The Pennsylvania State University

The Graduate School

Department of Electrical Engineering

DEVELOPMENT AND ANALYSIS OF THE HIGH ENERGY MONITORING

INSTRUMENT PATHFINDER FOR THE JANUS SATELLITE

A Thesis in

Electrical Engineering

by

Brian Christopher Schratz

Submitted in Partial Fulfillment
of the Requirements
for the Degree of

Master of Science

December 2008

The thesis of Brian C. Schratz was reviewed and approved* by the following:

Sven G. Bilén
Associate Professor of Engineering Design, Electrical Engineering, and
     Aerospace Engineering
Thesis Advisor

C. Russell Philbrick
Professor of Electrical Engineering

John D. Mitchell
Professor of Electrical Engineering

W. Kenneth Jenkins
Professor of Electrical Engineering
Head of the Department of Electrical Engineering

*Signatures are on file in the Graduate School

ABSTRACT

This thesis describes the early development of the High Energy Monitoring Instrument (HEMI) for the detection of gamma ray burst peak energies to be included on the proposed NASA/PSU Joint Astrophysics Nascent Universe Satellite (JANUS) being developed in response to NASA's Announcement of Opportunity: "Explorer Program: Small Explorers (SMEX) and Missions of Opportunity."

Included in the discussion is a comprehensive review of the first HEMI pathfinder, a cosmic ray detector, which was built over the course of nine months by students at The Pennsylvania State University's Student Space Programs Laboratory and launched successfully on a high altitude balloon on September 15, 2008. The purpose of this thesis specifically is to summarize the pathfinder development process, final design, operations, analysis of flight data, lessons learned, student effort, and feed forward to the JANUS HEMI project.

TABLE OF CONTENTS

LIST OF FIGURES

LIST OF TABLES

ACKNOWLEDGMENTS

Chapter 1

Background

1.1 HEMI Motivation

On 22 October 2007, NASA released an announcement of opportunity for a small explorer (SMEX) class satellite. In anticipation of this announcement, Penn State, in partnership with several other organizations, had already begun developing the concept for JANUS—the Joint Astrophysics Nascent Universe Satellite—to study high red shift gamma ray bursts in order to better understand the evolution of the early universe. In addition to JANUS two primary instruments, a third instrument to be developed by students was included as a student collaboration (SC) component [*CoBabe–Ammann and Klumpar,* 2008].

A student-built High Energy Monitoring Instrument (HEMI) will provide information on the peak energy of gamma ray bursts as well as a survey of the background energies in between bursts. The goal is to provide meaningful science that will enhance the JANUS science return. Additionally, the development of HEMI will expose undergraduate and graduate students to the processes and procedures of building spaceflight hardware and will better prepare this future generation of scientists and engineers for future careers in the aerospace industry.

Developing an instrument to NASA standards and requirements is not a trivial task for a predominantly undergraduate student group. Furthermore, the Student Space

Programs Laboratory's (SSPL) heritage has not included an experience with this type of

detector. As such, SSPL quickly decided on a technology development plan that would

mature the HEMI technology in accordance with the JANUS schedule. High altitude

balloons were chosen as the best platform. The cost and complexity of orbital launches

were prohibitive, and the duration of sounding rockets flights are too brief for this type of

science. High altitude balloons can provide sufficient duration for GRB science with less

complex design requirements and justifiable costs. Therefore, a preliminary pathfinder—

the primary discussion in this thesis—was conceived for a short-duration flight (~20

hours) on NASA's High Altitude Student Platform (HASP) operated by the Louisiana

State University. Based on lessons learned from HASP, another, more advanced

prototype is planned for flight on a long duration (>20 days) high altitude balloon

approximately two years after the HASP launch.

Because GRBs do not occur very frequently—on average there are one to two per

day—and the typical HASP balloon launch duration is roughly 20 hours; then it was not

very likely that a GRB would be detected by HEMI during the HASP flight. Taking this

into account, and keeping in mind that the ultimate goal is studying GRBs, this first flight

was intended to be a test of preliminary hardware as well as the student organization. On

this HASP flight, the instrument was used to detect cosmic rays as a precursor to studying

GRBs. HEMI collected information on the number of particles and their energies during

time intervals. The data processing algorithms for cosmic rays will differ from those for

GRBs. However, the detection and data collection hardware will be similar between the

two instruments.

The short duration pathfinder balloon experiment developed and analyzed by the students provided valuable experience to the students working on HEMI. Students were engaged throughout the mission life cycle from proposal to fabrication and were directly involved in the launch and data analysis.

Through this balloon project, students have been introduced to issues very similar to those they will encounter during the development of the satellite instrument. The current design for the HEMI detector uses a sodium iodide (NaI) scintillating crystal coupled with a commercial-off-the-shelf (COTS) photomultiplier tube (PMT). Students have become familiar with issues that arise in the use of PMTs, testing procedures, calibration, and data analysis from the PMT.

Students have provided a thermal analysis and suggested solutions for thermal issues. They have designed and built circuits for command and data handling, power, signal conditioning, and health and status monitoring. As part of command and data handling, the HEMI team now has experience in the area of pulse peak detection. This experience will provide a foundation as the students begin developing peak detection algorithms for a light curve of a GRB. The power and communication interfaces are also very similar to those of JANUS.

The HEMI team has also been introduced to the process of integrating an instrument into a host flight system, systems engineering, project management documentation, interfaces, and scheduling. In addition, this effort gave students significant experience in the end-to-end life cycle including data analysis and has better prepared them for the more complicated iterations to come.

1.2 Role of the Author

By the very nature of this project, the efforts described in this thesis comprised a collaborative work that involved a total of around a dozen undergraduate students. The role of this author, as a graduate student experienced in leading student space projects, was to lead the effort through the complete mission life cycle as well as take responsibility for the development of select components of the instrument while guiding students through the remainder of the instrument's design, testing, and integration for flight.

On the programmatic side, the author served as the project manager and lead systems engineer to oversee the development of the entire project. While project management and systems engineering tasks are preferably not performed by the same individual, a limited supply of skilled and experienced students made the adopted arrangement necessary.

On the technical side, the author was responsible for the C&DH system including both hardware and software. Two other undergraduate students assisted with this effort. At the beginning of the project, the author led the development of the scientific objectives and requirements—especially the background required to select an appropriate detector for the instrument. Through targeted recruiting, the science lead was eventually assumed by an undergraduate physics major. However, the author was still responsible for developing the support equipment and software for the detector testing and evaluation described in the Instrument Calibration section. Once the test setup was firmly established, the testing was continued by the science team.

Significant guidance was given by the author to the power team for the development of the DC/DC converters, based mostly on his past experience with the Penn State ESPRIT rocket payload [*Schratz,* 2006].

The thermal and mechanical teams were guided to a lesser extent as the author's expertise was not in these areas. Instead, the work presented here in the mechanical and thermal sections is a summary of the respective groups' efforts, which were guided by other more experienced members of SSPL.

As the project manager and systems engineer, the author was chiefly responsible for the integration (on and off site), testing, launch preparations, operations, and post-flight analysis.

Finally, as the purpose of this thesis is to prepare the student team as much as to develop the scientific and technical heritage, significant time was spent training, mentoring, and educating the young team from which the core of future efforts will be formed.

1.3 Relation to Past Missions

Since their discovery in the early 1970s, little information has been gathered about Gamma-Ray Bursts (GRBs). GRBs release a tremendous amount of energy, up to the order of GeV. Despite the allure of these phenomena, much of the physics behind them still remains unknown, including their origin. The three leading theories are 1) the collapse of two neutron stars upon one another forming a black hole; 2) a neutron star collapsing into a black hole; and 3) an extremely violent explosion of a supernova

forming a black hole. The first and second theories are for short bursts while the third theory is for long bursts, and proven by the *Swift* satellite. All three of these theories center on the turbulent activity of a black hole.

There have been numerous satellite investigations focused on understanding these phenomena. Previous investigations concerning GRBs, including the Compton Gamma-Ray Observatory, BeppoSAX, and *Swift*, have characterized low red shift GRBs and all of the components of their afterglows. However, these missions have not focused on the investigation of high red shift GRBs, which can help better understand the early evolution of the universe. BATSE on CGRO collected data from 2704 GRBs [*BATSE,* 2005] including measurements of the particle flux, fluence, and duration of each GRB. This served as a good basis for the further study of GRBs. BeppoSAX discovered that GRBs also emit radiation in the form of X-rays. *Swift t*ook lessons learned from both CGRO and BeppoSAX, and studied information on the X-ray, UV, and optical portions of GRB afterglows [*Gehrels,* 1998].

JANUS will be the first satellite to observe what happens during a high red shift burst and the respective afterglow. JANUS will measure the star formation rate, enumerate the brightest quasars and their contribution to re-ionization, and enable detailed studies of the history of re-ionization. JANUS also differs from previous satellites in the student collaboration involved. While student involvement has been present on past missions primarily in data analysis and science operations, none of these previous satellites have had students design, develop, and operate an instrument to contribute to the scientific objectives of the mission.

1.4 Overview of the Thesis

This thesis documents the full life cycle of the HEMI pathfinder mission. Chapter 2 discusses the implementation of each subsystem, with each section describing the driving requirements for the subsystem. Chapter 3 discusses the testing and calibration of the instrument components and the integrated instrument. The data discussed in Chapter 3 provides the foundation for the post-flight analysis presented in Chapter 4 which also includes post-flight testing and calibration. Chapter 5 presents the conclusions of this effort, lists key lessons learned during the course of the project, and outlines the continuing work that will feed forward to the development of the next iteration of the HEMI.

Chapter 2

Implementation

This chapter describes the technical implementation of the project that was created to meet the needs of the scientific and programmatic requirements of the HEMI pathfinder mission. It discusses the evolution of the design through the course of the life cycle, explains the detailed designs of key instrument components, and discusses trades and justifications for the instrument that eventually launched on HASP.

2.1 Evolution of Baseline Design

Significant design evolution occurred between the initial proposal design and the final flight instrument. The first major baseline design was created for the High Altitude Student Platform (HASP) balloon proposal submitted in December 2007 [*Schratz,* 2007]. At that time, the student team had only been formed about one month,, and there was only a cursory understanding of the science and engineering requirements. None of the students, mostly underclassmen, except the project manager had been through a complete mission lifecycle. For all but three, it was their first project. This baseline was designed mostly from discussions with faculty and graduate students from the Penn State physics department who had extensive experience in cosmic ray science and instrumentation. The baseline sensor, shown in Figure 2.1, was centered on using a single PMT, and made

first-order assumptions about the electronics and mechanical structure based on prior

Penn State student projects.
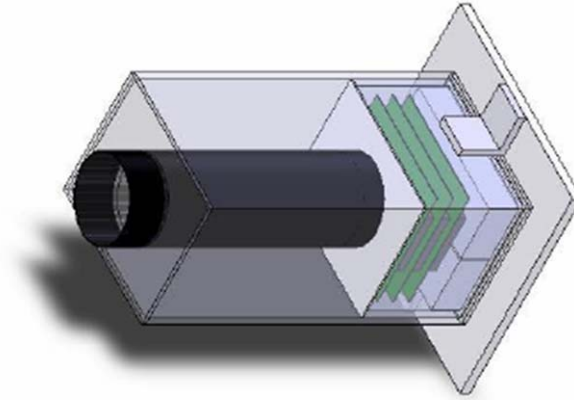
Figure 2.1: First HEMI Pathfinder Baseline Design

On 10 April 2007, approximately four months after the HASP proposal was

submitted, the pathfinder Critical Design Review (CDR) identified a new baseline design

shown in Figure 2.2 . The engineering implementation requirements were understood

better so more reliable numbers were used for power, volume, and mass. At this point,

several electrical component prototypes had been completed and tested; a thermal model

was built and tested; and the structure was ready for fabrication pending approval of the

subsystem leads. The science team added a second PMT to enable coincidence

detection—a method commonly used by past missions that would significantly improve

the science in the lower energy ranges.
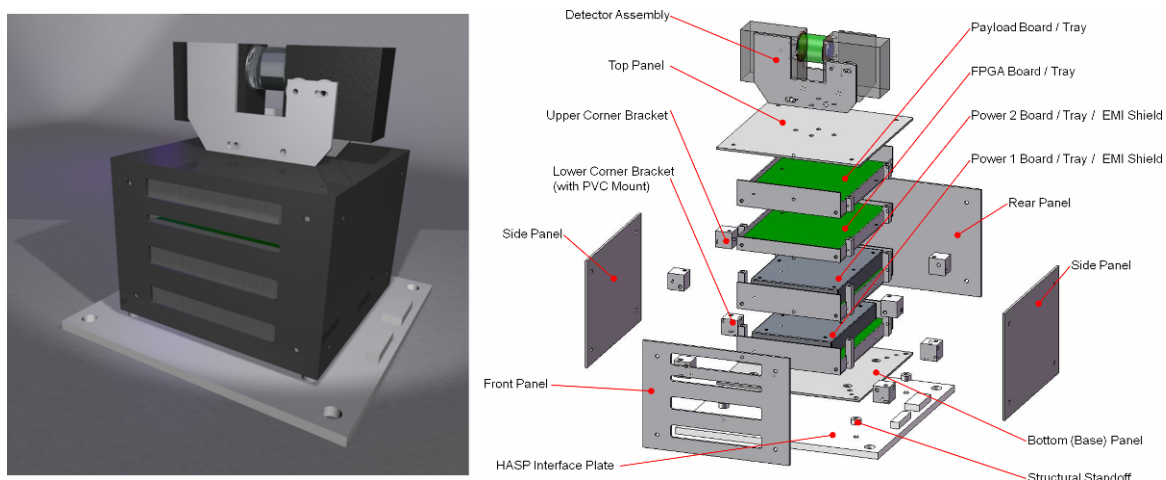
Figure 2.2: Second Major Baseline Design

On 27 May 2007, the PMTs were first tested in a vacuum chamber where they were observed to malfunction as the ambient atmospheric pressure dropped below ~12 torr. The nominal supply current increased from 14 mA to 47 mA, and the output signal went from sharp, clean pulses to indistinguishable noise. The initial hypothesis (and the original motivation for the vacuum test) was that the PMTs may not have been properly potted during assembly at the manufacturer. This would cause the PMTs to malfunction at the reduced pressures due to dielectric breakdown within the PMT module. HASP would carry the instrument to an altitude of approximately 36 km (120,000 feet) where the pressure was expected to be 1–10 torr (or 1–10 mm Hg). Consulting a graph of the Paschen curve, shown in Figure 2.3, showed that these pressures are near the minimum of the curve, where dielectric breakdown occurs at much lower voltages. Only the best practices in preparing the potting during the manufacturing process allows for protection against breakdown in reduced pressures. In the presence of the high voltage generated by the PMTs, the gas breaks down causing arcing. The PMT manufacturer, Hamamatsu,

later confirmed our explanation of our test results after several discussions with their product engineers who originally assured that these modules would operate in the low-pressure environment.
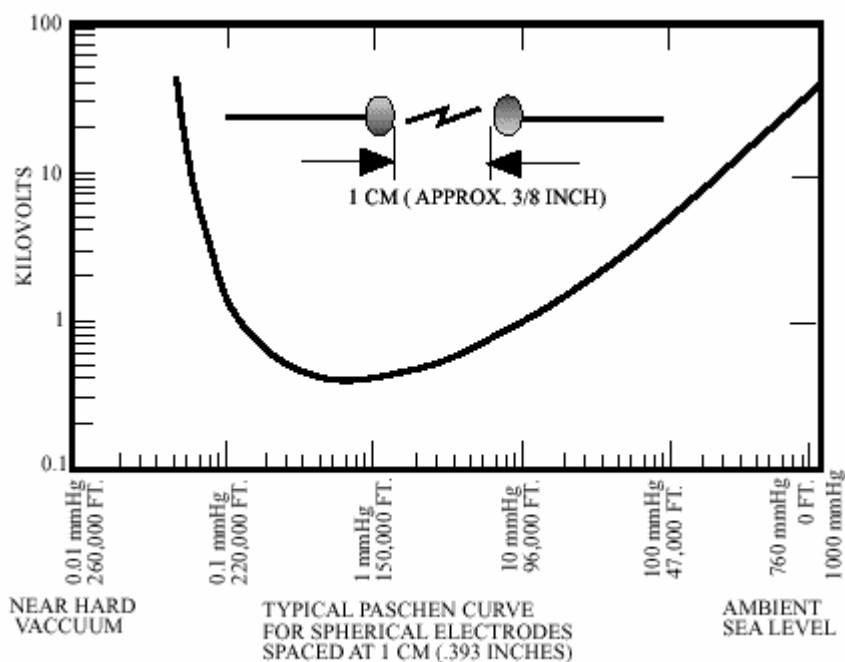
Figure 2.3: Paschen Curve for Dielectric Breakdown   [*Teledyne Reynolds,* 2008]

Two weeks were spent exploring alternative PMT assemblies, but given the short project schedule, limited order quantity, and limited budget, no feasible options from any manufacturer could be identified. With all other options exhausted, a pressure vessel was the only available solution. The pressure vessel requirement was imposed, which forced a total redesign, heavily impacted the project schedule, and implied drastic changes to the allocation of engineering requirements. The available volume decreased to maintain the mass budget.   The quantity and dimensions of printed circuit boards were reduced. The dual-PMT design was reduced back to a single PMT in order to meet volume requirements. The dual-PMT (coincidence measurements) de-scope in particular was a

very regrettable, but necessary. Fortunately, the minimum science requirements could still be met. Even with these reductions, the total mass budget increased to 4.3 kg, 1.3 kg over the 3-kg HASP allocation, and a waiver was granted after lengthy discussions with the HASP team.

Another two weeks after the pressure vessel decision was finalized, now at the end of June 2008, a third and final baseline design, shown in Figure 2.4, was agreed upon by the subsystem leaders. Fabrication of the primary structure began on 6 July 2008 and was completed two weeks later. Fabrication of the secondary structure components and electrical hardware followed shortly thereafter.
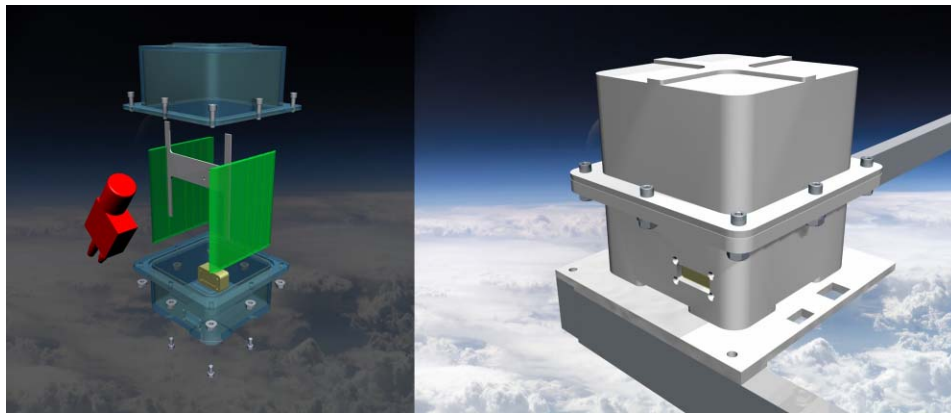
Figure 2.4: Third Major Baseline Design

The following sections describe the technical implementation of the HEMI pathfinder mission, and specific detail of the final design. However, as the designs were mature at the CDR prior to the pressure vessel implementation, these designs will be briefly discussed as well. The CDR baseline included additional features that were eventually de-scoped in the final baseline. These features, and the design effort behind them, may prove useful to future projects, specifically the planned long duration balloon

for the HEMI. Each subsystem section will discuss the CDR baseline followed by the changes made for the final baseline in addition to the final detailed design.

2.2 Science

2.2.1 HEMI's Contribution to JANUS Science

The primary purpose of the High Energy Monitoring Instrument on JANUS is to measure the output energy of high-energy gamma ray bursts (GRBs) and contribute to the context of JANUS' investigations of the evolution of the universe.

JANUS, which at the time of this writing is in the Phase-A proposal process, is a follow-on to the very successful *Swift* satellite, but is designed to capitalize and expand on *Swift*'s objective to use GRBs to study the early universe. Since its launch in November 2004, *Swift* has only detected one burst from the re-ionization era (GRB 050904 at a red shift, or z, of 6.29) [*Gao,* 2007]. Light is red shifted as it travels through the expanding universe. The amount of red shift is indicative of the distance (and time) the light has traveled. In this limited discussion of the thesis, z does not represent particle charge as it does throughout the rest of this thesis.

Over the course of its two-year baseline mission, JANUS should detect and observe on the order of 50 bursts from $z > 5$, including an estimated seven bursts from $z > 8$, out to a highest red shift of $z = 12$; and identify more than 400 quasars from $z > 6$, out to a maximum red shift of $z = 10$ [*Roming,* 2008].

JANUS will investigate the causes of re-ionization through star rate formation, quasar number density, change in luminosity over the re-ionization period (red shift of 5 $< z < 12$), and the contribution of stars and quasars to ionizing the interstellar medium. Identifying GRBs and quasars from the period of the early universe will give rise to a greater understanding of the re-ionization era [*Roming,* 2008]. By measuring the distribution of GRB red shifts, JANUS can form an accurate model of star formation over the range $5 < z < 12$, which contributed to the re-ionization of the interstellar medium.

JANUS will use the X-Ray Flash Monitor (XRFM) to detect GRBs and locate the burst position to sub-arcminute resolution—a vast improvement over BeppoSAX, which had an accuracy of three arcminutes (*Feroci,* 1997). Within minutes, JANUS will focus its Near-Infrared Telescope (NIRT) on the burst afterglow to measure the brightness and red shift (for $z > 5$) to 7.5% accuracy. The combination of the XRFM, the NIRT, and quick response make JANUS the most capable instrument for the study of the early Universe.

The prompt emission of GRBs is a broad-band phenomenon that has been detected by various instruments and for various bursts with energies from below keV to greater than GeV, i.e., regimes spanning eight, or more, orders of magnitude in photon energy. The full nature of the physical processes powering the burst prompt emission remains elusive, but their spectra are commonly parameterized as a Band function [*Band,* 1993], with two distinct power-law segments joining at E_{peak}, the peak energy, in a νF_ν energy distribution—that is, the photon energy that characterizes the bulk of the burst's energy output. Within the BATSE burst catalog, peak energies range from 40 keV,

roughly the low energy cutoff for BATSE, up to 1 MeV, with a typical value of $E_{\text{peak}} \approx$ 300 keV.

The XRFM instrument has been designed to *detect and localize* as many high red shift bursts as possible, thus achieving the primary science goals of the JANUS mission; it will also characterize the prompt emission spectra of these and other lower red shift bursts across its 1–20 keV band pass. The primary science return from XRFM and NIRT can be accentuated by broader spectral coverage, and several distinct science drivers can be identified.

First, including HEMI will allow for the measurement of E_{peak}, which can lie outside the XRFM band pass, even for high red shift GRBs. This measurement of E_{peak}, provided by HEMI, enables the calculation of the total energy output of the burst, E_{iso}. Measuring the energy output of the brightest and highest red shift bursts, while not necessary to exploit burst afterglows for cosmology, is of great interest from the standpoint of physical models, which must contrive to release these extreme energies in a short amount of time. Indeed, the high red shift GRB 050904, with $z = 6.3$ and $E_{\text{peak}} >$ 150 keV [*Cusumano,* 2007], was found to have an extraordinary energy output, more than ten times the typical value for $z \approx 1$ bursts [*Frail,* 2006; *Gou,* 2007].

Second, measurement of the burst E_{peak} and E_{iso} will enable tests of several proposed luminosity indicators for GRBs [*Liang & Zhang,* 2006]. While it is not clear that cosmological constraints can be derived from these relations in a non-circular fashion [*Bulter,* 2007], this application will hold for bursts at any red shift, so long as the red shift is measured via either JANUS or ground-based observations.

Finally, the presence of a detector of $E > 20$ keV photons onboard JANUS will enable XRFM detection and localization of additional, spectrally hard bursts that would otherwise lie below the XRFM threshold. Based on detection of a burst of high-energy photons, the XRFM software can relax its threshold for identification of new sources. While this approach is not expected to lead to the discovery of any additional high red shift bursts (these are relatively soft and slow evolving), it may enable real-time localization of additional short, hard bursts, an intriguing subset of the GRB population that may result from compact object merger events [*Fox*, 2005].

2.2.2 Pathfinder Objectives

SSPL has developed a HEMI pathfinder experiment that flew on a short-duration, high-altitude balloon on 15 September 2008 from Ft. Sumner, NM. As GRB events are typically observed only once or twice per day, this balloon's 20-hour flight duration would not guarantee the observation of a GRB. Therefore, the scientific investigation focused on more common, low-charge cosmic rays. The development of this pathfinder cosmic ray detector balloon instrument gave students valuable experience that will be critical as they develop the GRB detection instrument for JANUS.

The pathfinder instrument's scientific objective was to distinguish cosmic ray particles by their charge ($z = 1, 2, 3$) and possibly an occasional cosmic shower. During a cosmic shower, the energies would be comparable to the normal background but the detection rates would be higher. Note that from this point forward, z represents the particle charge.

2.3 Detector

The baseline design for HEMI on JANUS is a traditional photomultiplier tube (PMT) with a scintillating crystal, likely NaI or CsI. To maintain as much heritage as possible between the HEMI pathfinder and the eventual HEMI for JANUS, the pathfinder used similar technology. Because of the different science objectives (cosmic rays for the pathfinder compared to GRBs for JANUS), short development time, less stringent requirements, and limited budget, the pathfinder detector was not exactly the same as the final one to be used on JANUS. The performance of the pathfinder PMT has a slower response (a few microseconds compared to a few nanoseconds), but the general characteristics of the PMT output pulse will be analogous to the eventual JANUS PMT.

A typical scintillator and PMT configuration is illustrated in Figure 2.5 below. Energetic particles strike the scintillating material and cause light, around 420 nm for NaI, to be emitted. NaI is hydroscopic, and therefore, requires careful handling in a controlled environment. One option is to acquire an encased assembly where the crystal comes, for example, encased inside a thin metal reflective shell. If coincidence detection is desired, it must be confirmed that sufficient area is left exposed for the PMT apertures.
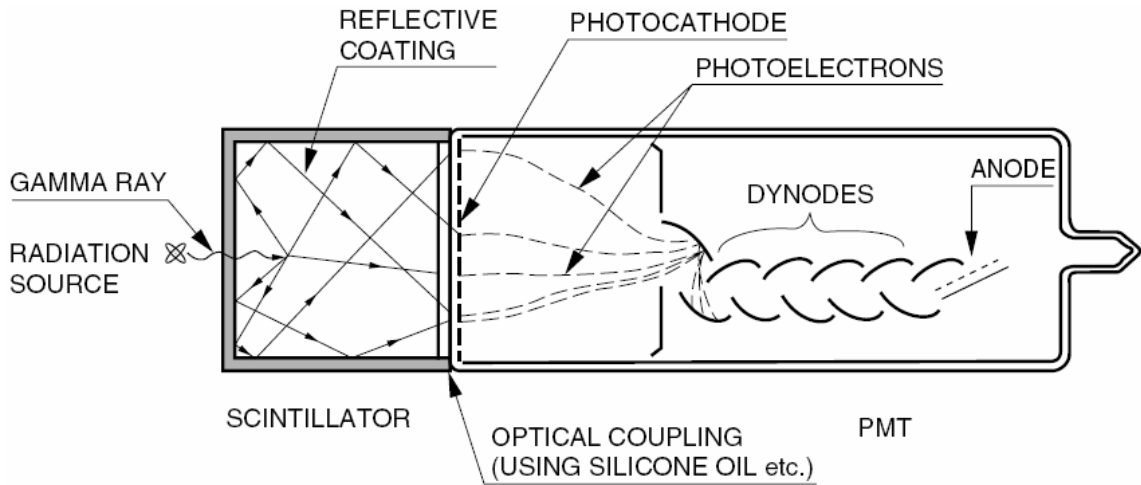
Figure 2.5: Typical Scintillator and PMT Configuration
(image credit, Hamamatsu Corporation)

Energy deposited in the crystal by energetic photons or particles will produce photons that will strike the photocathode of the PMT to produce electrons. The small number of electrons will be amplified by the PMT several orders of magnitude.

A scintillating crystal material has a specific stopping potential, *S*, defined by

$$S = -\frac{dE}{dx},$$

2.1

which governs the energy per distance deposited into the crystal material. Therefore, the size of the crystal, which determines the path length of the particle through the crystal, directly affects the amount of photons emitted by the crystal. Also, the energy loss of the particle is described by the Bethe formula, which states that the energy loss of the particle (energy deposited into the crystal) is proportional to the square of charge number, z, of the particle according to

$$-\frac{dE}{dx} = \frac{4\pi e^2 z^2}{m_0 v^2} NB,$$

2.2

where e is the electron charge, m_0 is the electron mass, v is the velocity of the particle, and N is the number density of the scintillator atoms. B is defined as

$$B \equiv Z\left[\ln\frac{2m_0 v^2}{I} - \ln\left(1 - \frac{v^2}{c^2}\right) - \frac{v^2}{c^2}\right]$$

2.3

where Z is the atomic number of the crystal atoms and I represents the average excitation and ionization potential of the absorber and is normally treated as an experimentally determined parameter for each element. Therefore, the light output of the crystal is dependent on the path length of the particle through the crystal, which will vary by incident angle and location, and z^2 for that particle [*Knoll,* 2000].

The process of energy deposition and photon emission varies with the energy of the incident particle or photon. The final JANUS HEMI will investigat gamma ray photons compared to this HEMI pathfinder, which measured high-energy charged particles. For the lower-energy photons (<100 keV) in a NaI detector, the predominant mechanism is the photoelectric effect. Between 100 keV and 2 MeV, Compton effects dominate. Above 2 MeV, pair-production provides a significant contribution [*Saint Gobain,* 2008]. Since the HEMI pathfinder is investigated cosmic rays that are in the GeV range, the emitted photons are caused mostly by many interactions with atomic electrons of the scintillator material—either through Coulomb forces as the charged particle passes near atomic electrons, or excitation or ionization of atomic elections. For the HEMI sensor on JANUS, the interesting signals will be from On the eventual HEMI for JANUS, the topic of interest will be the scintillator photons due to both the photoelectric effect and the Compton effect.

While many PMT designs exist, each with their strengths and weaknesses, the basic operation is the same for most models. Photons emitted from the scintillating crystal strike a photocathode at the front of the PMT (shown earlier in Figure 2.5) emitting photoelectrons. These electrons are then accelerated towards the first dynode, which is coated with secondary emissive material. The electron strikes the dynode material and ejects other electrons from the metal by transferring some of the dynode kinetic energy to the electrons. This process continues from dynode to dynode, until the electrons are collected at the anode as current pulse. Various options for amplification, pulse shaping, and current-to-voltage conversion are used after the anode. PMT gains can range from 10^2 to 10^8. This gain is dependent on the specific tube and the user-selectable control voltage applied to it, typically in the range of 0.5–1.5V. The control voltage is a low-voltage signal used to scale the high voltage potentials applied across the PMT dynodes (~100's of volts per dynode). The electron multiplier process requires the anode to be at a much higher voltage potential than the cathode, typically hundreds of volts. This high voltage is divided across each dynode between the anode and cathode. Figure 2.6 shows the relationship between gain and control voltage for the detector used on the pathfinder HEMI mission. The different lines are for the two versions of the H7827 PMT module which differ by the response time and dynamic range.
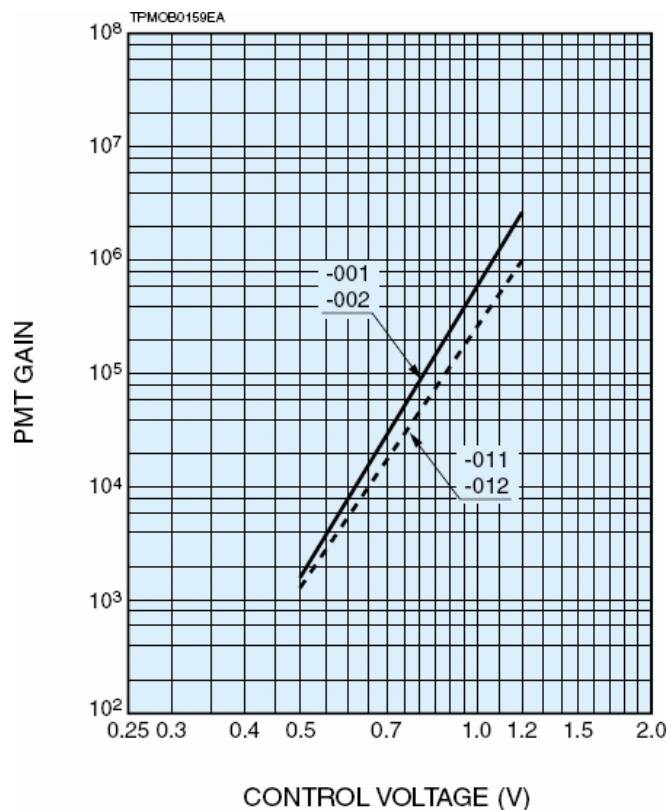
Figure 2.6: PMT Gain–Control Voltage Relationship | [*Hamamatsu*, 2008]

The high voltages used for PMTs presents a design challenge for high-altitude balloon missions which operate in a low atmosphere (~few torr).   In high-altitude balloon applications, dielectric breakdown in the rarefied atmosphere as described by the Paschen curve can cause arcing inside the PMT. This effect and mitigations for it are discussed throughout this thesis.

2.3.1 Selection and Figures of Merit

There is a wide variety of PMTs available suited for an almost equal variety of applications. Many figures of merit exist for selecting an appropriate scintillator and

PMT. The appropriate detector must be well matched to the energies, environment, and application of the experiment while conforming to technical and programmatic constraints of the project.

Since the scintillating crystal was chosen to be NaI due to its availability, cost, and sufficient efficiency for this project, the PMT first of all had to be well matched to the crystal. That is, have peak sensitivity at the same wavelength emission as the NaI crystal—between 310 nm (fast) and 410 nm (slow). Next, the PMT had to be compact and, given the short development schedule, be as simple as possible to integrate into the instrument. For this reason, complete factory-provided PMT modules were also considered alongside acquiring just PMT and then purchasing and/or developing the support circuitry (specifically the high-voltage DC/DC converter, voltage divider, and electrometer).

Other technical considerations were the amount of dark current (noise of the system) and its sensitivity. Practical considerations were of course mass, volume, aperture size (to match the crystal), and input power.

2.3.2 Selected Detector

As was mentioned previously, the detector system intended for the pathfinder mission did not have to match the exact one that will later be built for JANUS. In fact, because of programmatic (cost and schedule) limitations of the HASP project, selecting the same system for both was impossible. Instead, the team selected a detector system that best met the requirements of form and function, while still satisfying the constraints

of cost and schedule. While it would be slower than the eventual JANUS HEMI detector

and not ruggedized for spaceflight, it allowed the pathfinder HEMI to meet the necessary

requirements of its mission.

The pathfinder instrument used a cylindrical 1″ × 1″ diameter NaI(Tl) scintillating

crystal, shown in Figure 2.7, purchased from Saint Gobain as the scintillating crystal.

The crystal was encased in a reflective material on all but one face. The original plan

was to have two PMTs each observe opposite faces of the crystal in a coincidence

implementation. The metal enclosure required that, for coincidence measurements, the

two PMTs would have to both observe the same crystal face so the PMTs each only

partially overlap the crystal, sharing the light output rather than being securely attached to

separate faces. Eventually engineering constraints described in Section 2.1 limited the

design to only a single PMT.

Figure 2.7: Packaged Sodium Iodide Crystal Used on HASP

The crystal was coupled to an H7827-001 PMT module from Hamamatsu, shown

in Figure 2.8, which includes a PMT along with the high-voltage DC/DC converter,

voltage divider, and low-noise amplifier that converts the anode current to a voltage

scaled between 0–10 V. The penalty for the convenience of using this module is that the

bandwidth and response time was very slow. The data sheet quotes a 20 kHz bandwidth,

while the project's own testing measured the fall time as low tens of microseconds,

depending on the energy of the pulse. The PMT for JANUS will have to be much

faster—in the range of a few nanoseconds for rise and fall time. The speed is less critical

for cosmic rays, as their rate of occurrence is much less than that during a GRB.

However, the slow response would impose implementation requirements on the

supporting electronics, discussed in the C&DH and Instrument Testing sections below.

Figure 2.8: Hamamatsu H7827-001 PMT

A common approach for mounting the scintillating crystal to the PMT is to use

optical cement. However, optical cement is difficult to remove once hardened, which

means that switching between the flight unit and flight spare unit would be impossible in

the field. Rather than using optical cement, the team used room-temperature vulcanizing

rubber (RTV). RTV provides a reliable connection, while remaining easy to remove if

required. The light output from the crystal was more than sufficient, so any loss of

efficiency by not using the optical cement was tolerable.

2.3.3 Detector Characterization and Initial Testing

Once the detector system was selected, a set of tests was conducted to completely

understand its response in all expected operating environments. Understanding the

detector was critical in developing electronics capable of successfully interpreting the data from it.

Perhaps the largest initial design driver was the output response of the detector due to either dark current or particle detection. The electronics designers were specifically interested in the shape and timing of the output pulse, because these characteristics would drive the performance requirements for hardware and software.

The left image in Figure 2.9 shows a typical output pulse in response to dark noise. In this test, the control voltage was set to 0.7 V and no scintillation crystal was present. The PMT was completely enclosed in a light-tight container so the only signals would be from dark noise. Notice that there are many very low amplitude noise pulses around the baseline. Occasionally, larger dark noise pulses that appear similar to a meaningful energetic event, like the 0.4-V pulse depicted in Figure 2.9, are produced which appear similar to a meaningful energetic event, although typically at lower voltages.
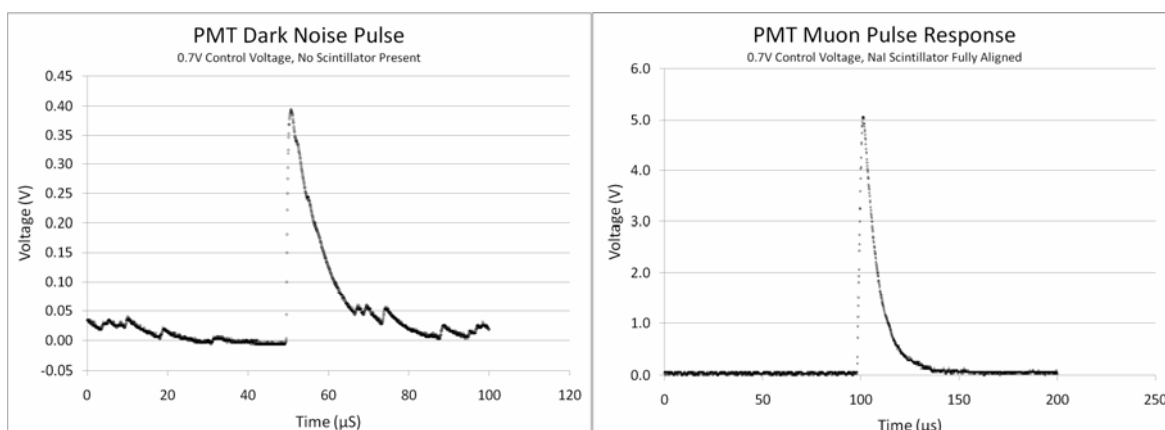
Figure 2.9: PMT Dark Noise and Muon Signal Response (note scale change)

Note the relatively slow decay time of the pulse. Common "fast" PMTs have a response of a few nanoseconds, compared to this module's tens of microseconds. As there is no scintillation crystal present, this delay is certainly due to the PMT module and is likely due to the small bandwidth (20 kHz) of the built-in electrometer.

Understanding the amplitude, rise time, and fall time characteristics of the scintillator–PMT system was necessary to reliably design the peak detection electronics. Understanding the relationship between true signals and dark noise was required to determine the appropriate designs for pulse discrimination and amplification.

2.4 Mission Design and Operational Environment

The High Altitude Student Platform (HASP) served as the host vehicle for the HEMI instrument pathfinder. This section describes the expected operational environment to which the HEMI pathfinder was designed, and the actual environment experienced during the flight.

Operated by the Louisiana State University for NASA, HASP provided the balloon, recovery system, integration, launch, and operations support. HASP provided all structure up to an interface plate for each payload. Figure 2.10 shows the HASP payload in the setup, hang-test, and flight configuration. The circles in the left and right images highlight the HEMI pathfinder. Additional available support systems included power, communication for data downlink and command uplink, telemetry of analog channels, and access to controllable relays.
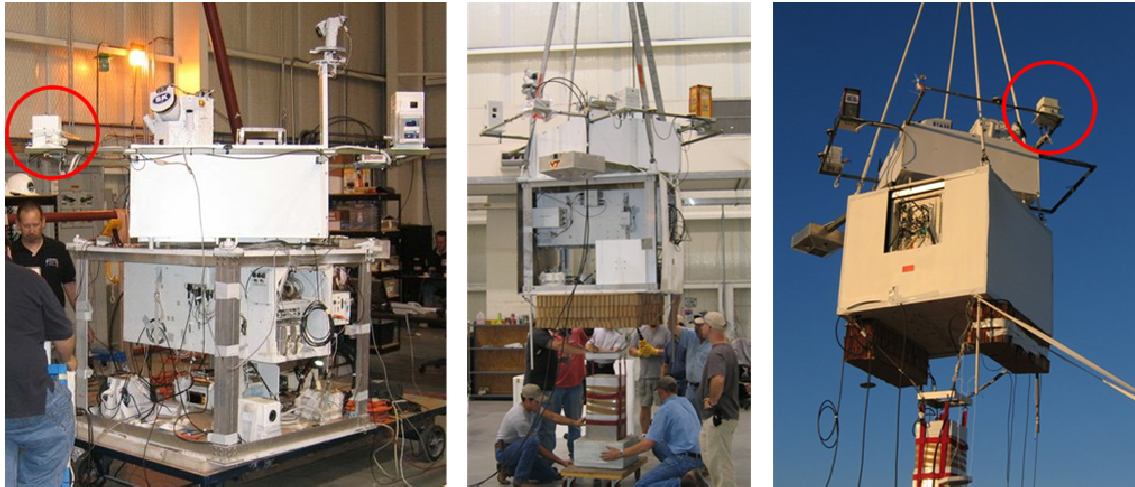
Figure 2.10: HASP Payload in Various Configurations (HEMI Pathfinder Circled)

HASP provided for two classes of payloads, large and small, which differ primarily in resource allocations. Smaller payloads were placed out on booms beyond the primary structure and, therefore, are better exposed to Earth's albedo, space, and solar environment. Large payloads mounted on top of the HASP primary structure, and are thus shielded from ground radiation. Figure 2.11 illustrates the HASP system with HEMI preparing for launch (left) and shortly after launch ascending through approximately 8,000 feet (right).

Figure 2.11: (L) HASP with HEMI Preparing for Launch and (R) During Ascent

The HASP Call for Proposals provided a measured thermal profile, shown in Figure 2.12, as a basic guideline for thermal design. The Ambient Outside Temperature curve is indicative of a small payload mounted out and away from the HASP structure, while the Platform Top Temperature curve is indicative of a larger payload mounted on top of the HASP structure [*HASP-CFP,* 2008].
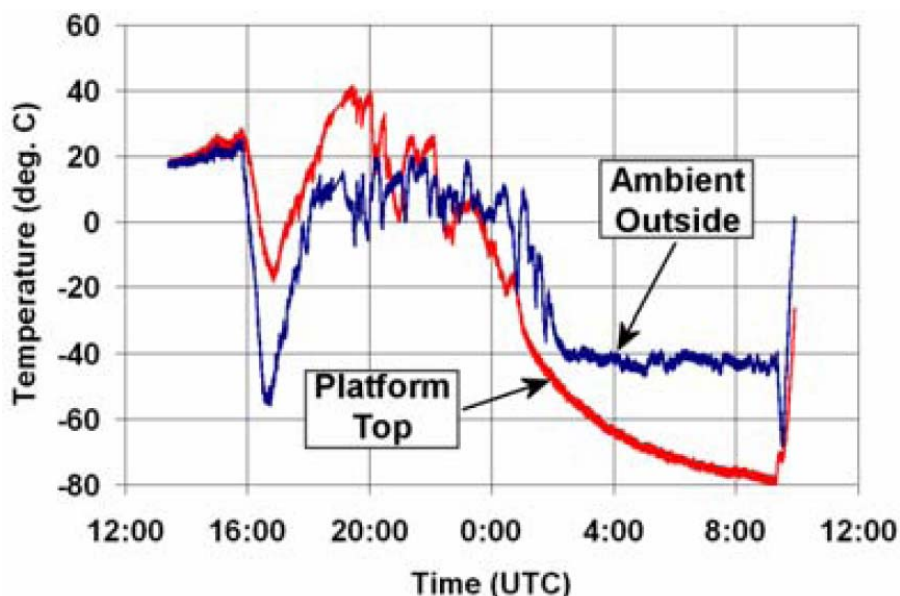
Figure 2.12: HASP Expected Temperature Profile

HASP power was supplied by batteries providing a nominal 30-V us; although depending on the battery state of charge, the voltage was expected to vary between 29 V to 33 V. HASP operators retained control of the power relays for each instrument and therefore were able to selectively turn on and off the instruments. Furthermore, each small instrument (HEMI's category) was rated for 500-mA current draw, with a fuse that will open if current exceeded 1.5 A for more than one second [*HASP-SPIM,* 2008]. Actual flight data, shown in Figure 2.13, indicates that the voltage supplied to HEMI was close to the nominal 30 V for the entire flight, with only small periodic variations— possibly due to diurnal temperature variations. Note that power to the HEMI was turned off around 24 hours into the flight in preparation for an anticipated flight termination. The power was later restored until the second and actual flight termination sequence.
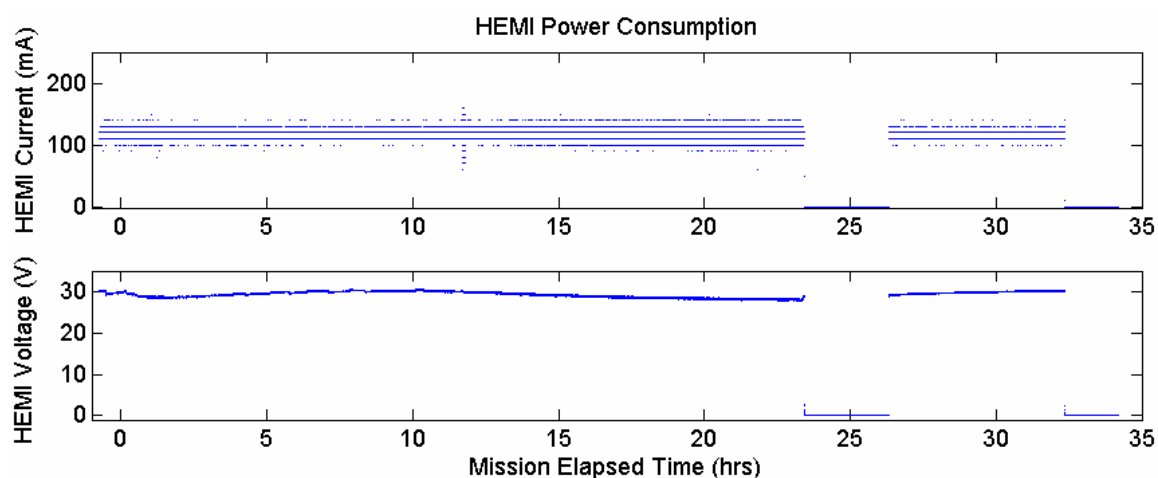
Figure 2.13: HEMI Flight Power Profile

Bidirectional digital communication was available over the standard RS-232 interface configured for eight data bits, one stop bit, and no parity. HASP could select baud rates to meet instrument requirements. For HEMI, it was mutually decided by the HASP and HEMI teams to use 2400 baud.

2.5 Systems Engineering

Given the limited scope and labor resources of the HEMI pathfinder, the central systems engineering effort was divided among the subsystem lead engineers and managed by the project manager. HASP drove the system-level allocation constraints, while self-derived system requirements based on HEMI's scientific and engineering objectives drove the subsystem functional requirements, performance requirements, allocations, and interfaces. Management of requirements and interfaces was accomplished through regular team meetings and frequent intermediate communication.

Table 2.1 summarizes the resource budgets originally allocated to the HEMI payload by HASP. The original proposal did not exceed the available HASP allowances. Additional downlink capacity was requested to enhance science, but was not required. With the notification of acceptance, HASP raised the HEMI downlink data rate to 4800 bps. Later, the HEMI and HASP teams would mutually agree upon 2400 bps for flight.

Table 2.1: Initial HEMI Resource Allocations on HASP

Maximum mass	3 kg
Maximum footprint *(including mounting structure)*	15 cm × 15 cm
Maximum height *(may need to be negotiated with neighbor payloads)*	30 cm
Supplied voltage	29–33 V_{DC}
Available current	0.5 A @ 40 V_{DC}
Maximum serial downlink (bit stream)	1200 bps
Serial uplink	2 bytes per command
Serial interface	1200 baud, RS-232 protocol, DB9 connector
Analog downlink	Two channels in range 0 to 5 V_{DC}
Discrete commands	Power On, Power Off
Analog and discrete interface	EDAC 516-020

The change to a pressure vessel drastically limited the design in mass and exceeded the mass allocation. To compensate, the payload volume was reduced to the minimum possible size in order to lower the mass of the pressure vessel. Even with reductions, the mass allocation was still exceeded and a waiver obtained. Although the mass allocation increase was approved, the increase was not enough to produce a large enough structure for two PMTs.

Power was never a driving constraint, and power requirements actually decreased with time as the circuitry complexity was reduced and the power-intensive heaters were removed. Therefore, the primary responsibilities of the systems engineering effort were

to ensure that interfaces between various instrument components were met and that all

HASP technical and programmatic requirements were satisfied.

2.6 Command and Data Handling—Instrument Electronics

The command and data handling (C&DH) subsystem was responsible for the

uplink and downlink communication with HASP, monitoring and controlling the internal

environment, and interfacing with the PMT/crystal detector, both providing the control

signal and interpreting the output signal.

2.6.1 CDR Baseline Design

The electrical block-level diagram for all of HEMI is presented in Figure 2.14 and

shows the electrical connections for power and data, as well as the physical printed

circuit boards (PCBs) and other external components.
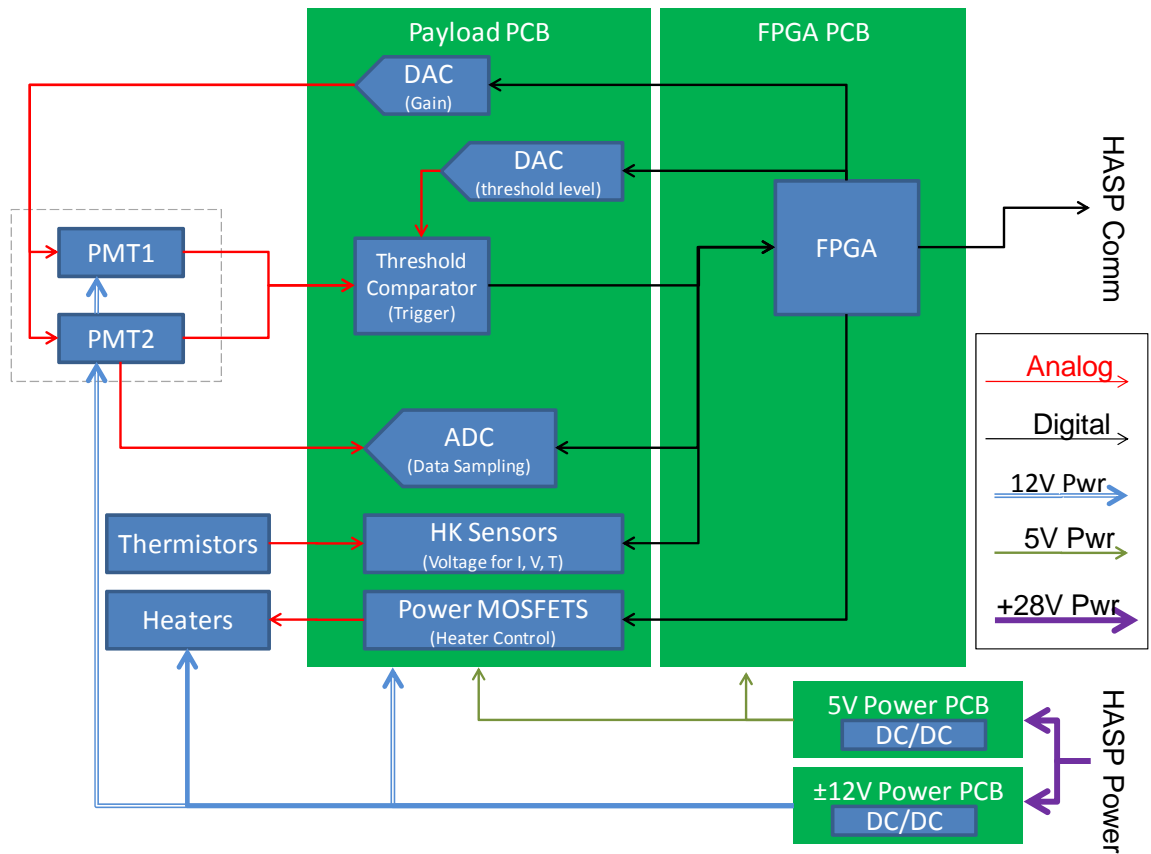
Figure 2.14: HEMI Electrical Block Diagram at CDR

The C&DH team was responsible for the Payload PCB and Field Programmable Gate Array (FPGA) PCB illustrated in Figure 2.14 as well as the electrical interfaces to the other components (power PCBs were the responsibility of the power subsystem). The capabilities of this design met the requirements current at that time. The specific capabilities and requirements, grouped by relevant subsystem, were:

- Payload:
  - Remotely adjustable gain control for PMTs
    - Voltage range: 0 V to 1.1 V
    - Compatible with PMT input impedance: 100 kΩ
  - Signal trigger with remotely adjustable threshold
    - Two voltage inputs (0–10 V)
    - Threshold adjustable from 0–10 V

- o Sample <u>single</u> PMT signal
  - ▪ 0–10 V input
  - ▪ 20 kHz signal (use >40 kHz sampling)
- o Data storage
  - ▪ Record energy spectrum: 128 bins, 256 max counts each
  - ▪ 8-bit resolution
- o Provide safe mode
  - ▪ Include ability to shut down PMTs if operating temperature ranges are exceeded. Continue to record, report, and regulate temperature.
- Thermal
  - o Provide thermal monitoring capabilities
    - ▪ At least 10 temperature channels
    - ▪ 5 V input range
    - ▪ >8-bit resolution
    - ▪ > 0.02 Hz sampling per channel
  - o Provide thermal control capabilities
    - ▪ Provide for at least 7 patch heaters
- Mechanical
  - o Conform to board interface agreements
    - ▪ Board size: 5.312 × 3.898 inches
    - ▪ No thru-hole parts 0.250 inches from the long edges
    - ▪ Connectors on only one short side of the board.
- Power
  - o Monitor voltage, current
    - ▪ 12-V board: input current, input/output voltage
    - ▪ 5-V board: input current, input/output voltage

The heart of the C&DH system was the FPGA. At the time, the intention for the

JANUS HEMI was to fly a Radiation Tolerant Axcelerator (RTAX) FPGA manufactured

by the Actel Corporation. To maintain some feed forward to that design, the pathfinder

used an Actel FPGA as well. Since RTAX chips are anti-fuse, making them one-time

programmable and very expensive, the team selected the Actel 208-pin ProASIC3

250,000-gate FPGA in a plastic quad flat pack package. Using flash technology, this

FPGA is reprogrammable and commercially available at relatively low cost. This FPGA

was chosen specifically to provide feed-forward to the JANUS project. While even the

family of FPGA will likely be different for the JANUS HEMI, the Actel development

environment will be used for both projects. Preliminary estimates showed that the selected FPGA has excess capability for this pathfinder mission. Since the over-capable chip would consume negligible extra power and cost, this chip was selected simply because SSPL already possessed development kits for the chip, with full schematics and reproducible PCB designs.

This design originally intended to create a custom development board featuring only the FPGA; voltage regulators for the FPGA 3.3 V and 1.5 V supplies; RS-232 transceiver chip and standard RS-232 nine-pin connector; and 100-mil stacking rectangular headers to provide access to each port of the FPGA. The intent was to create a development board, shown in Figure 2.15, that could be flown on HASP and then would be compatible with future custom boards that could allow students to rapidly prototype the designs. The payload board would include the same stacking headers to pass digital signals to and from the planned payload PCB and the FPGA PCB. The schematics for these designs are included in Appendix H.
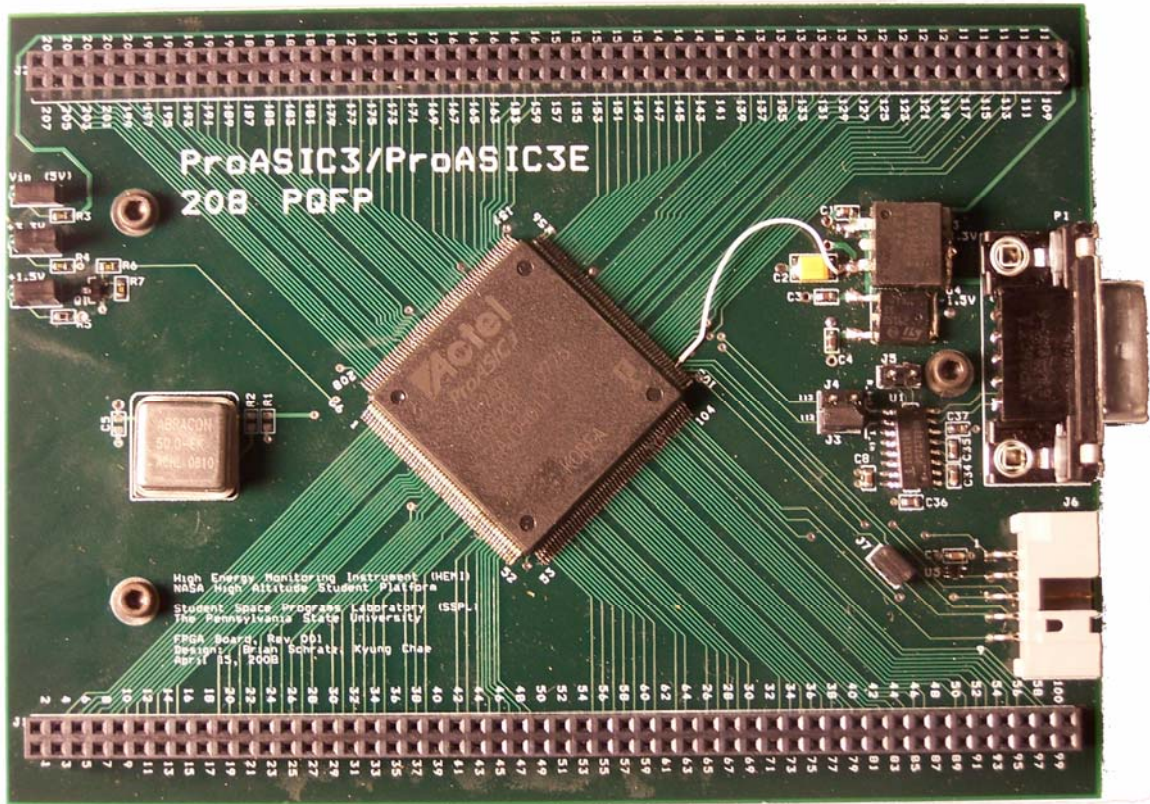
Figure 2.15: HEMI Custom FPGA Development Board

For this mission, a second development board, shown in Figure 2.16, was created with many mechanical pushbuttons, LEDs, DIP switches, and both pin and receptacle breakout headers for each port to provide for easy prototyping. Schematics for this design are in Appendix H. Again, this was intended to be used as a tool for students on future projects. This was intended for development only, and never intended to fly.
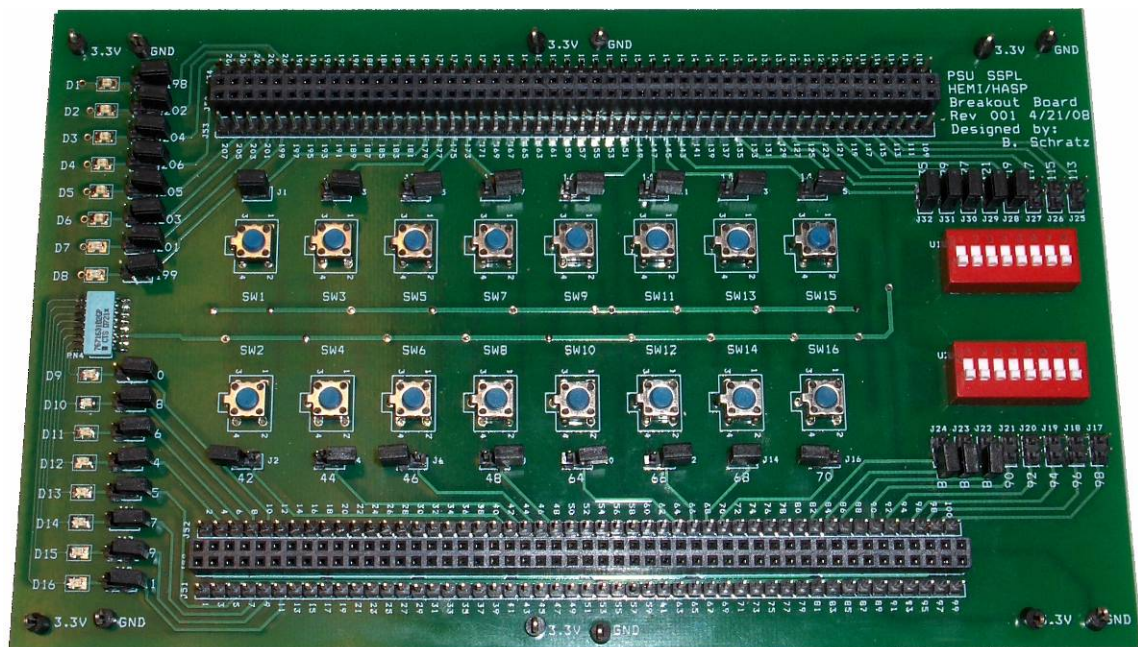
Figure 2.16: HEMI Custom Development Board

The Payload Board (intended for flight) provided the analog interface to the rest of the system. The first function was to set the PMT gain control voltage and to condition and digitize the PMT output. The second function was to monitor and regulate, when possible, the environment throughout the instrument.

The science team required the ability to use coincidence measurements, discussed in Chapter 3, to reduce false-positive detections. The concept was that the sources of noise are random so it is probable that, if one PMT produces a false output, it is statistically unlikely that the second PMT will also produce a false signal at the same time. This was verified by the science team through testing the PMTs, and is discussed in Section 3.4.

This design implemented the coincidence feature using a simple logic AND gate configuration shown in Figure 2.16. Specifically the CD4081BNSR part from Texas

Instruments was used, which allowed for 12-V logic (compatible with the 0–10 V signals from the PMTs) in a small surface mount package. The output was then passed through a simple voltage divider to bring the signal down to the 3.3-V logic that would serve as the pulse trigger for the FPGA.

Also shown in Figure 2.17 are the comparators used to condition the input triggers first from the PMTs before reaching the AND gate to ensure that appropriate logic levels were met. If the output voltage from the PMT exceeded the comparator reference voltage, it would produce a 10-V output trigger to the AND gate, otherwise the output was zero. Positive feedback was included to introduce hysteresis to limit jitter. Furthermore, the science team wanted the comparator threshold to be adjustable to any voltage between 0–10 V during flight so that adjustments could be made in response to the real-time data. Specifically, if too many peaks were detected (likely in the lower energies), the comparator reference could be increased to focus only on the higher energy events. If no or few peaks were detected, the threshold could be lowered to extend the energy range into the lower, more common energies. Alternate practices are to use pulse-height windowing.
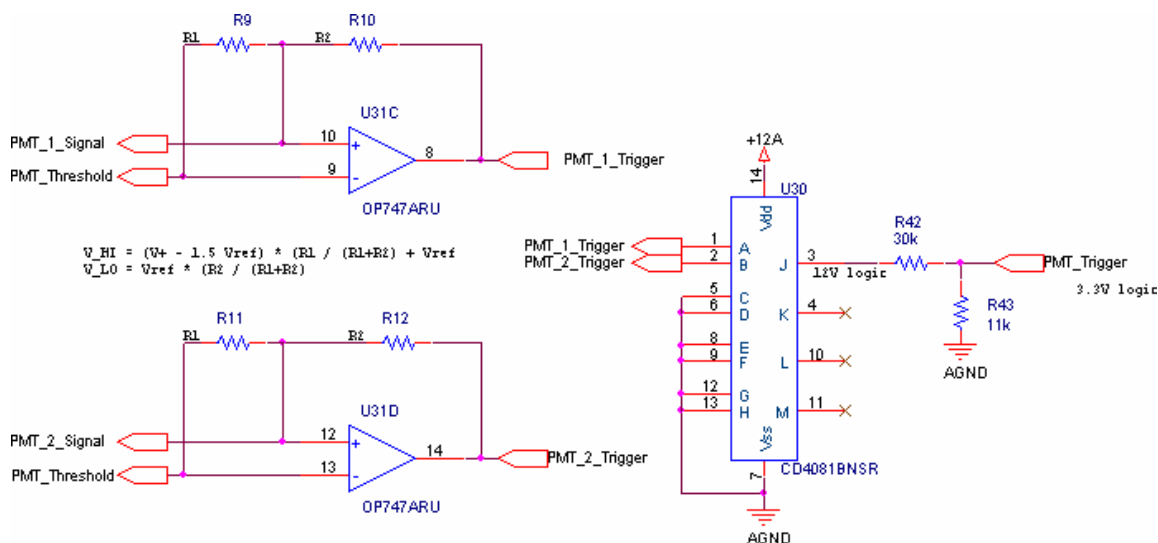
Figure 2.17: Circuit Implementation for Coincidence Measurements

The threshold was controlled using a digital-to-analog converter (DAC), which was controlled by the FPGA in response to uplink commands during flight. An up-linked command could be sent to the FPGA that then would command the DAC to provide a specific analog voltage. The chosen DAC was the AD7801 from Analog Devices. It was chosen for its simple parallel interface, optional external voltage reference for increased stability, flexibility for 2.7–5.5-V supply, rail-to-rail output, low power, and compact packaging. The 8-bit interface was deemed sufficient resolution for this application.

Figure 2.18 shows the schematics that the DAC used to set the comparator thresholds along with a second DAC used for the PMT control voltage (described below). The digital input lines were shared between both DACs. As the DACs only respond to commands when the DAC chip select (CS) pin is set low, an inverter gate on the control voltage DAC allowed the FPGA to exclusively program the appropriate DAC device. The unselected DAC would ignore programming commands until the CS line was inverted again by the FPGA.
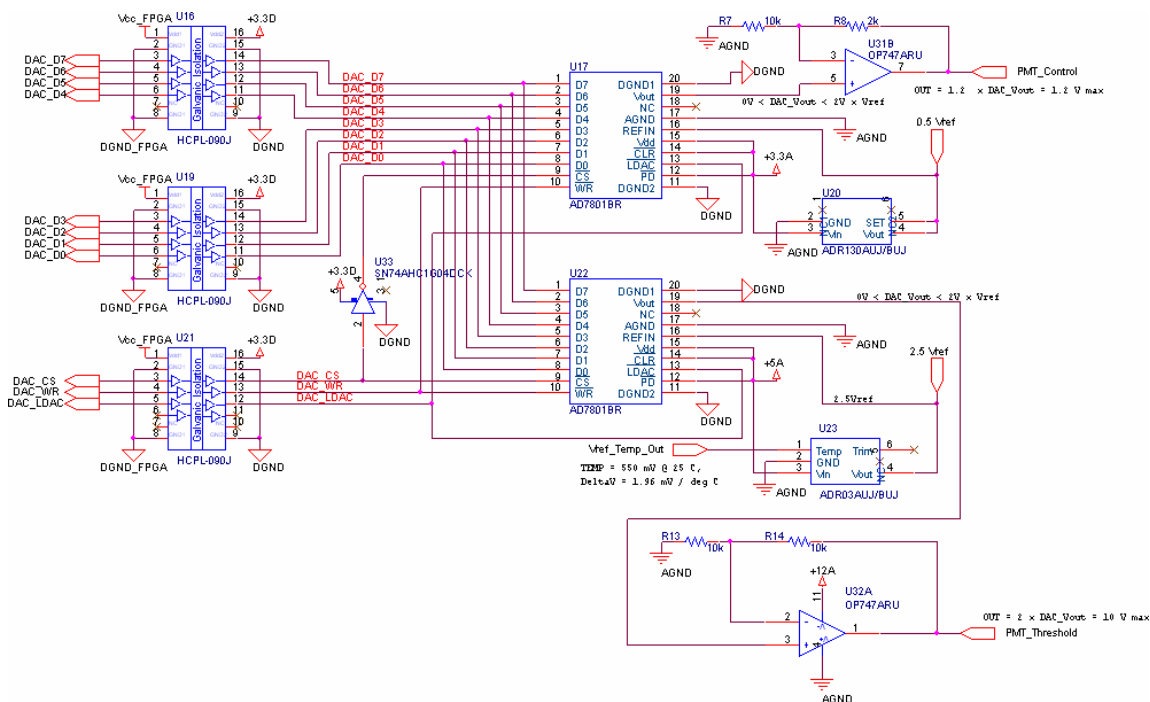
Figure 2.18: DAC Schematic for PMT Control Voltage

When the coincidence detector produced a positive edge, this indicated to the FPGA that the detected peak was valid, and the value would be passed to other software modules inside the chip for appropriate processing, storage, and transmission. If the FPGA detected a peak not accompanied by a positive edge from the trigger, the peak value would be ignored as noise.

The two options explored for the actual peak detection were either (1) direct sampling of the analog signal by an ADC or (2) analog peak detection topology that would track and hold the peak voltage until sampled by a lower-speed ADC (once triggered by the coincidence detector) and then cleared by an external source (likely the FPGA).

Direct sampling requires a fast ADC (on the order if MHz) to detect the quick pulses of the PMT, which generally implies more powerful ADCs and higher power consumption in the FPGA. In this topology, the actual peak detection would be accomplished in software. The advantages are that, if the algorithm is not accurately detecting the peaks, it can be fixed in software without modifying hardware. The alternative hardware option would require much slower sampling (~kHz) on the part of the ADC.

Ultimately, the direct sampling method was selected. The increased power consumption did not threaten the power budget, and it was determined that a digital algorithm would be faster and easier to debug than an analog algorithm, especially given that, due to long lead times, the PMTs would not be available for validation until late in the development cycle.

The sampling of the signal would be accomplished by an ADC. The selection of the ADC was driven by the characterization of the output signal arriving from the PMT. Figure 2.19 shows a pulse from the PMT acquired from an oscilloscope monitoring the direct output from the PMT. This pulse was caused by a muon that interacted with the scintillating crystal, which was fully aligned with the PMT aperture (maximum exposure). The PMT control voltage was set for 0.7 V. The data shows that, for this event, the maximum output voltage was 5.0625 V with rise and fall times of 2 μs and 15.4 μs, respectively. Again, this slow response is due to the performance of the selected PMT module.
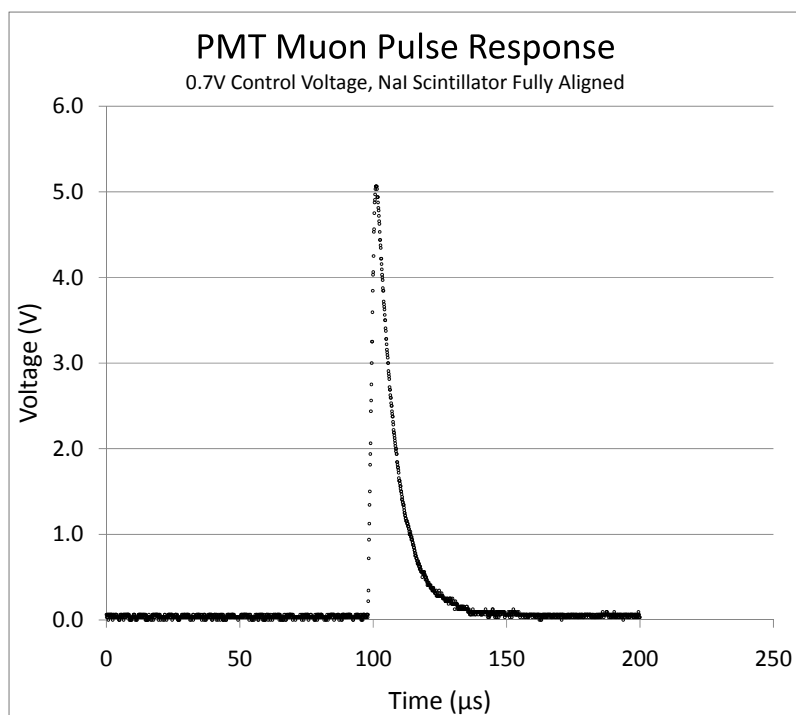
Figure 2.19: PMT Muon Pulse Response

As the peak output amplitudes would be stored in 128 binned energy ranges, one least significant bit (LSB) of an 8-bit system was deemed a minimum resolution to allow for 1 LSB of jitter. For the 10-V signal, the LSB of the 8-bit system corresponds to approximately 40 mV. Using the data in Figure 2.17, the time associated with a 40-mV drop from the peak voltage is observed to be 0.4 µs. Therefore, to accurately capture the peak voltage within 40 mV, the ADC should sample at least once every 0.4 µs, or at 2.5 MHz.

To increase the accuracy of the ADC, it was decided to select an ADC with at least one additional bit of resolution, and then to sample only the eight most significant bits in an effort to remove any ±1 LSB jitter. Also, since the sampling was relatively high speed, it was determined that a parallel data interface would be best. A parallel interface is easier to implement in software, requires much slower clock speeds, and there was more than sufficient I/O ports on the FPGA.

The AD9221/AD9223/AD9220 family of ADCs was selected to meet the requirements discussed above. The three components are pin-compatible ADCs that differ only in sampling speed and parameters that depend on it (specifically power consumption and timing). The AD9221/AD9223/AD9220 family of devices are 1.25, 3.0, and 10 Msps converters, respectively. Therefore, if later testing revealed that higher sampling rates were required, the 10 Msps AD9220 could be substituted with no additional hardware changes. If sampling rates could be reduced, the 1.25 Msps AD9221 could be used to conserve power or reduce clocking frequencies.

The other key features of the ADC family were 12 bits of resolution (only 8 of which would be used), parallel interface, on-chip voltage reference, 0–5-V sampling capability, single supply, and small outline package (SOP). Other parameters included small nonlinearity errors—0.5 LSB integral nonlinearity and 0.3 LSB dynamic nonlinearity— along with a 70-dB signal to noise ratio (SNR), and an 86-dB spurious free dynamic range (SFDR).

For the interface to the PMT, as described in Section **Error! Not a valid link.**, the gain of the PMT is controlled by an external voltage. In order to provide flexibility during flight, the science team required the gain to be controlled remotely from the

ground station in case the PMT output saturated, or was too low. A second (DAC) easily

met this need. Its voltage output would be buffered and then used by both PMTs as the

control voltage input. The schematic is shown in Figure 2.15 along with the comparator

threshold DAC discussed earlier in this section. Note that decoupling and bulk

capacitances are not shown in this schematic.

Environmental monitoring and control for the CDR baseline involved

temperature, voltage, and current. At this point, there was still a trade study to determine

how much autonomy for environmental control to place in the system versus human-in-

the-loop decisions using down-linked telemetry and uplink commands. This decision

was ultimately driven by software, so this section describes the hardware capability only.

The thermal team determined that passively cooling the system would be

sufficient, while active heating with patch heaters likely would be required. 5-kΩ

thermistors from YSI (±0.2°C GEM) were to be placed at key locations throughout the

payload for thermal monitoring. Thermally conducting, electrically insulating thermal

epoxy was to be used to encapsulate the circuit boards to aid in preventing isolated hot or

cold areas. The current sensors were to monitor the total current draw of the instrument,

in addition to the individual current draw of the power boards, C&DH, and the PMTs.

Voltage monitors would monitor the input and output voltage of the DC/DC converters.

The voltages from the current, voltage, and temperature readings would be multiplexed

through the ADG732 analog switch from Analog Devices into a dedicated ADC for

housekeeping sensors.

Active heating would be controlled by the FPGA through power MOSFETs

placed in series between a supply voltage and a resistive patch heater. If temperatures

began to get too cold, the FPGA would assert the MOSFET switch, either automatically in response to thermistor readings, or manually through an uplink command from the ground. Patch heaters were planned for the PMT and each of the PCBs.

2.6.2 Final Design

The final design encompasses the final flight circuit boards as they were designed. It does not account for post-fabrication modifications that were made in response to lessons learned from testing, verification, and validation. Those modifications will be described in detail in Section 2.6.3 and not discussed here. Note that the final documentation presented in the appendices illustrates the final designs with the post-fabrication modifications. That is, the documented schematics in the appendices show the schematics exactly as they were flown.

The final design accounts for the changes made since the CDR and includes both the addition of the pressure vessel and other changes as a result of additional testing and prototyping. At the system architecture level, due to space constraints, the plan for a multi-purpose FPGA board and a custom payload board was abandoned in favor of a single PCB that would encompass all C&DH and payload functions.

The largest change is the removal of the second PMT and coincidence detection. With this change, there was no longer a need for a DAC for the threshold voltage, the comparators, or AND gate for the trigger. The FPGA would no longer use a coincidence trigger to validate a detected peak—instead it would just record every peak above a certain threshold, which could be reprogrammed in software within the FPGA. The

threshold voltage was implemented to filter out the lower-energy signals that were not cosmic rays and instead mostly due to thermionic emission or stray electrons that began part way through the dynode chain and do not reach a full pulse height.   The other DAC was still retained for the control voltage, and the ADC would now serve as the only interface between the PMT and the FPGA except for basic signal conditioning and buffering.

The AD9223 ADC was still used as the converter for the PMT signal. The 3-Msps sampling rate was sufficient for the PMT signals (it was actually operated at 2.5 Msps during flight). Since the input range was only 0–5 V, the C&DH system used a divide-by-two voltage divider between the PMT (max output of 10 V) and the ADC (max input of 5 V). A unity gain amplifier was included to reduce any loading from the PMT or ADC, and Schottky diodes were included for protection to clamp the input voltage into the ADC to 0.2 V above or below the 0–5-V supply rails. The FPGA would continuously sample the PMT output and process the data.

Another major change was the removal of thermal control hardware. Later (incorrect) analysis indicated that staying warm would not be a problem in a sealed container given the estimated thermal power produced by the existing electronics and the addition of convective heating. Therefore, the C&DH board did not have power MOSFETs to control patch heaters.

Similarly, the plan to selectively power down the PMTs or parts of C&DH was eliminated. The complexity was deemed unnecessary and added more complications than possible solutions, especially in the now more compact schedule. Instead, a single temperature and pressure sensor was included that would be supplied with a primary

battery separate from the HASP system. That way, if temperature or pressure limits were violated, the main payload could be powered down by HASP (simply by switching off power to HEMI) and the sensors would still operate. The sensors would be monitored by the two analog channels provided by HASP so that the C&DH board was not necessary. Therefore, even though the safety pressure and temperature sensors were included on the C&DH board, they used a separate, dedicated power supply, and relied on HASP for communication.

The pressure sensor used was the ASDX015A24R manufactured by Honeywell. The part comes in a wide eight-pin DIP package and provides a sensitivity of 0.267 V/psi, which maps 0–15 psia (~776 torr) pressure to a voltage output between 0.5–4.5 V. The pressure sensor circuitry provided two outputs. The first was a full scale output so the team could monitor pressure from sea-level atmosphere down to the pressures that would cause the PMT to malfunction. The second output was a windowed circuit that provided a narrower resolution across a smaller pressure range in the lower pressure range around the PMT arcing pressure. This was to provide higher resolution around the sensitive pressures in case the vessel could not maintain the required atmosphere. If there was a slow leak, the plan was to operate the PMT right up until just before the failure point.

The safety temperature sensor was the same YSI 5-kΩ thermistor used in a voltage divider configuration with a bias resistor—the same design used throughout the rest of the instrument. Although the temperature sensor was not thermally stabilized, the response was calibrated across the full temperature range and a custom calibration curve was developed.

Since the safety sensors were required to operate independently of the rest of the HEMI instrument, the safety sensors operated from a dedicated 6-V-nominal battery pack consisting of four AA batteries in series located within the pressure vessel. The ground reference was the signal return for the HASP analog channels. Since the power and return signals were different than those supplied by the HEMI DC/DC converters, instrumentation amplifiers were used to interface the safety sensor outputs to the HEMI housekeeping circuitry included in C&DH. It was later discovered through HASP engineers that the HASP uses the same return path for all digital, analog, and power signals with no isolation. Therefore, instrumentation amplifiers may not have been necessary but are still a good design practice.

The final design retained the capability for housekeeping sensors using the multiplexer and ADC. The C&DH board provided for the measurement of 32 total housekeeping signals, with four of those hard-wired to C&DH monitors, 15 of those coming from elsewhere in the payload, and another 13 left as test point connections if future expansion was necessary.

2.6.3 Post-Fabrication Modifications

The most drastic post-fabrication modification was to correct the logic interface between the 3.3-V FPGA outputs and the 5-V MUX inputs. According the respective datasheets, the logic thresholds of the 3.3-V FPGA were compatible with the logic input thresholds of the 5-V MUX. However, while the circuitry functioned properly at first, after only minutes the C&DH board appeared to short circuit. After extensive debugging,

the problem was localized to an apparent short circuit within the FPGA core logic.

Replacing the FPGA resulted in a similar result (i.e. temporary successful operation

followed by a short) and the problem was isolated to the MUX. It was later decided that

leakage current from the MUX's 5-V supply was leaking into the FPGA output pins,

damaging the FPGA.

To fix the problem, the I/O signals were cut and passed through optocouplers that

were "dead bugged" to the existing PCB. This appeared to fix the problem, as the board

operated successfully for many hours without ever experiencing a fault.

Concern with the 3.3-V/5-V logic interfaces also prompted a re-evaluation of the

FPGA/ADC interface. Fortunately, the ADC allowed for 3.3-V digital operation while

the analog part of the ADC could still operate at 5 V (the required analog input range).

However, even with 3.3-V logic, the ADC required a 5-V clock to drive the system.

Therefore, the ADC clock input from the FPGA was also routed through a spare

optocoupler. This provided a voltage translation from 3.3- to 5-V logic, and removed

some of the overshoot and ringing on the clock line. The final C&DH circuit

documentation includes these additions. Additionally, Figure 2.20 shows the MUX and

ADC section of the board pre- and post-modification.
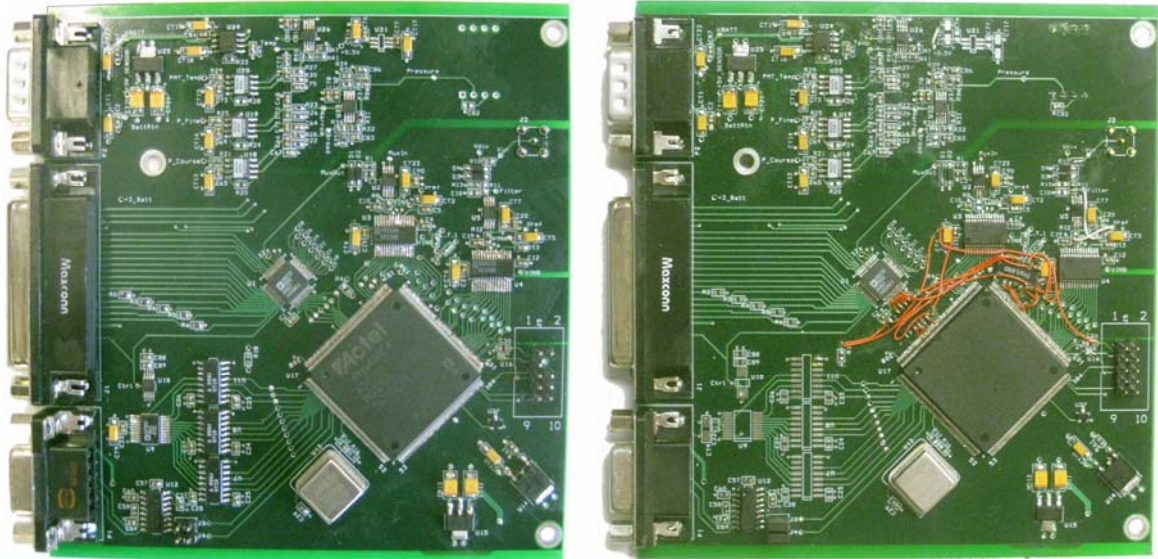
Figure 2.20: C&DH Board Before (*L*) and After (*R*) Post-Fabrication Modification

The interface for the DAC already included optocouplers by design, so the logic

interface was not an issue. However, although the DAC was verified to operate with the

FPGA, the software was not able to be completely integrated into the flight software

package and maintain enough time for testing. The PMT would cease to operate if the

DAC output was zero, or would break if it exceeded 1.1 V, it was decided to modify the

control voltage amplifier for a constant 0.6-V output rather than populate the DAC.

Since insufficient testing was completed with the DAC as an integrated part of the total

system for the team to have complete confidence in its performance during flight, the

DAC was left unpopulated on the flight board in favor of a fixed 0.6-V output created

from the DAC buffer and a voltage divider using the unused housekeeping ADC input

filter and 5-V supply.

Similarly, even though the software for the MUX functioned as desired, and the

hardware fix was identified, there was not sufficient time to incorporate the housekeeping

data into the final flight code and maintain an adequate test schedule. The two most important sensors, the safety and pressure sensor, were already being monitored by the HASP analog channels. Therefore, the MUX and housekeeping ADC were left unused (although they were populated). Removing the DAC and housekeeping drastically simplified the software (discussed in more detail in Section 2.7). In the tight schedule, implementing the science algorithms was the first priority. It was a difficult decision, especially since the wealth of planned temperature data would be valuable for the future long duration balloon.

The buffer amplifier was observed to greatly interfere with the PMT signal. The 28-MHz of the AD8655 amplifier was not sufficient for the PMT signal. As the amplifier would distort signals representing the bulk of the PMT pulse spectra, the amplifier was replaced with a short-circuit connection and verified to work as expected. There was some concern that, without the amplifier, the finite impedance of the ADC may load the PMT output; however, testing did not show this to occur.

2.7 Software

The software baseline at the CDR was significantly more complicated than what was actually flown. However, unlike many of the other subsystems, the majority of the changes were not because of the pressure vessel change, rather the changes were made to de-scope the software in a way that it could be completed in time for flight with enough testing and validation to ensure that the software would perform reliably during flight. Modules for housekeeping and thermal control were removed. The risk of not having

them was less than the risk of flying them untested and diverting precious software

validation resources from the resources needed to validate the science software

algorithms.

The software consists of two primary functions: (1) monitor the input PMT pulse

and detect each peak and (2) transmit the data to the ground

2.7.1 Peak Detection Software

Inside the PMT there is a trace amount of gasses and surfaces that can be ionized

by electron collisions. As the electron current flows through the PMT, the interaction

with the molecules of the residual gasses and surfaces in the PMT can produce electrons

and positive ions that, in turn, can strike the dynodes or photocathode. This interaction

then will produce secondary electrons that will appear at the output of the PMT as a

second pulse following shortly after the original pulse. To prevent false detection of this

"afterpulse" the C&DH detection algorithm implemented a 25-μs delay before the

algorithm would begin searching for the next peak which provides a max detection rate of

40 kHz. This simple dead-time delay is not the most optimal correction for afterpulse

mitigation, but it was deemed to be effective enough given the tight schedule for

development and testing.

2.7.2 Communication Software e

The communication software was adapted from RS-232/422 modules originally written by student Matthew Sunderland for SSPL's *NittanySat* satellite project. The modules were modified to meet different interface requirements and incorporated into the HEMI flight software package.

The RS-232 function consisted of three separate modules, one for transmit, one for receive and one to generate the baud clock used by the other two. The code was updated to match the HASP signal interface (eight data bits, no parity, 2400 baud, one stop bit) and to operate on the faster (50-MHz) C&DH clock. The updated module also used separate baud clock generators for transmit and receive functions to make the operations independent.

The uplink receive module required a finite delay in between received bytes to reset and sync to the new bit pattern. The official 16550 standard does not specify or require any delay, although delays between receive operations are allowed [*National,* 1995]. The HASP uplink data stream did not include any delay between one word's stop bit and the next word's start bit. While several fixes were identified, time did not allow for the complete testing and validation to implement the new algorithm, so uplink commands were not used during flight.

2.7.3 Data-Packaging Software

The original data downlink would package the science data alongside the housekeeping data using a telemetry matrix format previously used by past PSU student

projects on sounding rockets. Rather than sending the cosmic ray pulse peak value immediately as it occurred, the peaks were to be placed into energy bins to form an energy spectrum. The full spectrum would be transmitted every second along with a single measurement from each of the housekeeping sensors.

The design was to be implemented using a dual-RAM configuration, where new data would be stored to one block of RAM while the older data would be transmitted. Once the transmission was complete and the next new set of data was complete, the transmit RAM block would be cleared and used to collect the next data set, while the most recently completed data set would be transmitted from the other RAM block. Table 2.2 shows the originally planned telemetry frame. Each cell represents an 8-bit word. The synchronization (SYNC) and sub-frame ID (SFID) words are used to identify the specific data words in the asynchronous bit-stream. The SCI1 through SCI128 represents the 128-bin energy spectrum for the science data. The remaining cells represent various housekeeping voltage, current, and temperature readings throughout the instrument. At 7×32 cells with eight data bits and two overhead bits (start, stop) per cell, a full data frame would have been 2240 bits. This requirement is what prompted the HASP and HEMI team to lower the allocated bandwidth from 4800 baud to 2400 baud.

Table 2.2: Planned Downlink Telemetry Frame

SFID	SCI1	SCI33	SCI65	SCI97	TEMP 1	SYNC
SFID	SCI2	SCI34	SCI66	SCI98	TEMP 2	SYNC
SFID	SCI3	SCI35	SCI67	SCI99	TEMP 3	SYNC
SFID	SCI4	SCI36	SCI68	SCI100	TEMP 4	SYNC
SFID	SCI5	SCI37	SCI69	SCI101	TEMP 5	SYNC
SFID	SCI6	SCI38	SCI70	SCI102	TEMP 6	SYNC
SFID	SCI7	SCI39	SCI71	SCI103	TEMP 7	SYNC
SFID	SCI8	SCI40	SCI72	SCI104	TEMP 8	SYNC
SFID	SCI9	SCI41	SCI73	SCI105	TEMP 9	SYNC
SFID	SCI10	SCI42	SCI74	SCI106	TEMP 10	SYNC
SFID	SCI11	SCI43	SCI75	SCI107	TEMP 11	SYNC
SFID	SCI12	SCI44	SCI76	SCI108	TEMP 12	SYNC
SFID	SCI13	SCI45	SCI77	SCI109	TEMP 13	SYNC
SFID	SCI14	SCI46	SCI78	SCI110	TEMP 14	SYNC
SFID	SCI15	SCI47	SCI79	SCI111	TEMP 15	SYNC
SFID	SCI16	SCI48	SCI80	SCI112	TEMP 16	SYNC
SFID	SCI17	SCI49	SCI81	SCI113	CURR 1	SYNC
SFID	SCI18	SCI50	SCI82	SCI114	CURR 2	SYNC
SFID	SCI19	SCI51	SCI83	SCI115	CURR 3	SYNC
SFID	SCI20	SCI52	SCI84	SCI116	CURR 4	SYNC
SFID	SCI21	SCI53	SCI85	SCI117	CURR 5	SYNC
SFID	SCI22	SCI54	SCI86	SCI118	CURR 6	SYNC
SFID	SCI23	SCI55	SCI87	SCI119	CURR 7	SYNC
SFID	SCI24	SCI56	SCI88	SCI120	CURR 8	SYNC
SFID	SCI25	SCI57	SCI89	SCI121	VOLT 1	SYNC
SFID	SCI26	SCI58	SCI90	SCI122	VOLT 2	SYNC
SFID	SCI27	SCI59	SCI91	SCI123	VOLT 3	SYNC
SFID	SCI28	SCI60	SCI92	SCI124	VOLT 4	SYNC
SFID	SCI29	SCI61	SCI93	SCI125	VOLT 5	SYNC
SFID	SCI30	SCI62	SCI94	SCI126	VOLT 6	SYNC
SFID	SCI31	SCI63	SCI95	SCI127	VOLT 7	SYNC
SFID	SCI32	SCI64	SCI96	SCI128	Control V	SYNC

2.7.4 DAC Software

The DAC software was developed and verified to work with the FPGA and DAC used by C&DH. However, due to schedule constraints, the DAC software was not able to be integrated into the final flight software package.

The module would continuously update the DAC with the 8-bit value stored in a register within the module. If C&DH had wanted to change the DAC output, it would simply update the data register, and on the next DAC update, the new value would be sent to the DAC. Although not flown, the Verilog code is included in the appendices.

2.8 Power

The power system was the one that was least affected by the adoption of a pressure vessel. Power required by the payload systems was reduced with the removal patch heaters and parts of C&DH, and the physical dimensions constraining the power circuit boards were reduced with the implementation of the pressure vessel. Other than these changes, the power system requirements remained the same. A final change, unrelated to the pressure vessel, was the decision to change the PMT supply voltage from ±12 V to ±15 V. This simply required changing the DC/DC converter to a different converter within the same product family. Therefore, all external filtering and monitoring circuitry remained the same. The following discussion on the power system only describes the final as-flown design.

2.8.1 Requirements and Baseline Design

The HEMI pathfinder required ±15 V for the PMTs; 5 V for the payload electronics and environmental monitoring circuitry; and 3.3 V and 1.5 V for the FPGA. It was determined that the power system would provide the ±15 V and 5 V supplies and

the lower positive voltages would be generated locally at the FPGA with linear regulators. Input power was supplied by the HASP system at a nominal 30V and maximum 500 mA from a fused supply.

The −15V supply requires a DC/DC converter to create the negative voltage. While linear regulators could be used to create the 15-V and 5-V supplies, the large drop from 30 V makes this design inefficient. Therefore, the power system used DC/DC converters for ±15-V and 5-V supplies.

To create the 3.3-V and 1.5-V supplies, DC/DC converters were deemed unnecessary. The power loss in the linear regulators would be comparable to the efficiency losses of the typical DC/DC converter, and additional converters can add unnecessary switching noise to the system. Furthermore, regulators are generally lower cost parts and available in very small form factors with minimal external component requirements for the low current requirements of this design.

A preliminary search of available DC/DC converters identified several models that matched the power requirements of the system. The ideal converter must be capable of supplying sufficient power for the system. In addition to increased size and cost, an over-capable design is also power inefficient as well. DC/DC converters usually require a minimum percentage of the rated current draw in order to maintain regulation. Furthermore, many converters are optimized to be more efficient towards the rated current output. Far below the rated current output, switching losses in the converter dominate the power loss, and efficiency suffers.

Once several models with appropriate power ratings were selected, the next primary concerns were managing noise and thermal issues throughout the system.

Excessive ripple current generated by the switching topology of the converters can cause errors throughout the system. Also, the power output capability is de-rated as temperature increases, so thermal management is important—especially when the design is targeted to operate in a vacuum and not a pressure vessel.

Of the converters considered for this design, the WP06R series from C&D Technologies demonstrated the best characteristics for the considerations listed. Specifically, the converters used were the WP06R24S05NC and WP06R24D15NC for the +5-V and ±15-V lines, respectively. The WP06R series contained superior thermal and EMI characteristics, largely due to the device's metal-case packaging. The device operates within the −40 °C to +100 °C range, which provided more range than alternative converters. Also, the metal case and encapsulated components help minimize hotspots within the converter and dissipate heat into the surrounding system. For the purposes of EMI shielding, the metal packaging of the WP06R improves the EMI shielding of the device. The WP06R series also provides many voltage output and input options within one physical package and footprint, meaning that one physical board design can be used both the 5-V and dual 15-V parts.

Although the rated output power of the WP06R parts is higher than what is likely required by this mission, the power requirements were not well defined when these parts were originally selected. It was determined that allowing for extra capacity was worth the sacrifice in efficiency. Furthermore, if line regulation suffers with the lower power draw, then external load resistors can be added to increase the current draw.

2.8.2 Filter Design

Filtering the switching noise from the converters was the primary design concern for the power system. Insufficient noise performance in past student-designed power systems necessitated last-minute redesigns [*Schratz,* 2006]. Given HASP's tight schedule, that redesign effort could not be repeated here.

DC/DC converters convert voltages through the charging and discharging of a capacitor at a given frequency. A simplified model of this operation is shown in Figure 2.21. For these particular models, this frequency was fixed at 200 kHz. Therefore, there will be some ripple present on both the input and output power lines at the primary switching frequency plus at higher order harmonics.
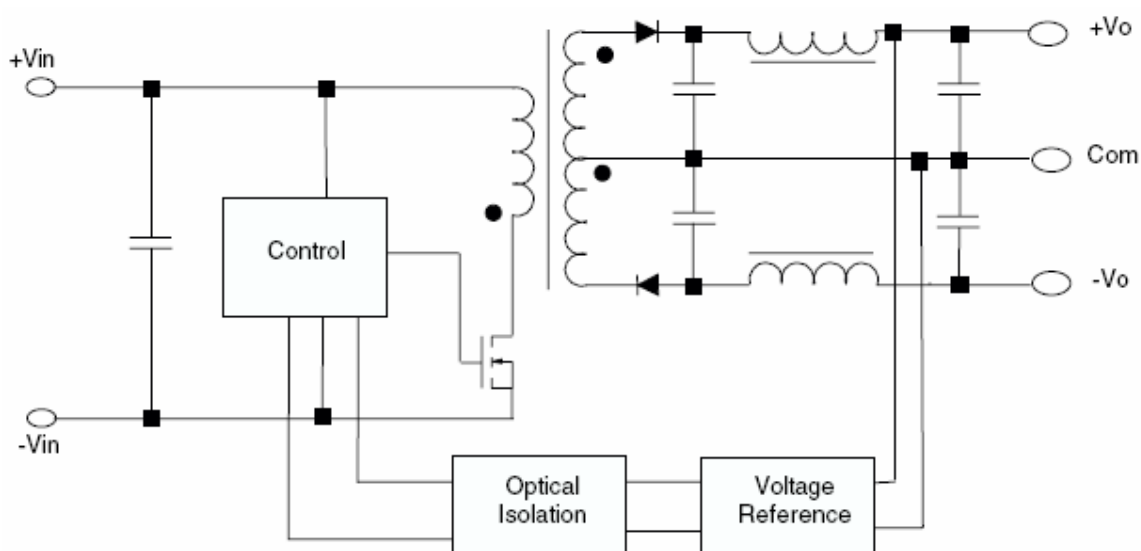
Figure 2.21: Simplified Schematic of the WP06R DC/DC Converter
[*Murata,* 2008]

Noise present on the output lines could interfere with the sensitive analog circuitry throughout the payload, and noise present on the input lines could interfere with

other student payloads or the HASP system itself. The converter datasheet quotes a maximum 50-mV$_{pp}$ ripple voltage. However, the quoted ripple voltage from the high voltage DC/DCs within the PMTs module was only 5 mV. Therefore, filtering was designed to lower the power supply noise below the noise floor of the instrument electronics.

The performance of the converters was immediately tested and Figure 2.22 shows the power spectrum of the WP06R24D12 ($\pm$12V) converter supplying 110 mA at both $\pm$12V. At input power to the DC/DC under these conditions was 66 mA at 27.997 V. Note the first peak at the primary switching frequency (determined to be 228 kHz instead of the specified 200 kHz) followed by the next harmonic at ~456 kHz. The power at the first peak, $-$32.37 dBm, corresponds to voltage (in V) referred to a 50-Ω load.
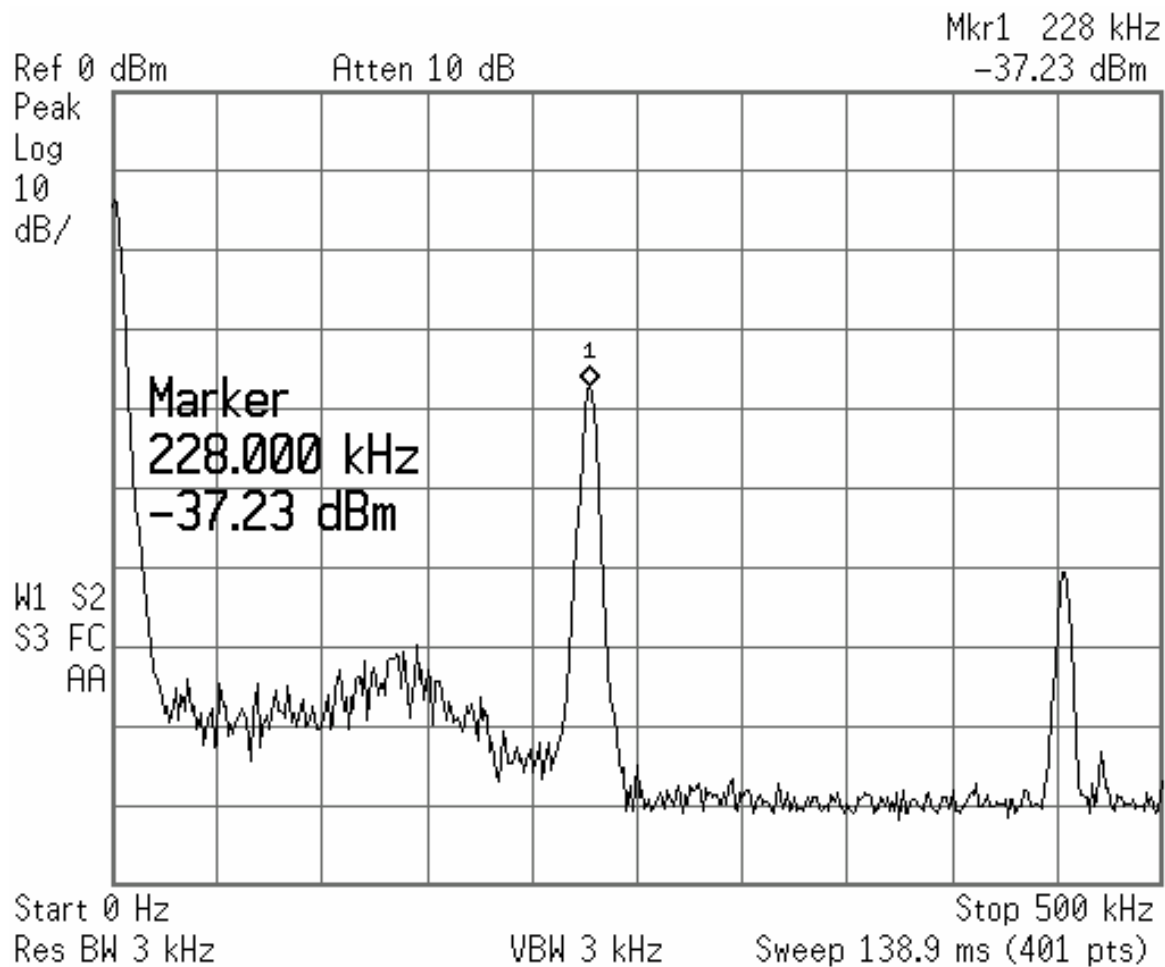
Figure 2.22: Unfiltered Output of the WP06R DC/DC Converter

A simple LC filter on both the input and output lines is a common configuration for converter filters. Figure 2.23 shows this topology, which obeys the transfer function described by

$$T(s) = \frac{1}{s^2 LC + s\dfrac{L}{R_{load}} + 1}.$$

2.4
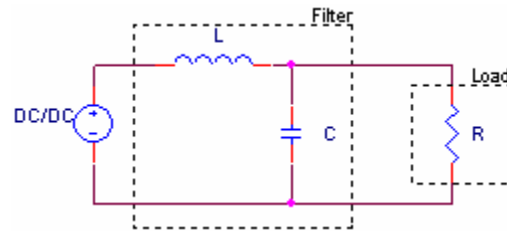
Figure 2.23: LC Filter Topology

Using LC components, as is described above, a resonance can occur if there is not enough inherent damping from the load or parasitic resistances (usually small). Therefore, a series resistor and capacitor was placed in parallel with the load as shown in Figure 2.24. This adds a damping factor to the circuit transfer function. Modeling with MATLAB showed little sensitivity to resistor values between 10 Ω to 10 kΩ. The capacitor was 0.1 µF.
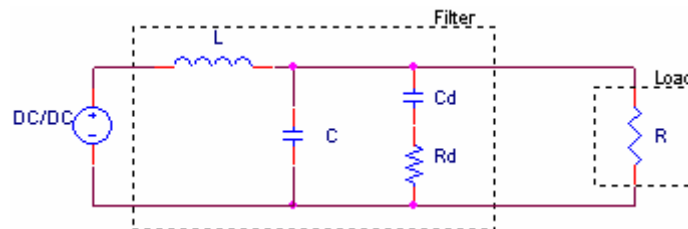
Figure 2.24: Damped LC filter

Figure 2.25 shows that the simulated response of the filter provides 67 dB of attenuation at the specified switching frequency (200 kHz), and 70 dB of attenuation at the observed switching frequency (225 kHz).
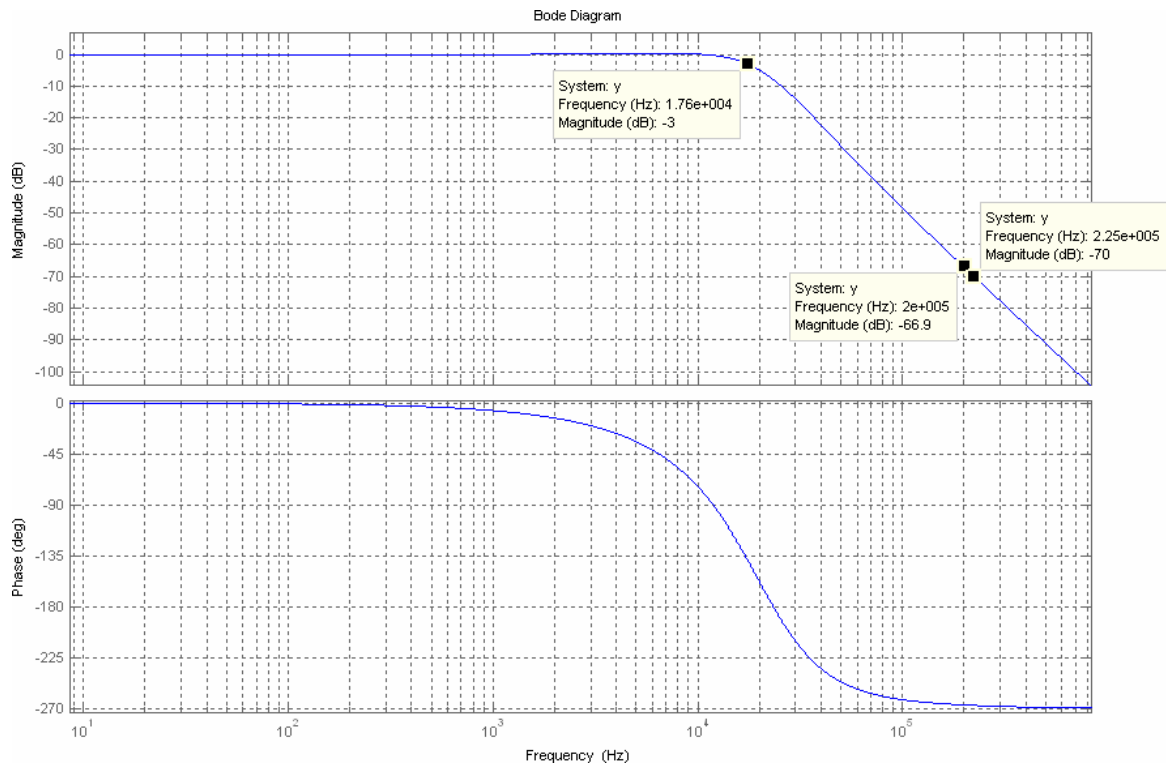
Figure 2.25: DC/DC Converter Filter, Simulated Response (Final Design)

2.8.3 Final Design

Each input and output of the 5-V and 15-V DC/DC converters used the filter

shown in Figure 2.24. As this filter provides 20-dB attenuation, and the design goal was

60 dB, each input and output filter used three repeated stages of the filter to provide the

required attenuation.

2.8.4 Post-Fabrication Modifications

There was little post-flight modification for the power boards—due mostly to early prototypes that validated the successful performance of the filters with these converters. The only post-fabrication changes were related to parts of the design that were modified or added after the prototype boards were verified. The largest change was that the footprints for the large filter capacitors were too small and very close together. The smallest capacitors available could only fit only by placing one capacitor on the pads designed for two parallel capacitors (parallel footprints were used to halve the required capacitor values and therefore reduce cost). The halving of the filter capacitance (from 30 μF to 15 μF) reduced the performance of the filter. However, testing showed that the noise suppression was more than adequate so that the performance loss was tolerable. The updated simulated response is shown in Figure 2.26.
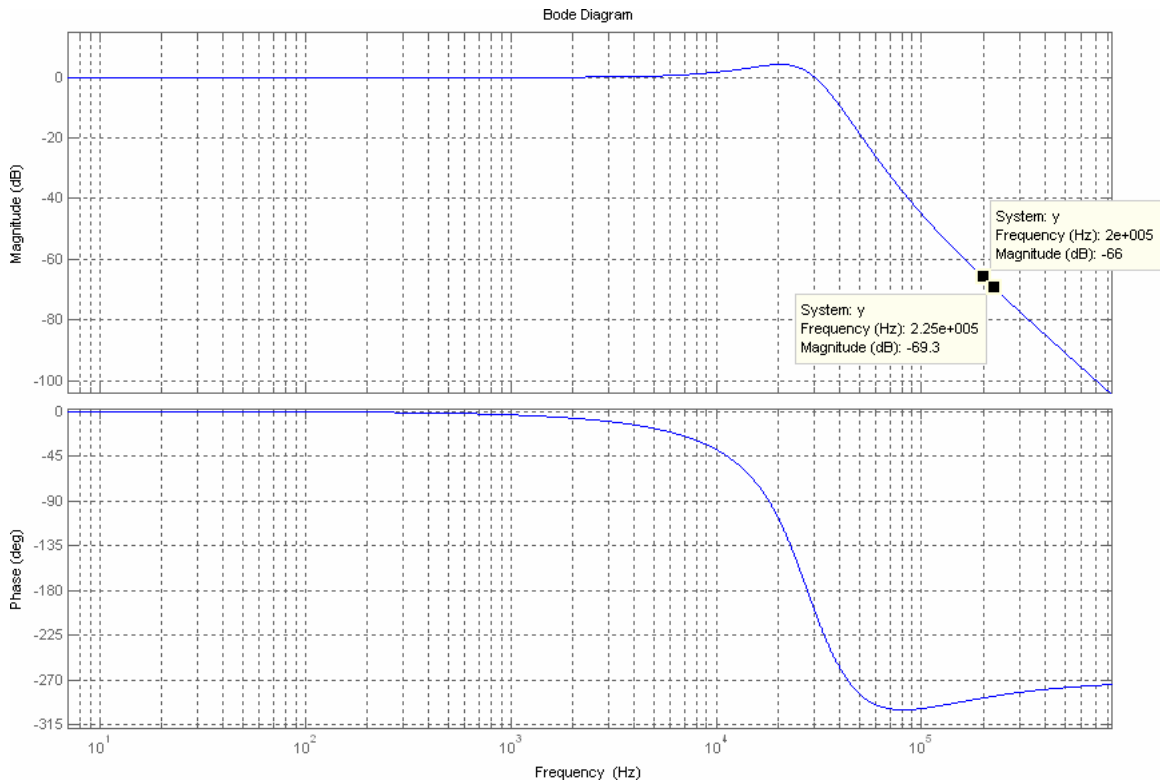
Figure 2.26: Simulated Filter Response (Flight)

Another addition after prototyping was the addition of input and output current sensors. The design used the AD623 instrumentation amplifier to measure the small voltage drop across a small series resistor. However, the common-mode voltage of the instrumentation amplifier was too small so the current sensors did not function properly. The final flown boards left the current sensors unpopulated.

The positive voltage sensors were simple two-pole low-pass Sallen Key Butterworth filters. The negative voltage sensors used the single-ended MFB configuration rather than the Sallen Key. Although the monitors worked as expected, since the final C&DH designs did not include the monitoring sensors, the power voltage sensors were populated, but never used.

2.8.5 Testing

Testing the DC/DC converter power supply with an external electronic load validated that the DC/DC converter with input and output filters could supply the regulated, clean powers required by the system. The figure below shows that any peak is at the noise floor of the system, at least −88 dBm.

However, testing did reveal that, because of the large capacitance used in the filter designs, there was a large start-up transient in-rush current spike. Setting the bench power supply current limit slightly above the expected current draw of the converter produced a periodic sawtooth-like waveform as the converter repeatedly tried to start with insufficient transient power. Using the N6705A DC Power Analyzer from Agilent, the team was able to determine that, although the nominal current draw for the converter is about 100 mA, the turn-on transient could be anywhere between 200–450 mA. Once the bench power supply current limit was increased to 300 mA, the converter would quickly recover from the transient and enter nominal operation. Since the current transient was less than the HASP-allocated 500-mA current limit, no further mitigation steps were taken.
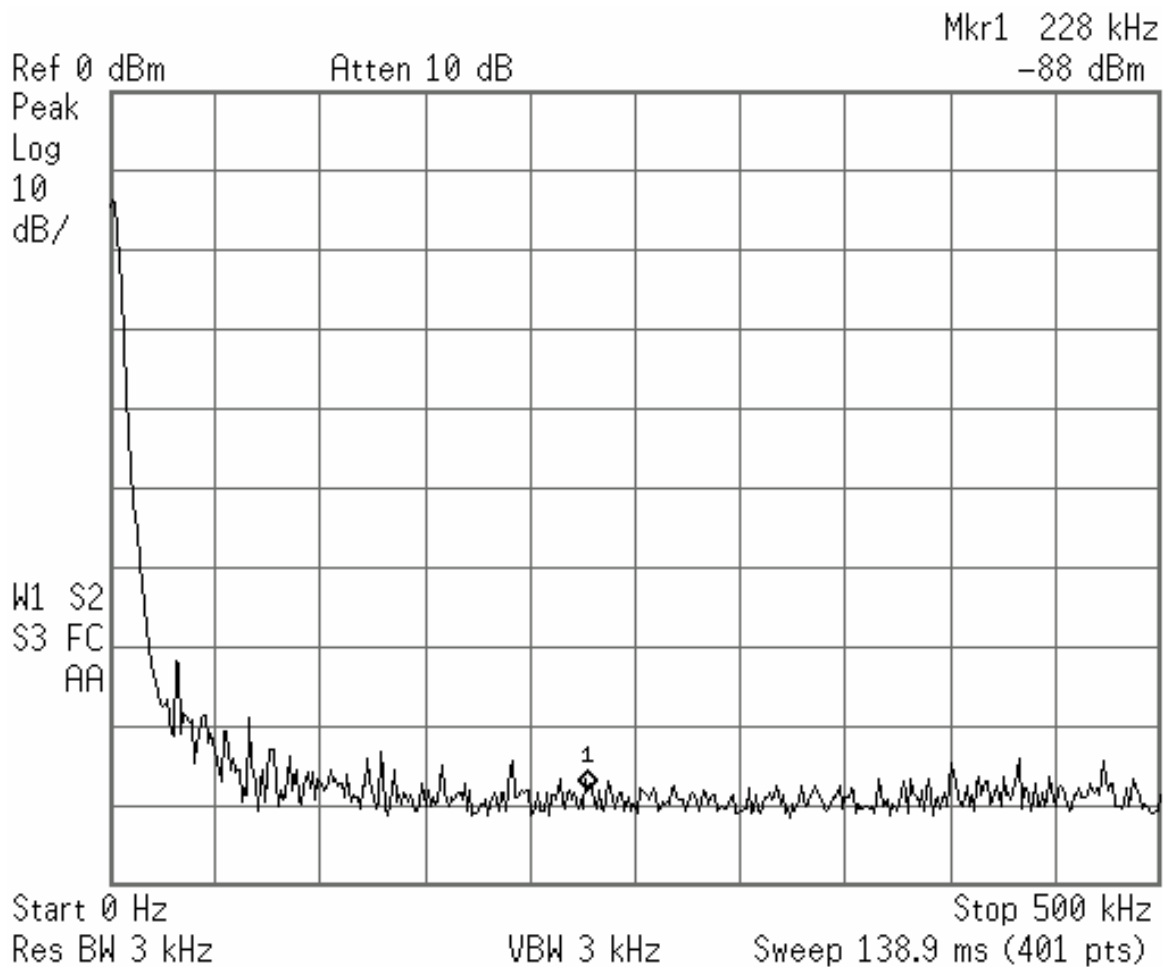
Figure 2.27: Filtered Output of the WP06R DC/DC Converter

2.9 Structure

2.9.1 Requirements and Baseline Design

The HEMI mechanical subsystem was tasked with providing the primary structure

that would interface to HASP per the requirements set by the small class payload

specifications in the HASP Student Payload Interface Manual. The subsystem was also

responsible for providing the secondary structure that allowed the detector and supporting

electronics to mount to the primary structure. The design also had to satisfy the

requirements of the science and thermal subsystems. HASP interface requirements for a

small class payload are set forth in the HASP Student Payload Interface Manual.

Condensed requirements for the payload are as follows:

- Ability to withstand a 10-g vertical and 5-g horizontal shock without separating from HASP.
- Have a total mass of no more than 3 kg.
- Have a footprint of no greater than 15 cm × 15 cm and a height of no more than 30 cm. In certain areas, the structure may extend beyond the footprint, and specific parts of those areas require the overhang be two inches above the plate. See Figure 2.28 for the location of these areas.
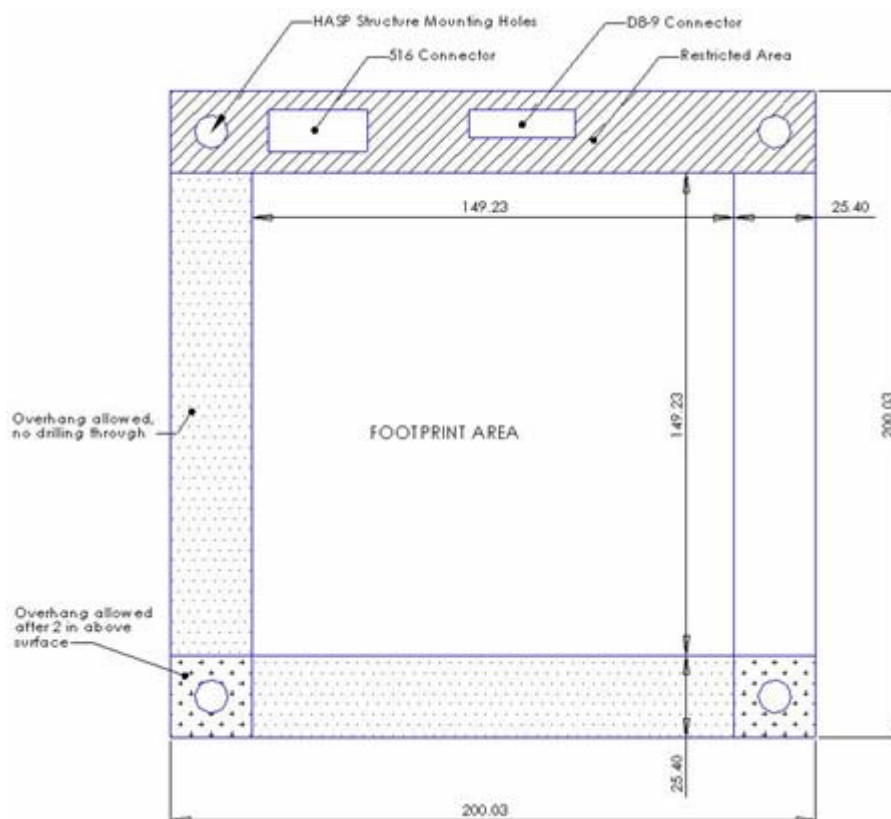
Figure 2.28: Regions of the PVC Mounting Plate for the HEMI–HASP Interface

The science and payload team's requirements affected the structure above the electronics housing. The structural components supporting the detector should not cause interference with measurements by causing secondary particles, i.e., there needed to be maximum exposure from the crystal to the external environment with minimal, or no, metal near or surrounding the crystal. Also, the structure needed to allow for patch heaters, which would maintain the narrow temperature range required for operation of the compact PMT modules.

Since the mechanical design was completely re-designed once the pressure vessel requirement was imposed, the discussion on the early mechanical baseline is discussed in Appendix I, rather than in the primary discussion of this thesis.

2.9.2 Final Design

The final design was a complete redesign from the CDR baseline because of the requirement that this be a pressure vessel. The primary driver in the redesign effort was the mass allocation combined with the small physical footprint. Extensive searching produced no commercially available structure that was within either the cost or schedule allowances of the project. Instead, commercially available products were used as guidelines for the first new revision. Analysis of the structure allowed for iterative optimizations that maximized the internal volume while minimizing mass and maintaining sufficient factor of safety. The analyses of the final structure are shown in Figure 2.29.

Bottom Shell (Post Fab), Flight Conditions   **Top Shell (Post Fab), Flight Conditions**
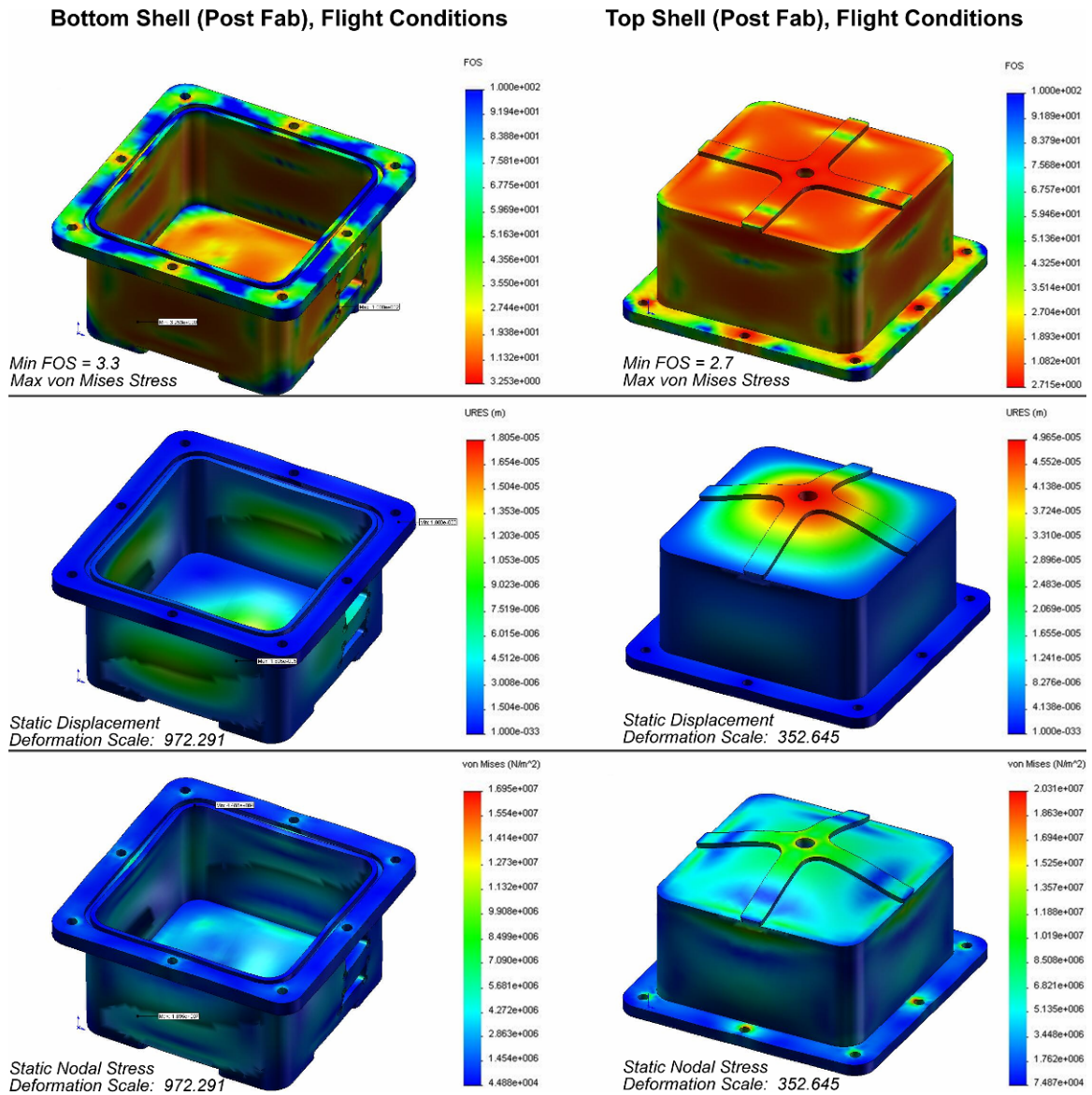
Figure 2.29: Finite Element Analysis of Structure Designs

A cross pattern was added to the base of both the top and bottom halves of the vessel. The pattern added strength to the weakest part of the design while contributing little mass. A hole for a release valve was included at the intersection of the cross pattern to release any pressure that might develop inside the vessel. There was a fear that the vessel may develop small internal vacuum during temperature and pressure testing that

would make it difficult to separate the two halves. The release valve allowed easy venting of the vessel if required.

The HASP team originally requested that HEMI include a burst disk that would automatically rupture if a certain pressure was achieved. Their concern was that somehow the pressure vessel could explode and the shrapnel would damage the balloon or the HASP system. Analysis showed that if the pressure vessel were to fail, air inside the vessel would slowly leak out of the seal. A slow leak over several hours could be devastating to the instrument, which required a minimum ambient pressure to function, but a slow leak would have no effect on HASP. The factor of safety was enough to ensure that an explosive failure was impossible.

The area of most concern with the vessel was the seal between the two halves. A literature search showed that the tongue-and-groove O-ring seal was the most effective for this application. Vacuum grease would be added to help seal any pores from machining. There is a wide variety of O-ring materials and eventually the Buna-N material was selected as it would operate over a wide temperature range and does not react with vacuum grease.

As the structure mass was directly related to volume, the internal volume of the structure had to be minimized, which is why the second PMT was removed. As mentioned in the beginning of Chapter 2, even with the remove of the second PMT, the mass was still 1.3 kg over the 3-kg mass limit and a waiver from HASP had to be obtained.

To further reduce mass, the FPGA and payload PCBs were combined. The boards would now fit vertically into the structure, sliding into guide rails that minimized

the spacing between them. A two-connector, nine-pin hermetic D-subminiature connector on the bottom half of the structure allowed electrical power and data signals to pass through the structure.

The PMT was fastened to an H-shaped bracket using existing mounting holes in the PMT module. The PMT bracket and electrical PCBs slid between two grooved plates, then the entire assembly slid into the pressure vessel. The only other components not connected to the grooved plates were the hermetic D-subminiature connector and the safety sensor battery back. The battery pack was glued with RTV onto a free side of the vessel.

The last addition to the structure was a separate mechanical mount for an external toggle switch to connect or disconnect the safety sensor battery from the circuitry. This allowed the vessel to be sealed with the batteries at any time before flight without worrying that the batteries would discharge. The HASP team was instructed to turn the safety sensor power on when launch ops began. Figure 2.30 illustrates all of the HEMI pathfinder mechanical components.
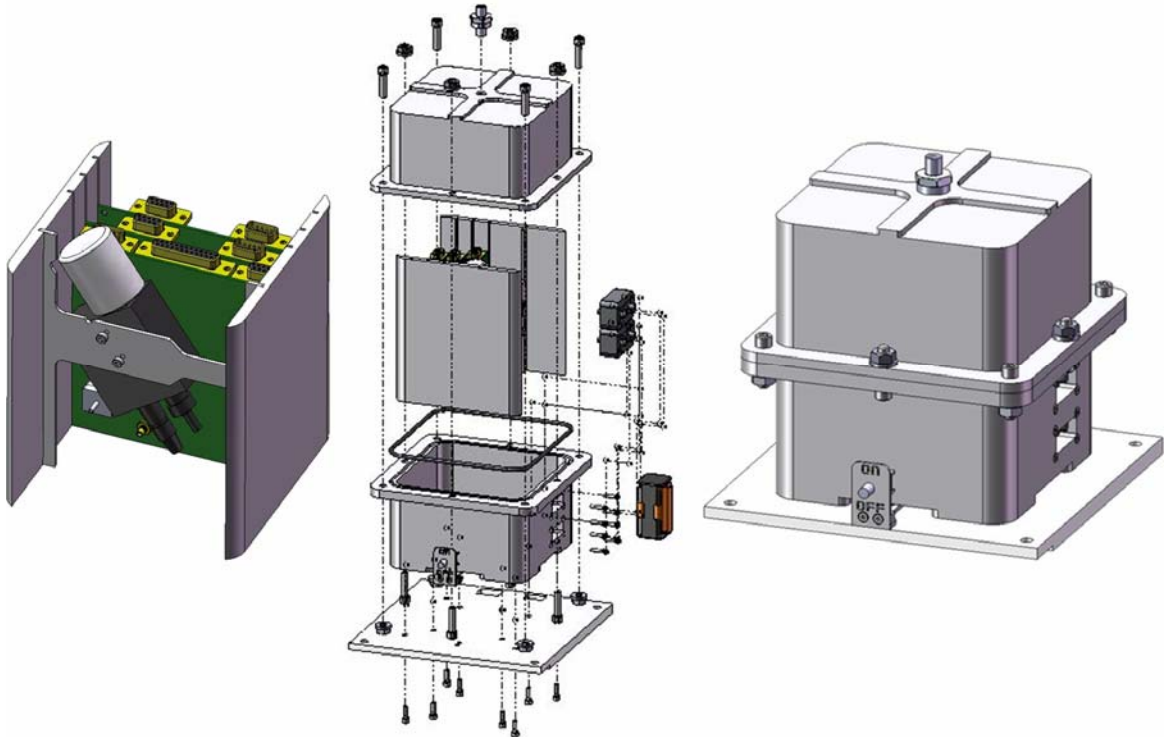
Figure 2.30: Final Mechanical Primary and Secondary Structure

2.10 Thermal

In hindsight, the HEMI pathfinder thermal design was one of the major oversights of the project that drastically affected the quality of the data. Active thermal control was not included, and the flight experience clearly confirms that this was an incorrect decision.

2.10.1 Requirements and Baseline Design

The thermal design was driven by the PMT temperature range, which required an operating environment of 5 °C to +45 °C and a storage environment of −20 °C to +50 °C. The expected ambient environment ranged between −40 °C to +20 °C based on past flight data. As the instrument was mounted on booms away from HASP, it was exposed to Earth's albedo which provided some radiation during the day and night and specifically helped mitigate the worst-case cold temperatures at night.

As described above in Section 2.6.1, the baseline design at the CDR included patch heaters that would be controlled by C&DH, either autonomously or controlled remotely through command uplinks. Two low cost and readily available patch heaters were purchased for evaluation and tested in the SSPL thermal vacuum chamber along with thermistor temperature sensors that would be used to monitor temperatures throughout the payload.

The use of heat-conductive, electrically-insulating epoxy was also explored to distribute heat throughout the electronics, and to mitigate extreme hot or cold spots. Specifically, the epoxy commercially available through McMaster-Carr (PN 66395A11) was considered for its thermal conductivity of 10 Btu-in./ft.^{2}-hr.-°F and its dielectric breakdown of 410 V/mil.

2.10.2 Final Design

The final analysis concluded that heaters would not be necessary as the heat generated by the electronics and ambient radiation would suffice to keep the payload

warm. Therefore, the plan for the C&DH and the power subsystems to include support for patch heaters was abandoned. Furthermore, thermally conductive epoxy was also not used.

2.10.3 Post-Fabrication Modifications

During integration with the HASP host system, the HEMI pathfinder and the rest of the student instruments were put through a thermal–vacuum test while integrated with the HASP structure. The test was the first indication to the team that the thermal requirements of the instrument may not be met as the HEMI temperature dropped to between -40–-50 °C. However, the HASP test used a vacuum barely below ambient atmospheric pressure, and the thermal transfer mechanism was significantly affected by convection, rather than the radiation that would be experienced in flight (ice began to develop on the instrument). This was meant to test far beyond the most extreme environment anticipated on HASP, so the team found this test to be alarming, but inconclusive.

After integration with HASP, the HEMI team retained the instrument to make final modifications. As a precaution, in response to the HASP environmental test, the team decided on a quick-fix solution to add patch heaters without drastically modifying existing electronics. A patch heater would be placed on the internal metal structure and connected to the HEMI main 30-V power supply from HASP through a mechanical latching relay. As one of the other student payloads was removed from the flight, there was an empty pair of discrete command lines (28-V momentary pulses) that could be

used to switch the mechanical relay open and closed, thereby controlling power to the patch heater. Using the data from the self-contained safety temperature sensor, this provided a last-ditch, human-in-the-loop, closed-loop thermal control system.

The necessary hardware was produced and the instrument wire-harness adapted. However, the system would only have access to a cursory interface test with the HASP host system once the instrument was re-integrated on the flight line just prior to launch. Furthermore, the short time between integration and flight did not allow a full, rigorous validation of the design. To use the spare discrete lines, the HASP wire harness would also have to be modified on the flight line. As it turned out, flight-operations logistics did not allow for the rewiring of the discrete lines, so this option could not have worked.

There was a concern that the untested system could malfunction and cause the rest of the instrument to fail also. If for some reason the heating circuit were to fail in a way that caused a short-circuit, the power to HEMI pathfinder would be completely cut and the HEMI pathfinder flight would be a failure. The final decision was to operate the instrument during the day when the temperatures were warmer and, if necessary, remove power to the instrument during the night when temperature dropped. Heaters were not included, and the added thermal control circuitry was removed.

As the following sections will describe, active thermal control should have been included, and a detailed thermal model should have been developed and validated.

2.11 Ground Support Equipment

LabVIEW, a graphic-oriented software development package from National Instruments, was used extensively throughout this project to interface between the A/D prototypes developed by C&DH; integration and test equipment automation for environmental testing; and eventually with the flight instrument for ground testing and evaluation. Building on these earlier efforts, the original Ground Support Equipment (GSE) interface was developed using LabVIEW. The program served as a decommutator for the serial bit stream coming from HEMI pathfinder in real-time and during testing, or it accepted and parsed a binary file of the raw data during flight operations, during which the data downlink was handled by HASP and sent to the universities in binary data files.

The program was originally designed to provide an instantaneous view of the science data and the many voltage, current, and temperature sensors located throughout the payload. During testing, it would also provide the command uplink function that would be provided by HASP during flight. When the final design de-scoped all but the science data, the LabVIEW interface was unnecessary and was changed to a simpler MATLAB script. However, the final product of the interface was very successful and is worth describing briefly as a template for future efforts.

The interface consisted of four tabbed panels. The first panel, shown in Figure 2.31, was the main setup screen, which provided the user with the options for configuring the RS-232 serial data interface (for ground testing) or the data files (for flight operations).
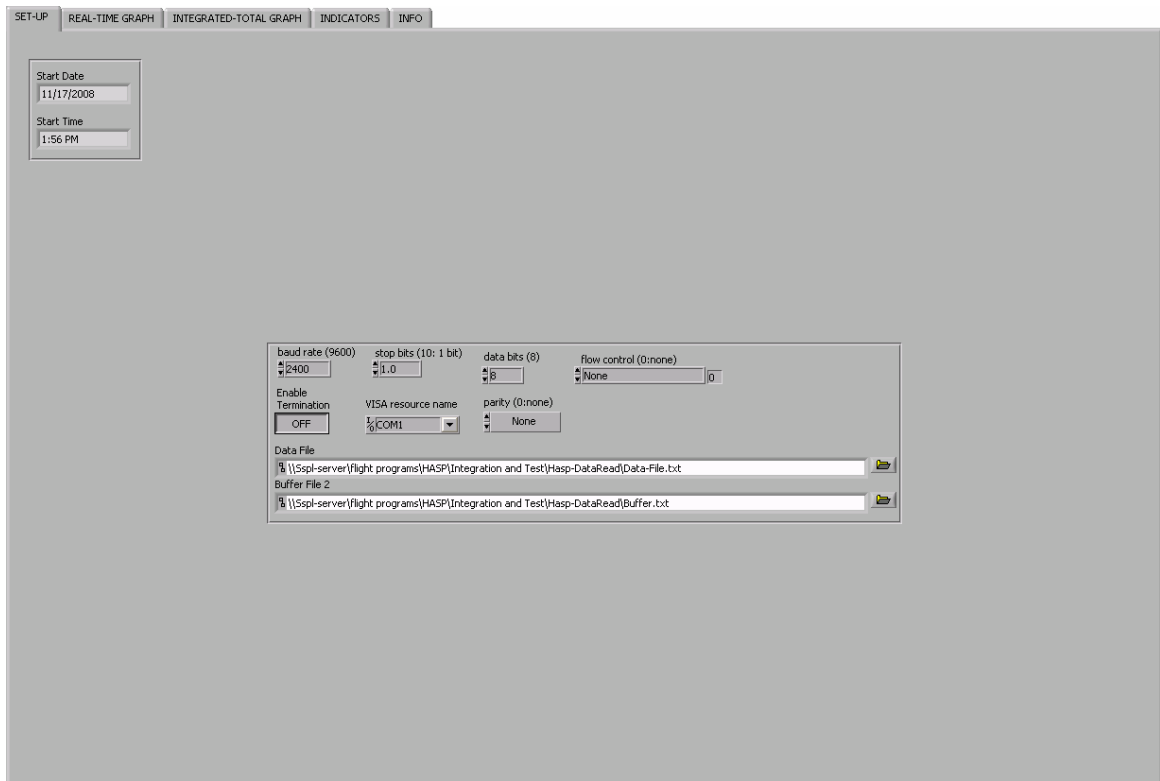
Figure 2.31: LabVIEW Operations Setup Panel

The next two panels provided different views for displaying the science data. One would display the peak voltages detected as a function of time in a scrolling view similar to an oscilloscope. This is especially useful during testing when known signals are generated, and the response can be monitored in real time, and the data simultaneously recorded.

The other science data view would display the science data in a spectrum form— where the peaks for a fixed time are sorted and graphed similar to the test data described throughout this thesis. This view allows the user to quickly monitor the energy spectra produced by the detector in near real time—the interface is only slowed by the user-specified time duration of the spectrum.

79

Figure 2.32, summarizes the voltage, current, and temperature data throughout the payload. The amount of expected data was the primary motivation for developing this interface. This interface allows for real-time and simultaneous monitoring of all instrument sensors. Pre-programmed and adjustable limits are selected, which generate warnings and errors if they are exceeded.

Figure 2.32: LabVIEW Environmental Monitoring Panel

Chapter 3

Integration, Testing, and Calibration

This chapter describes the methods for the testing and calibration of individual

components and the integrated instrument. Initial testing began early in the project, and

was continued as thoroughly as possible throughout the project within the imposed

schedule constraints. These tests were carried out with the intent to verify that the

technical implementation of the instrument would perform as expected during operations,

and to provide a calibration of the detector across all expected flight conditions.

3.1 Pressure Vessel Validation

Once the pressure vessel requirement was added to maintain an atmosphere above

~12 torr for the PMTs, members of LSU's HASP team required that the vessel be tested

in a relevant environment to ensure that the vessel would not damage the host flight

system. Given its robust design and the pressure differential between the ambient and

internal atmospheres, the HEMI team did not feel that destructive failure was of primary

concern. Rather, the more likely failure mode was that the vessel would slowly leak,

causing the internal pressure to drop below operating limits.

A thermal–vacuum test was planned and carried out to ensure that the vessel

presented no risk to the host flight system and would reliably maintain a sufficient

atmosphere throughout the entire flight.

The test was conducted using the thermal–vacuum chamber located in the Electrical Engineering East Building at The Pennsylvania State University. The test was conducted over a period of two days. For the first 24 hours, the temperature was held constant, demonstrating the air-tight quality of the vessel. The second 24 hours involved thermal cycling, which placed the vessel beyond the temperature extremes expected during flight in order to illustrate the durability and safety of the vessel. For the duration of the test, pressures outside of the pressure vessel were maintained between 500 mtorr and 10 torr to simulate the pressures expected during flight.

Data was collected via thermistors and electronic pressure sensors located inside and outside of the pressure vessel. In addition to collected data, the expected internal pressures were calculated for comparison with the ideal gas law, $PV = nRT$, where the ratio nR/V is constant for this experiment. Volume may change slightly due to thermal expansion and contraction, but the effect is small enough to be disregarded in and computations for this test.

The pressure test of the HEMI-HASP vessel was conducted with the purpose of demonstrating the vessel's ability to survive beyond the extremes of expected flight conditions based upon calculations by the thermal subsystem using previous flight data provided by LSU and from data gathered from thermal coating information. As such, the thermal cycling during this test mimicked that of the flight in profile, but durations were elongated in order to demonstrate the stability of pressure, i.e., that the vessel would not leak, and temperatures have been taken to 10–15 °C beyond expected extremes. Figure 3.1 shows the measured and expected internal pressures alongside the measured ambient temperature inside the vessel. There was an error in the automated data logging

software that caused data to be lost for a period of about five hours during the vessel's

cold soak. However, since the pressure remained constant before and after the data

dropout, the test was still deemed satisfactory.

At $t = 24$ hours and $t = 34$ hours, the vessel was subjected to a cold thermal cycle,

and the data illustrated in Figure 3.1 show a sudden pressure decrease corresponding to

the temperature decrease in each case.
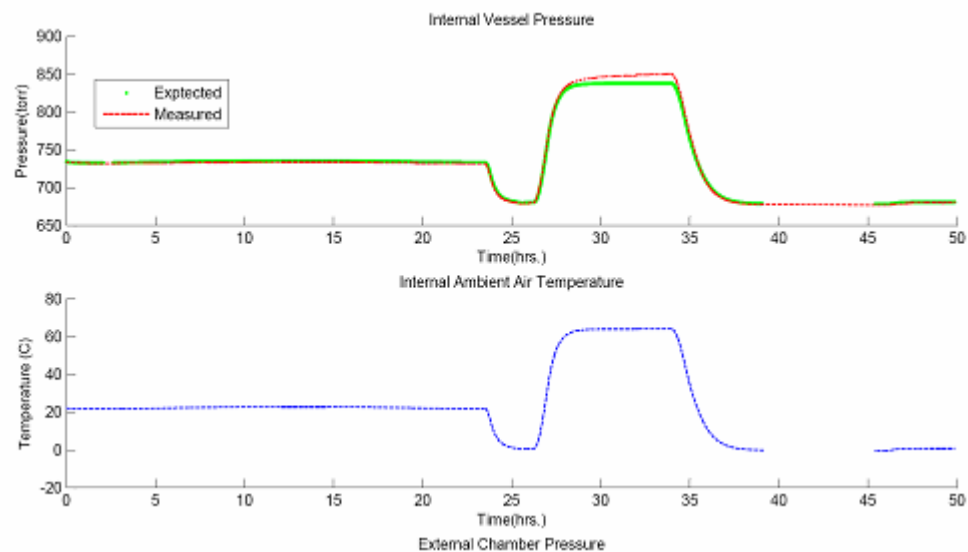
Figure 3.1: Pressure Vessel Thermal–Vacuum Test: Pressure and Temperature

The applied temperatures from the thermal cycling system caused the internal

pressures to fluctuate as expected. Figure 3.2 shows that the ambient air swung slightly

wider to the hot and cold extremes than the vessel itself. The thermal cycling system of

the test chamber does not allow for direct heating or cooling of the entire vessel. Instead,

only the base was conductively heated or cooled, which does not yield evenly distributed

temperatures. The temperature gradient of the vessel lowers after a long period, but a

small difference exists between the internal air, which is as cold or hot as the average

vessel temperature, and the measured vessel temperature, which is measured at a single

point.
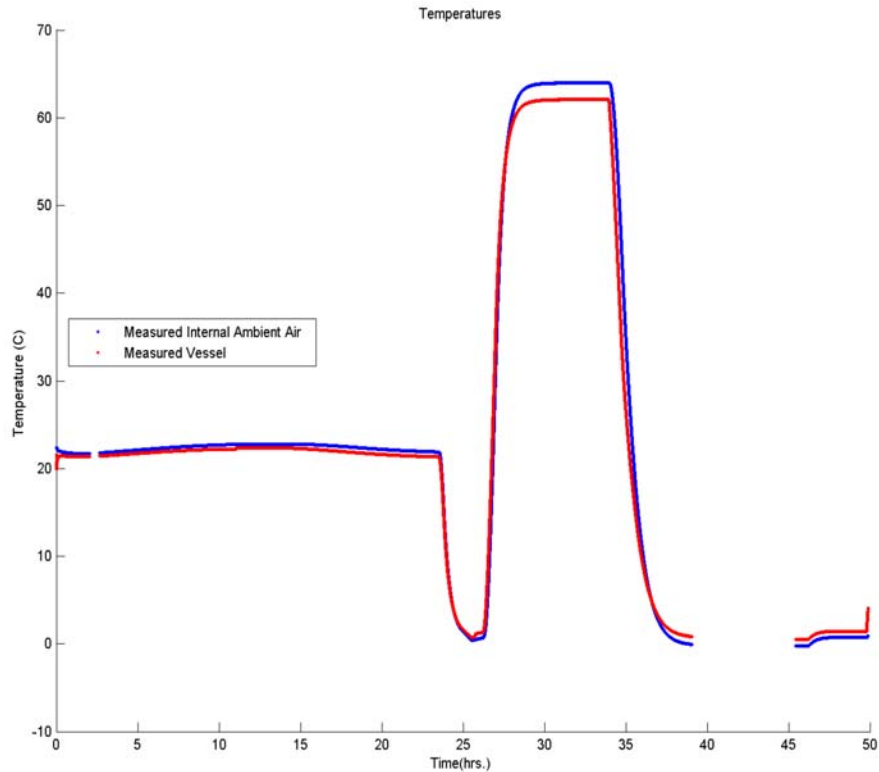
Figure 3.2: Pressure Vessel Thermal–Vacuum Test: Ambient and Vessel Temperatures

The measured internal vessel pressure exactly follows expected temperatures

when the vessel is cycled to low temperatures, demonstrating that the low extreme

temperatures do not cause the vessel's seals to fail. This also indirectly illustrates the

previously discussed pressure stability, as the two portions of cold testing both follow

expected pressures, which are identical for both parts, so no significant air could have

leaked out between those two parts of the test.

Between the cold thermal cycles, the vessel was subjected to extreme hot

conditions, approximately 10 °C above the expected maximum temperature. The

resulting temperature of about 65 °C drastically increased the internal pressure of the vessel. This is the most likely time for the vessel to fail, as internal pressures are at their highest, and the increased temperatures will affect the shore hardness of the Buna-N O-rings sealing the vessel flange, the hermetic D-sub feed-through connectors, and the vent opening.

At $t = 27$ hours, the hot thermal cycle began, and the measured pressure change shown in Figure 3.1 correlates nicely with expected data. As the graphs illustrate, the internal pressure climbed slightly above the expected values. These errors were deemed to be within the limits of the test equipment calibrations and other non-idealities and indicate that the test is still valid. The data provide evidence that the vessel does not leak at high temperatures and pressures. This test shows that is that the vessel survived all required environmental conditions without any structural damage, and no significant volume of gas was lost from the vessel.

3.2 Safety Sensor Calibration

The thermistor used for the safety sensor calibration was assembled and tested in SSPL's cryo chamber across the predicted temperatures during flight. The test produced the calibration curve illustrated in Figure 3.3.
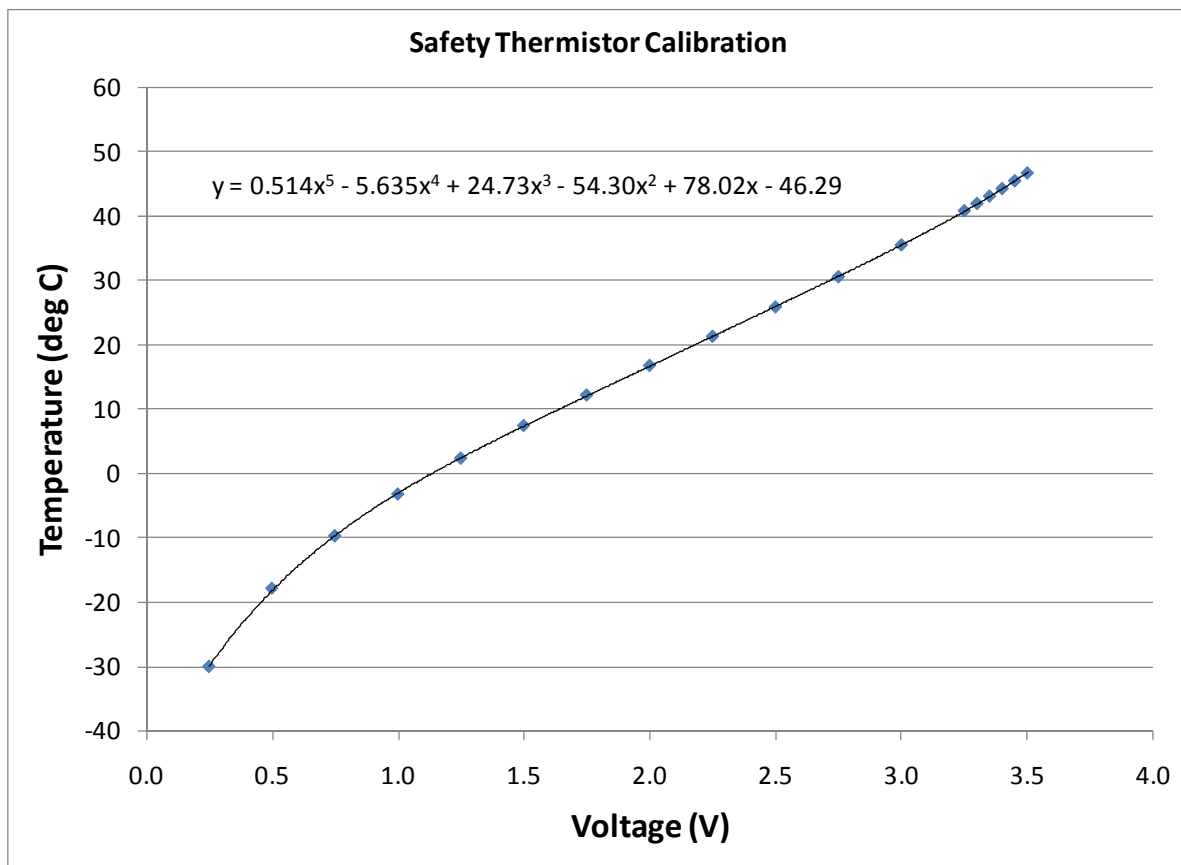
Figure 3.3: Safety Thermistor Sensor Calibration

3.3 C&DH Assembly & Calibration Test Results

The C&DH boards were assembled according to a detailed step-by-step procedure that is formally documented in SSPL document number 5004-06-12 (see Appendix G). All assembly and board-level test data are stored there. Significant calibration results are presented for the safety temperature sensor in Section 3.2 above, and for the peak detection validation throughout Chapter 3.

3.4 Instrument Calibration

Prior to flight, extensive testing was conducted on the PMTs in order to

adequately characterize their response across all expected conditions and to verify that

they would survive the balloon environment.

3.4.1 Test Setup

The general test setup used an Agilent 54622D oscilloscope and an Agilent

E3631A power supply controlled and monitored by an external computer through a GPIB

interface and using a custom MATLAB script for automation (included in appendices).

Illustrated in Figure 3.4, the oscilloscope was used to monitor the output signal from the

PMTs. One or two channels were used for single- or dual-PMT configurations,

respectively. A bench-top power supply provided the ±15-V supply voltages and the 0–

1.2 V control voltage recommended for each PMT.
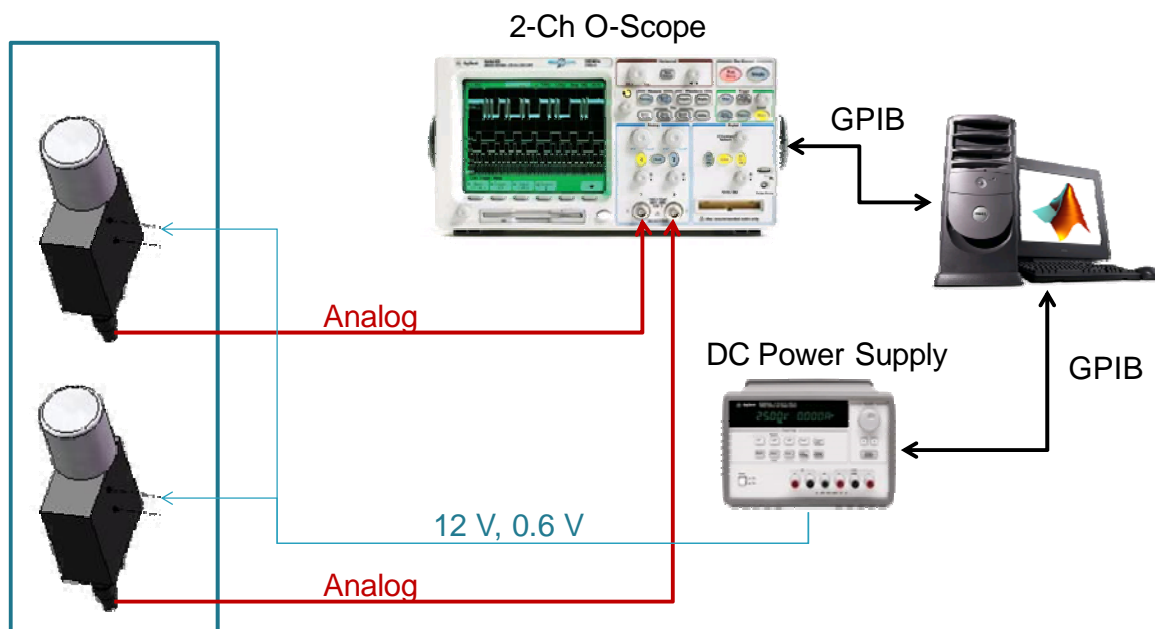
Figure 3.4: Detector Calibration Test Configuration

A single-trigger threshold value was set manually by the user before each test to exclude the low-voltage pulses caused by dark current. When the MATLAB script initialized, it would place the oscilloscope into a single-trigger mode and then wait for a pulse to trigger the scope. When a pulse occurred, the scope would signal the MATLAB program that a valid pulse was on the screen, at which point the program would query the scope for the maximum voltage, base voltage, rise time, fall time, and pulse width. All currents and voltages from the power supplies were also similarly recorded. As soon as the data was collected for that pulse, the program would set the scope back into single-trigger mode to capture the next pulse.

The GPIB interface is not a high speed interface, nor is the scope designed for high speed data acquisition. Therefore, there is about a one-second delay between when the scope is triggered (stopped) and when it is set to trigger again. Occasionally pulses

would occur during the sampling period and consequently would be lost. However, for simple muon detection, the expected rate is one about every three seconds. Therefore, it was concluded that the missed pulses would not drastically affect the data over long test durations. The MATLAB program runs autonomously until stopped by the user.

Where two PMTs were used, the scope would monitor the product of the two signals (calculated using the scope's 1*2 MATH function). Therefore, if only one PMT produced a signal—likely due to thermionic emissions—then the product of the pulse with the almost-zero baseline would still be almost zero. Only a pulse from both PMTs would trigger the scope and, consequently, the MATLAB program's sampling routine.

The PMT-and-crystal assembly was placed inside a vacuum chamber with all windows covered in Tedlar (light time material plastic sheet) to keep the system light-tight. Using the vacuum chamber was the quickest solution to provide a sealed environment with electrical pass-through connections. Unless specified, all the tests occurred at ambient pressure. The chamber provides a 10-pin circular connector for electrical pass-through and two additional BNC connectors for more sensitive signals. The oscilloscope, power supplies, and computer were located outside the chamber and the power and signal lines were connected through the chamber connections.

Note that the C&DH board eventually used for flight has an almost instantaneous reset time except for the intentional dead-time delay for afterpulse mitigation described in the peak detection algorithm discussion in Section 2.7.1 Therefore, when the automated MATLAB test data is compared to the C&DH flight configuration data, the statistics are generally the same, except the count rates are higher—especially for thermionic emission pulses.

3.4.2 Single PMT Configuration, Varying Aperture

Figure 3.5 shows the data from a test using a single PMT and crystal. No additional radiation source was used. The graph shows the number of occurrences (counts) of specific peak voltages throughout the test. Note that the lowest voltage recorded is around 0.4 V, which was the manually set trigger threshold of the scope. The smaller peaks below ~1 V are due to noise in the detector system. The next peak is distributed around 2.4 V, which is due to muon particles.
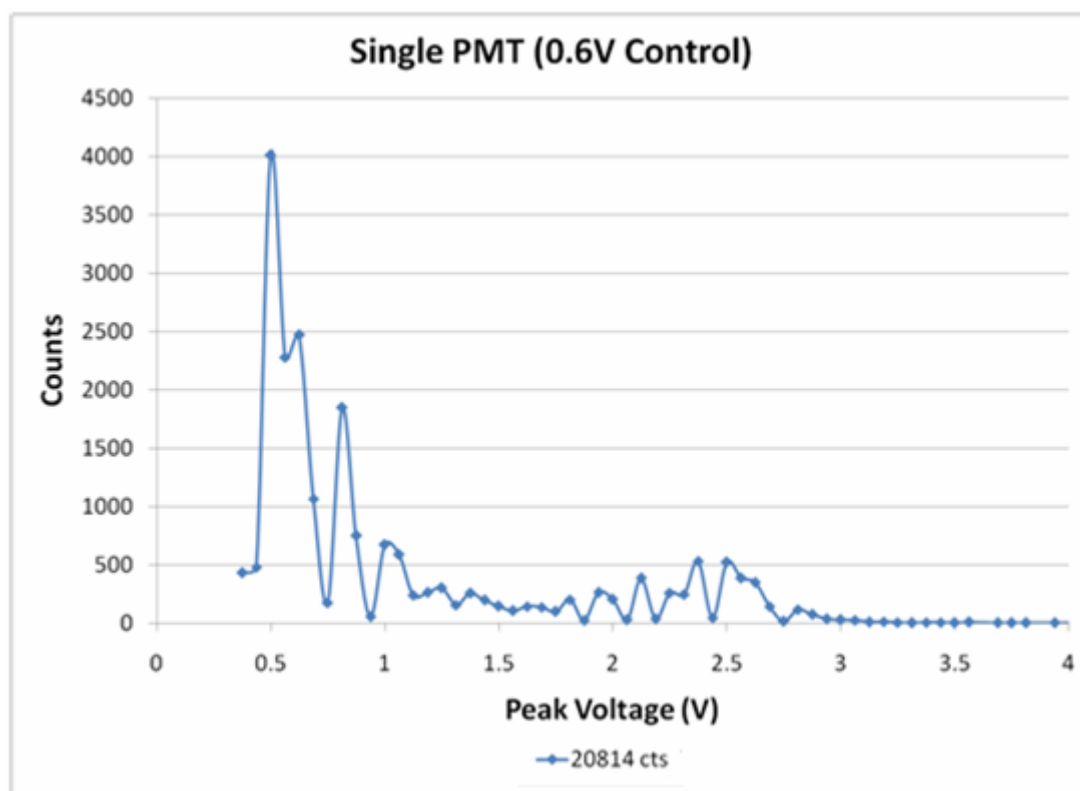

Figure 3.5: Single PMT, Full Aperture

The distribution around the muon peak is expected to be a Gaussian-shaped peak as the path lengths of the particles through the crystal (and therefore the energy deposited) vary based on the incident angle of the particles. One will notice that the peaks of the scope test data do not have the expected smooth distribution, rather it has jagged peaks. It is hypothesized that rounding and the slow acquisition time is the cause of the peaks.

Before the HEMI pathfinder instrument was packaged for transport to the Ft. Sumner launch site, one last test was performed. For this test, the scope triggered on a debug signal from the FPGA indicating the internal FPGA trigger was activated. Both the scope data and the direct data from the instrument were recorded. Again, the instrument is faster than the MATLAB and GPIB test equipment so the sampling time was limited by the test equipment. The result is shown in Figure 3.6
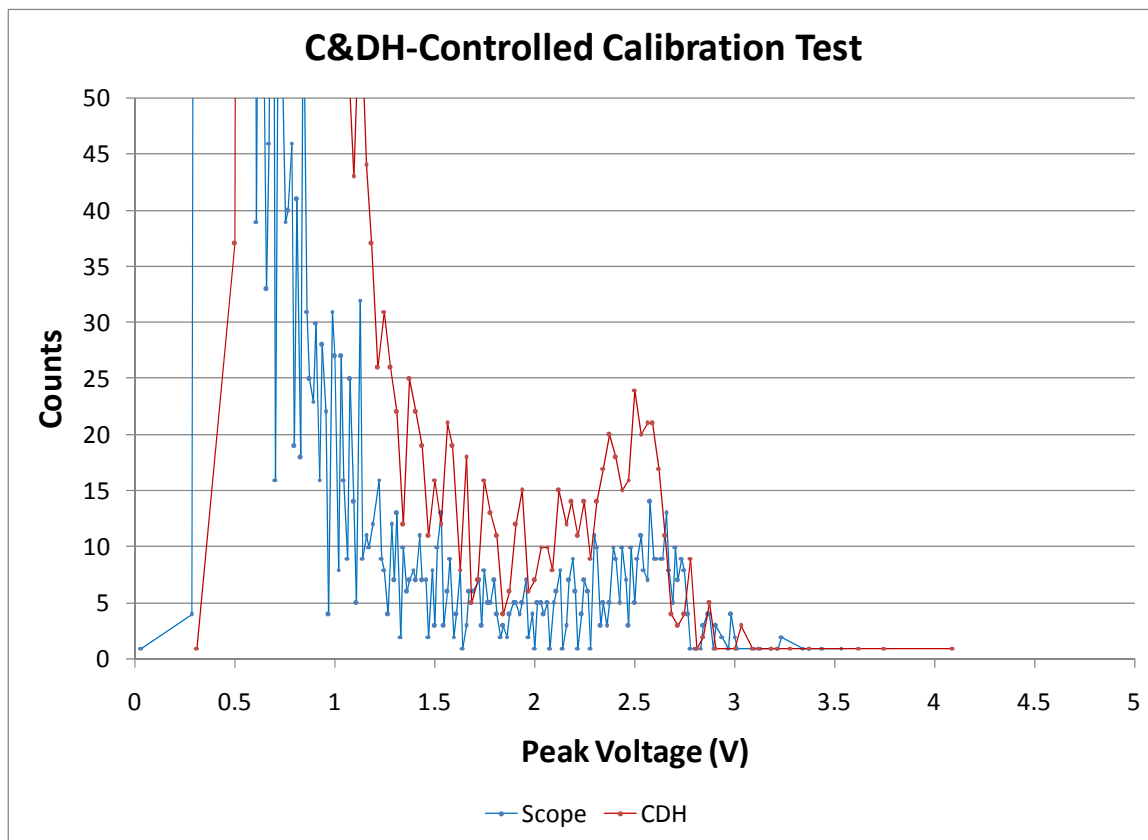
Figure 3.6: Pre-Ship Scope Test Using C&DH Trigger

Notice that the scope and C&DH curves track each other well. The peak of the
muon distribution is slightly offset for the two data sets, but this is likely due to
differences in the peak detection algorithms used by the scope and the C&DH design.
Note also that the peaks are less jagged than when measured using the scope trigger, but
jagged peaks still exist.

Figure 3.7 shows the results of data logged directly from the C&DH system in the
complete flight configuration. The scope was not involved in the test setup so no delay
was present except for the short 25-µs delay purposely programmed into the peak
detection algorithm (see Section 2.7.1). The internal threshold for the detection

algorithm was set higher than previous tests in order to drastically limit the amount of noise so the data downlink would contain mostly muon or higher-energy particles rather than noise. If the data were too noisy, there was a chance that significant points would be missed while the system was acquiring the peak of a noise pulse.
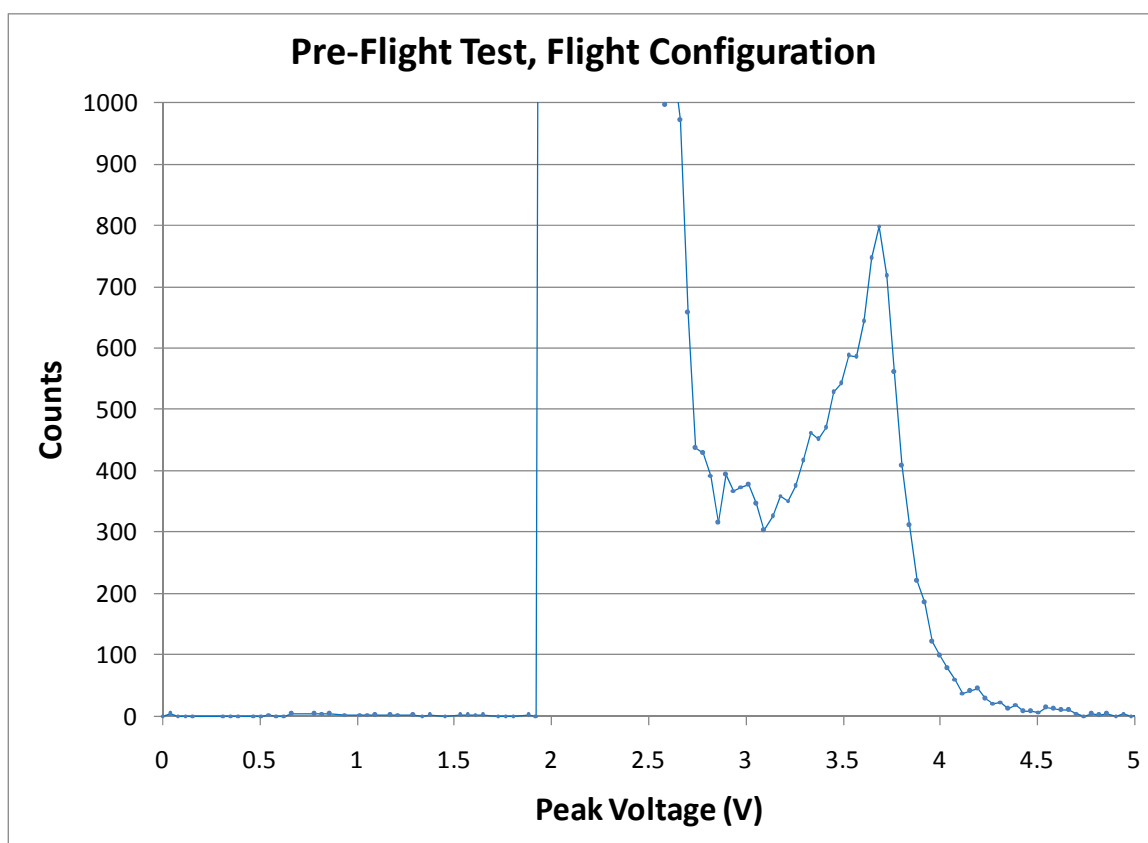
Figure 3.7: HEMI Pathfinder Test in Flight Configuration

The distribution peak is located higher than in previous tests. This may be due to a combination of ambient temperature differences and the different muon energies between this test in New Mexico and all the other tests, which occurred at Penn State.

Continuing with tests performed only with the PMTs, Figure 3.8 is the same test configuration as the single-PMT test shown in Figure 3.5, except the viewing aperture of

the PMT was partially covered. As the output voltage corresponding to muons was in the middle of the instrument's dynamic range, the team was concerned that the more energetic particles would fall outside the range of the PMT (since energy is related to z^2). The goal of obscuring part of the aperture was to reduce the light input into the PMT, thus extending the range of energies that could be detected by the PMT before the output would reach its maximum output. If detected energies were too high, covering part of the crystal would allow detection of higher energies.
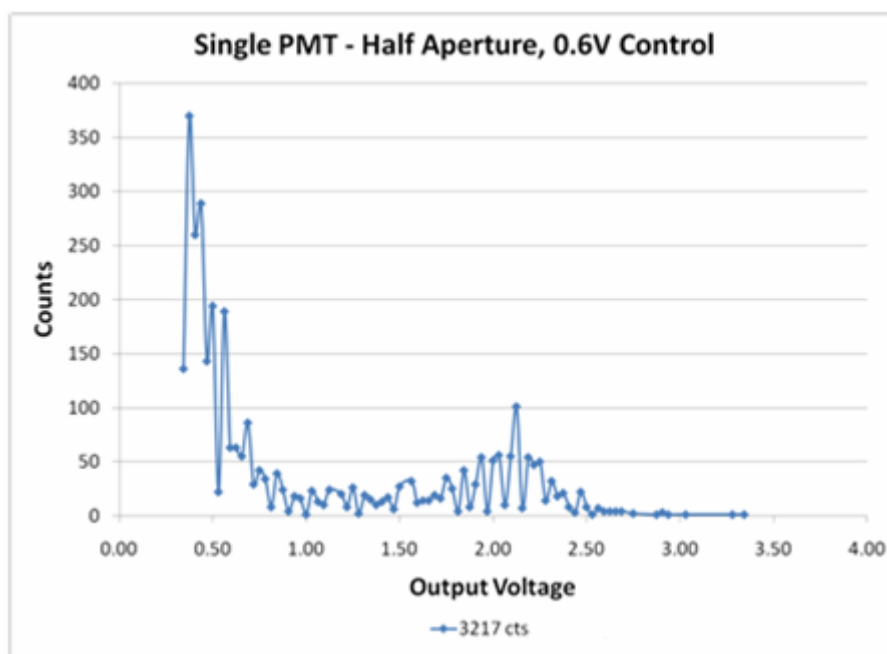

Figure 3.8:   Single PMT, Half Aperture

Notice that the curves in Figure 3.5 and Figure 3.8 are almost identical, except the *x*-axis is shifted slightly to the left since fewer photons entered the PMT. This test was also performed to investigate the possibility of sharing the same crystal opening between two PMTs. This shared configuration was not used for flight because the higher range

was thought not to be needed and instrument volume constraints eventually prohibited the use of two PMTs (see the Section 2.1).

3.4.3 Coincidence (Dual) PMTs

As described above, coincidence detection uses two PMTs to monitor the same crystal. If a pulse is simultaneously generated by each PMT, it is likely due to a particle or photon interacting with the scintillating crystal. If a pulse is generated by only one of the two PMTs, the pulse is likely due to a thermionic emission (dark current). Figure 3.9 shows that in coincidence a significant amount of noise pulses have been removed, and, as a percentage, there are more counts in the muon distribution than the noise distribution.
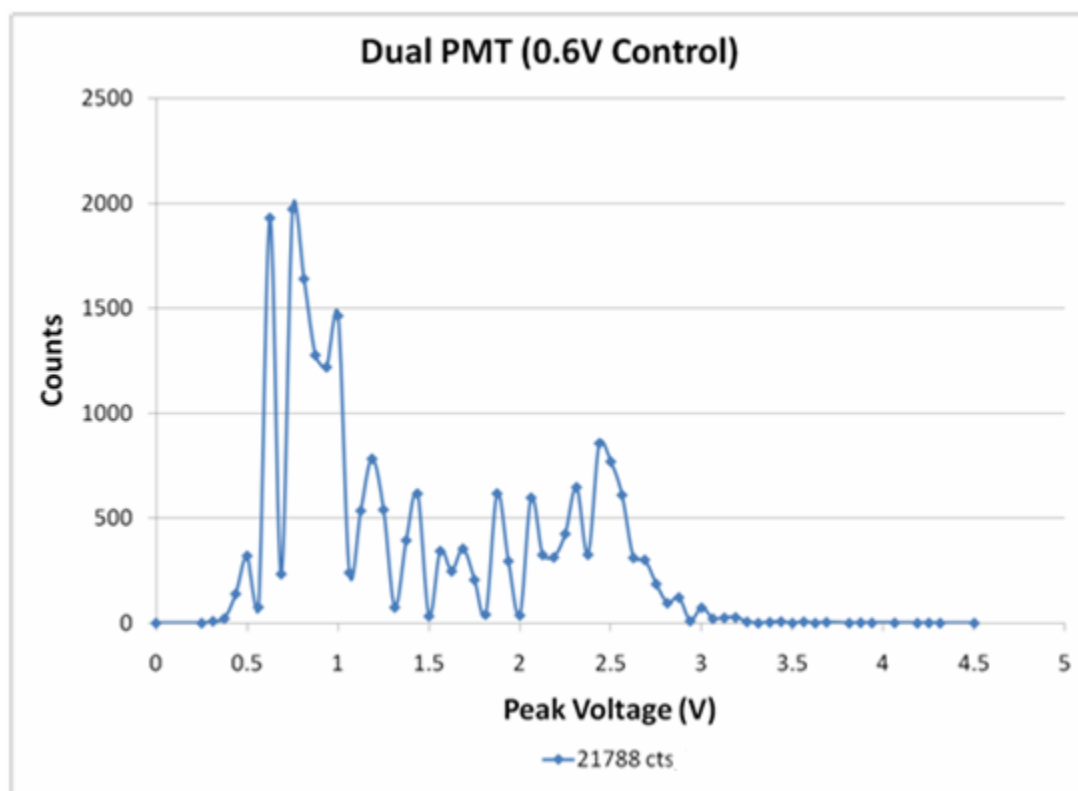
Figure 3.9: PMT Coincidence Measurement

3.4.4 Noise Dependence on Control Voltage

To better understand the effects of control voltage on the output of the PMT, the control was lowered to 0.5 V. Immediately, it was clear that the rate and magnitude of the peaks were much smaller. For this test, the scope trigger threshold was set lower than previous tests just to increase the sensitivity. With the gain so lowered, even in the dual configuration, effectively only the baseline dark current noise was detected, and any meaningful data was obscured by the noise, as shown in Figure 3.10.
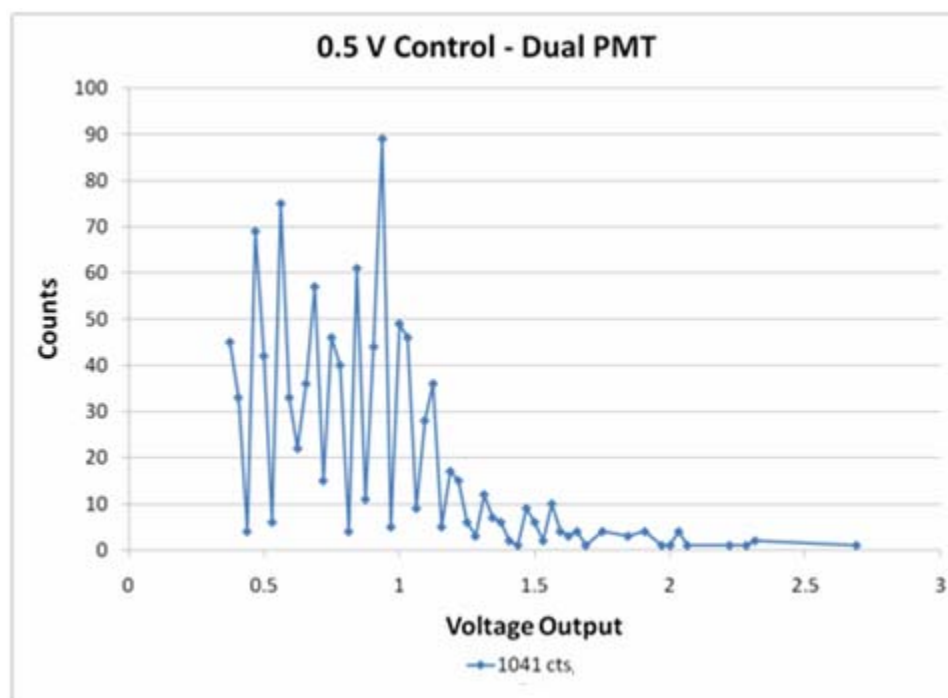
Figure 3.10: Dual PMT Test with 0.5 V Control Voltage

The effect of control voltage was studied in general in order to determine the

optimum setting that would be high enough to provide sufficient gain, yet low enough to

minimize the dark current effects. Figure 3.11 shows how the thermionic noise increases

with increased control voltage. This shows that the optimal place to keep the control

voltage is ~0.7 V as that is the maximum gain that can be achieved before thermionic

emissions start to be more of an issue as a higher gain is then high enough to more

significantly amplify the low-amplitude dark current pulses. However, at 0.7 V, the

increased rate indicated that afterpulses (discussed in Section 2.7) were being detected.

A 0.6-V control voltage provided the theoretically expected rate, so this is the control

voltage that was used for flight. For this specific test, the crystal was removed so that the

only pulses would come from noise sources inside the PMT.
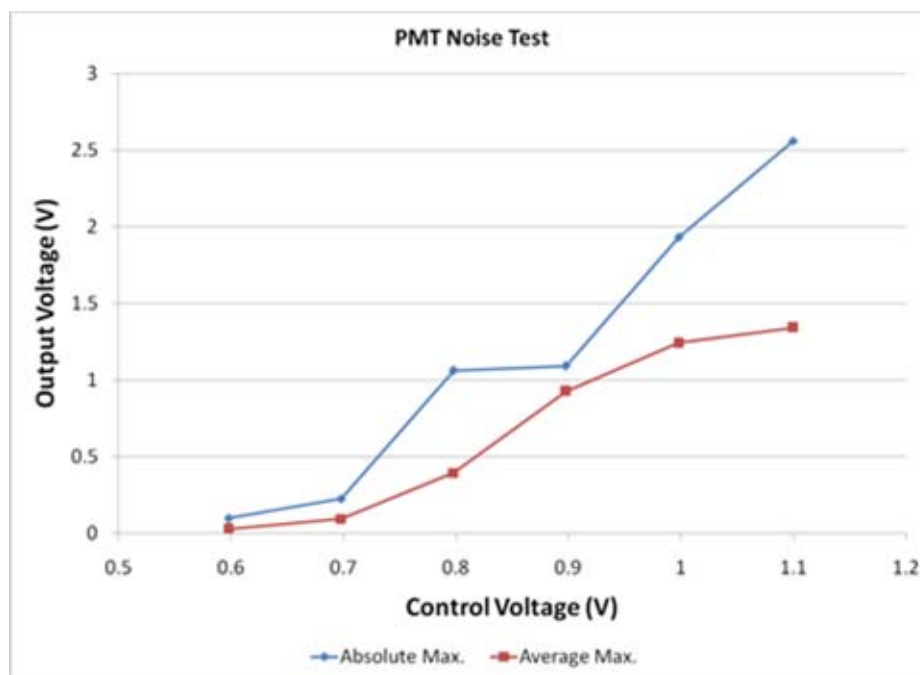
Figure 3.11: PMT Noise Dependence on Control Voltage

3.4.5 Temperature Effects

Understanding how temperature affects the devices was also important.

Figure 3.12 shows the results of four separate tests, each of which were run at single

temperature. The four temperatures used were 10 °C, 23 °C, 31 °C, and 40 °C. The test

setup included the PMT with the crystal. As expected, the test showed that the thermal

noise increased with temperature—most significantly as the temperatures exceeded 30

°C. Since the test was conducted using the slower oscilloscope–MATLAB-GPIB

interface, the spectrum will be slightly biased towards the more frequent pulses. This

explains why the spectrum tends to shift towards the lower energies as the thermal noise

increases.
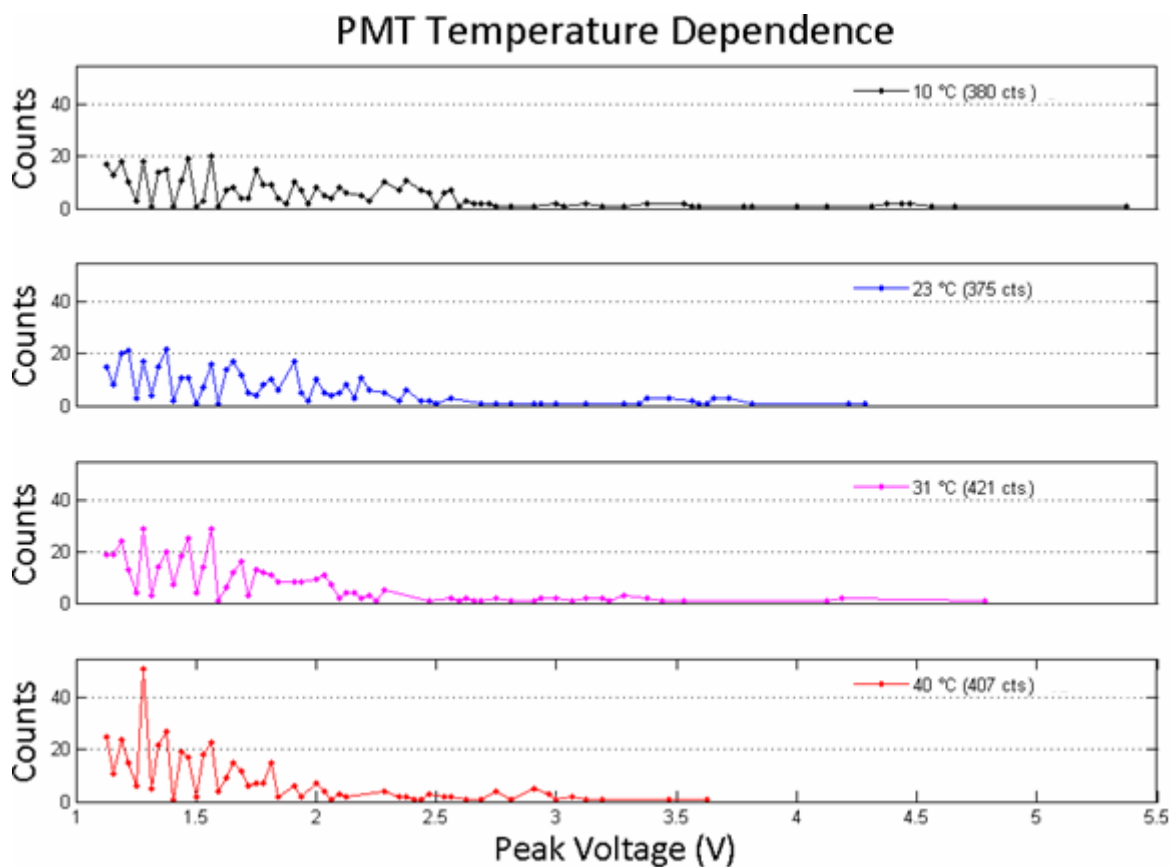
Figure 3.12: Post-Flight Thermal Test Showing Temperature Dependence

3.4.6 Power Variations

Understanding the dynamic power requirements was necessary for appropriately sizing the power supply. Figure 3.13 shows that the PMT negative supply current and control signal supply current do not change appreciably with change in control voltage. Positive supply voltage changes noticeably as the control voltage is increased, but the variation falls well within the planned power supply capability and did not drastically affect the instrument power budget.
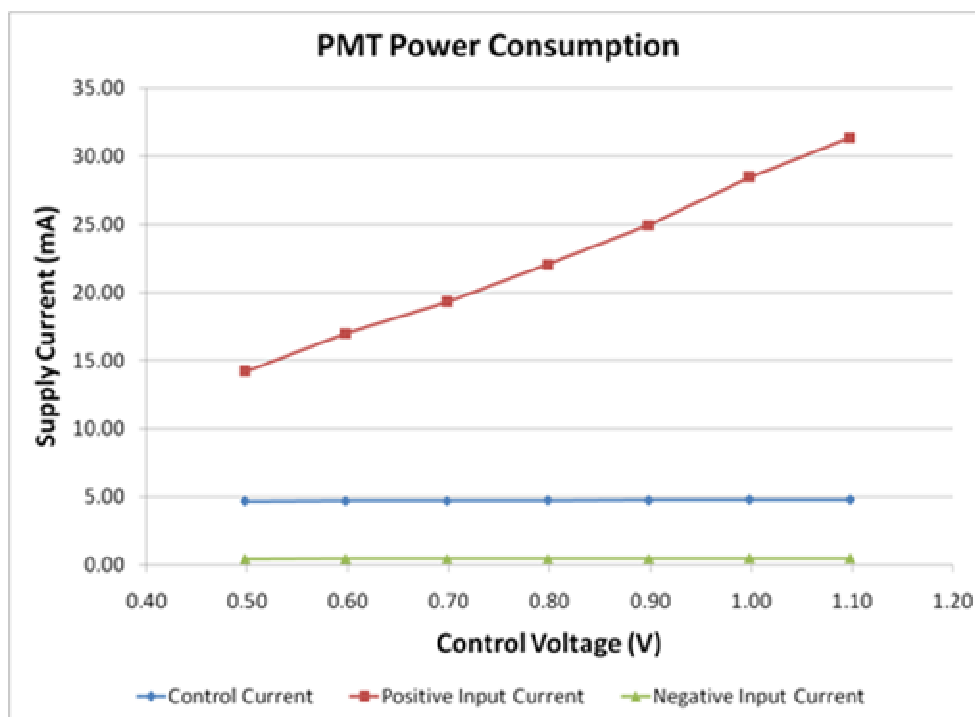
Figure 3.13: Variation of Detector Power Requirements

3.4.7 Pressure Variations

As the pressure would vary between ~760 torr at launch to ~10 torr at float,

understanding the response of the detector with respect to pressure was investigated. The

first pressure test took the PMT down to 1 torr. However, this was the test that proved

that the PMTs would not operate in the desired operational environment and caused the

system to be redesigned. After the pressure vessel design was implemented, it was

desired to understand how the detector would operate over a limited pressure range in the

event that the vessel began to leak slowly. Figure 3.14 shows the detector operated at

ambient pressure compared to the same test operated at 100 torr (well above the dielectric

breakdown). The results show that the PMT is not affected by pressure variation as long

as the pressure is outside the breakdown range.
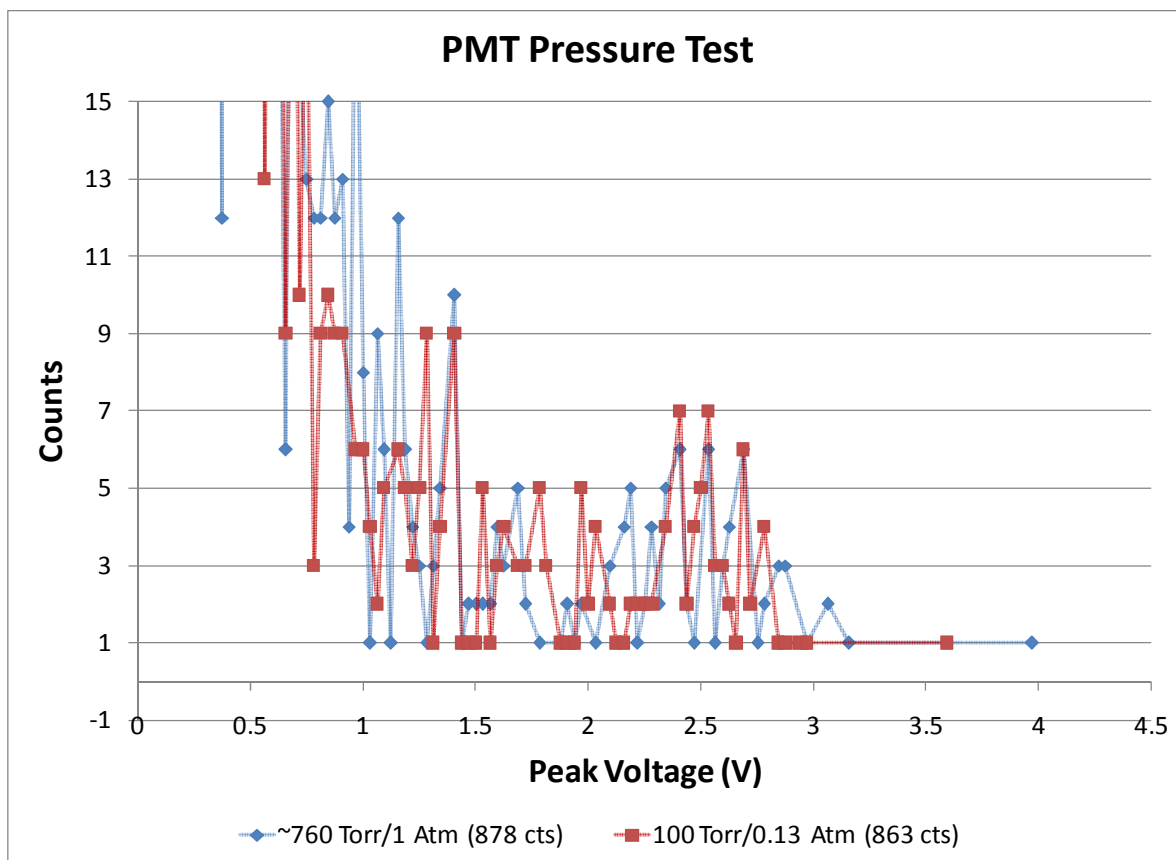
Figure 3.14: Detector Test Showing No Variation with Pressure

3.4.8 Using Radiation Sources

Finally, rather than only relying on ambient radiation, the team acquired radiation

sources to provide known calibration points. Figure 3.15 shows the same general tests

described above (crystal, coincidence PMT configuration) repeated with a sample of

^{137}Cs present. The left image illustrates the results from the typical control experiment

(no radiation source) and it shows the usual ambient muon and thermal noise

distributions. The right image uses ^{137}Cs (primary emission line at 662 keV). Notice that

the rate at which photons from the radiation source are being detected is much faster than

the rate at which muons are being detected. The ^{137}Cs test shows the majority of the

counts from the ^{137}Cs. Recall that there is some delay in the automated sampling set up

time. By the time the program resets and is ready to take measurements again, there is a

much higher probability of detecting a photon from the radiation source than a muon,

because the rate at which the radiation source emits is much higher than the rate at which

muons are detected.
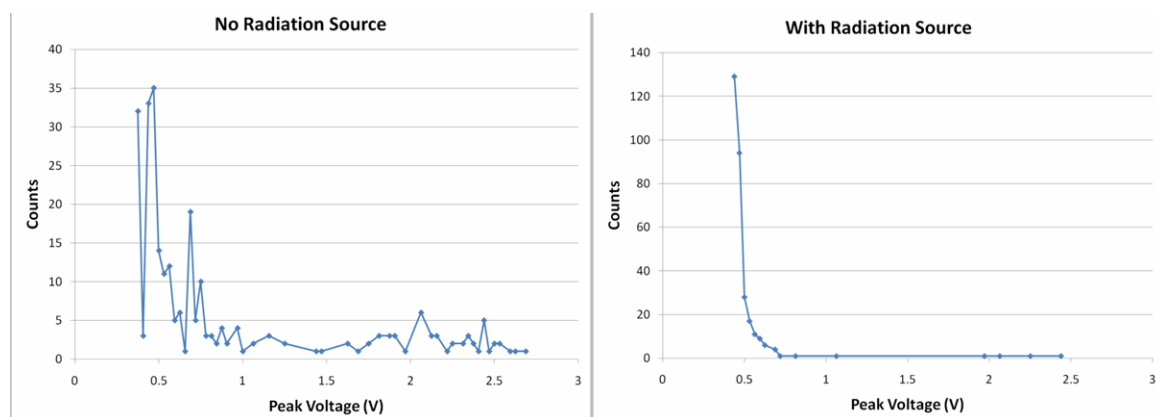
Figure 3.15: Comparison of Muon Tests to ^{137}Cs Tests

Chapter 4

Results

This chapter presents the final results of the mission. This includes the

engineering and science data product, the analyis of the data, and comparison to the

misison's expected results. The final conclusions are presented, in addition to the key

lessons learned during this project, and an outline of the work that should continue into

the future.

4.1 Flight Results

Launch occurred at NASA's Balloon Base in Fort Sumner, NM at 07:33:34 local

time (MST) on 15 September 2008 (13:33:44 UTC). Figure 4.1 illustrates the latitude,

longitude, and altitude collected by onboard GPS. Table 4.1 shows the mission event

timeline for key events during the flight in hours since launch, and both local and UTC

time.
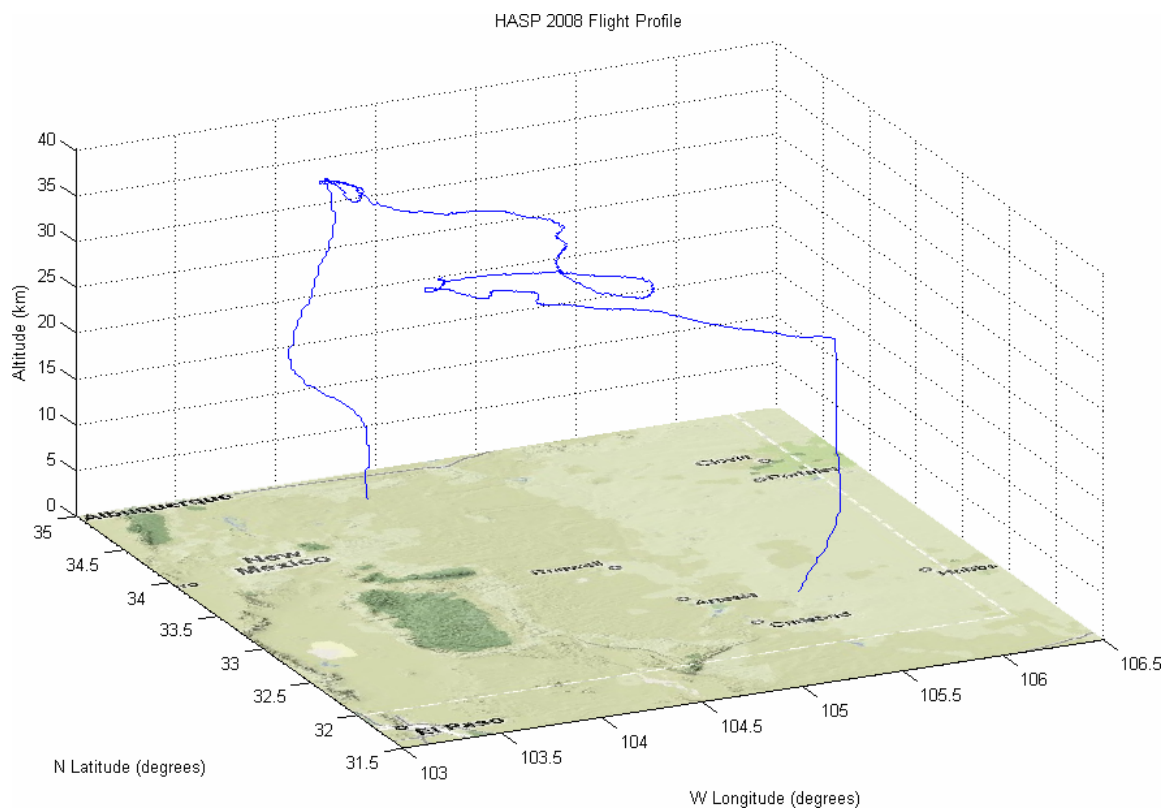
Figure 4.1: HASP Flight Profile

Table 4.1: Mission Event Timeline

Event	MET (Hours)	MET (hh:mm:ss)	Local Time	UTC Time
Launch	0.00	00:00:00	7:33:34	13:33:34
Achive Float Altitude	2.05	02:03:04	9:36:38	15:36:38
Local Noon	4.44	04:26:26	12:00:00	18:00:00
Local Sunset*	11.49	11:29:26	19:03:00	1:03:00
Local Midnight	16.44	16:26:26	0:00:00	6:00:00
Local Sunrise*	23.12	23:07:26	6:41:00	12:41:00
Instrument Power-down for planned termination	23.42	23:25:26	6:59:00	12:59:00
Instrument Power-up after termination cancelled	26.33	26:19:44	9:53:18	15:53:18
Local Noon	28.44	28:26:26	12:00:00	18:00:00
power down for final termination	32.36	32:21:47	15:55:21	21:55:21
Flight Termination	33.83	33:49:49	17:23:23	23:23:33
Local Sunset*	35.47	35:28:26	19:02:00	1:02:00

*Source: http://www.almanac.com/

The ascent lasted approximately two hours. The payload remained at float altitude (120,080 feet, 36.6 km) for 31.8 hours. Figure 4.2 shows the HEMI instrument at float altitude. At local time 17:23:33 on 16 September (23:23:33 UTC), HASP

operators cut down the payload and it descended by parachute. After landing, the

payload was recovered and HEMI was returned to PSU for post-flight calibration.

Figure 4.2: HEMI at Float Altitude

The first termination attempt began the morning of the second day. In

preparation, most payloads including HEMI were turned off at 12:59:00 UTC on 16

September. When no optimal landing sites were available, HASP was allowed to float

longer. Subsequently, some payloads, including HEMI were turned back on at 15:53:18

UTC. The payloads were finally powered off the final time at around 21:55:21 UTC in

preparation for termination.

HEMI was turned on before and through launch and ascent. The instrument

continuously down-linked science and telemetry data throughout this time period.

Various temperatures, recorded by HASP, measured throughout the HASP

payload are shown in the following seven figures. The predicted minimum temperature

of approximately -70 °F (-57 °C) was to occur around 60,000 feet. Ambient

temperatures at float averaged 5 °C to 10 °C during the day and -40 °C at night.

Figures 4.3, 4.4, and 4.5 provide the temperatures for components of the HASP

Flight Control Unit (FCU), Serial Control Unit (SCU), and Data Archive Unit (DAU),

respectively. These three items comprise the HASP command and control subsystem.

The FCU controls subsystem receives, decodes, and distributes up-linked commands

from the Ft. Sumner ground station, monitors the payloads for faults, collects system

environmental data. The SCU provides the serial interface to each student payload and

the DAU controls the on-board recording of all data to an onboard flash drive. [*HASP-*

CFP, 2008]
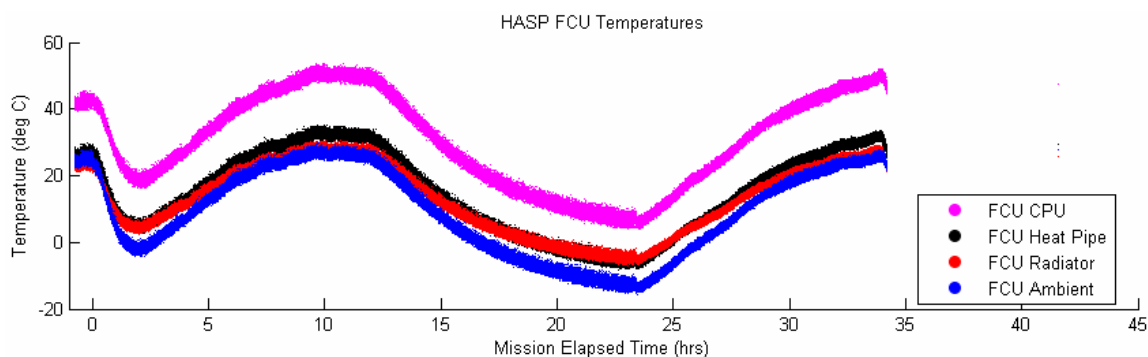
Figure 4.3: HASP Flight Control Unit (FCU) Temperatures
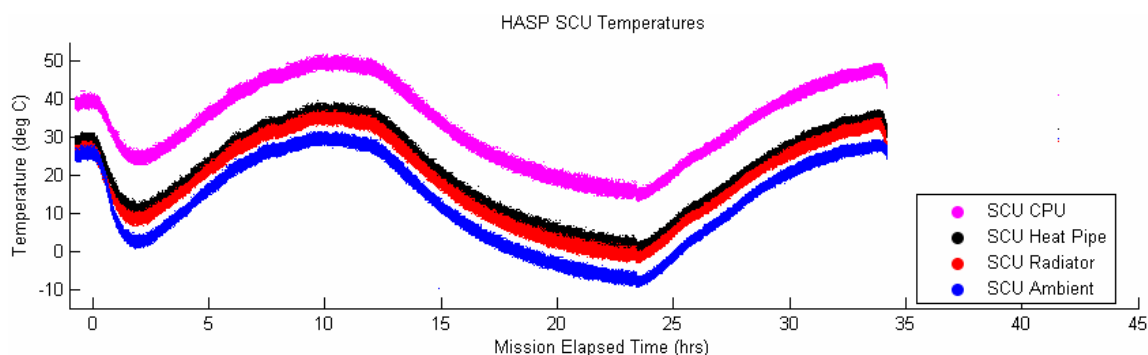
Figure 4.4: HASP Serial Control Unit (SCU) Temperatures
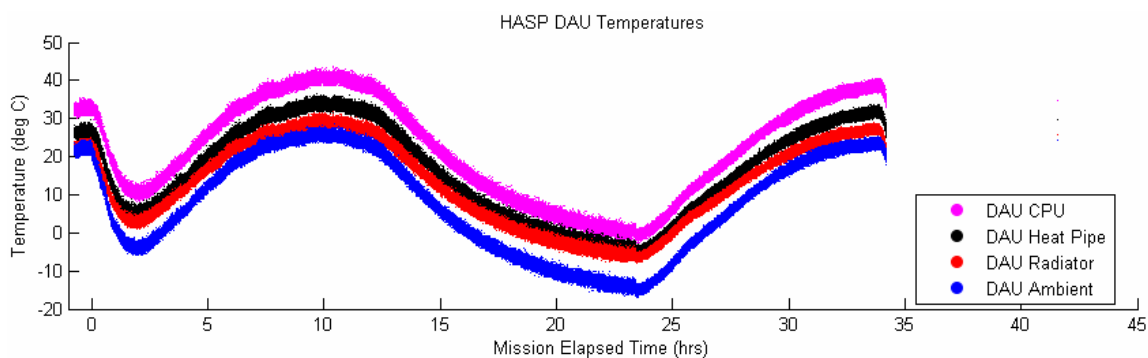
Figure 4.5: HASP Data Archive Unit (DAU) Temperatures

All these HASP Command and Control components are mounted inside solar shields to maintain electronics and battery temperatures and to isolate the HASP system from the student payloads. Temperatures of the solar shields are shown in Figure 4.6.
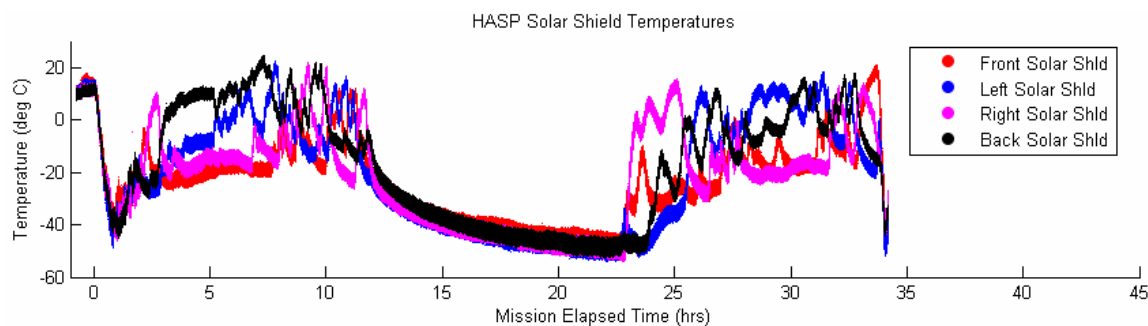
Figure 4.6: HASP Solar Shield Temperatures

HASP used eight lithium battery packs (11-cell). These temperatures are shown in Figure 4.7.
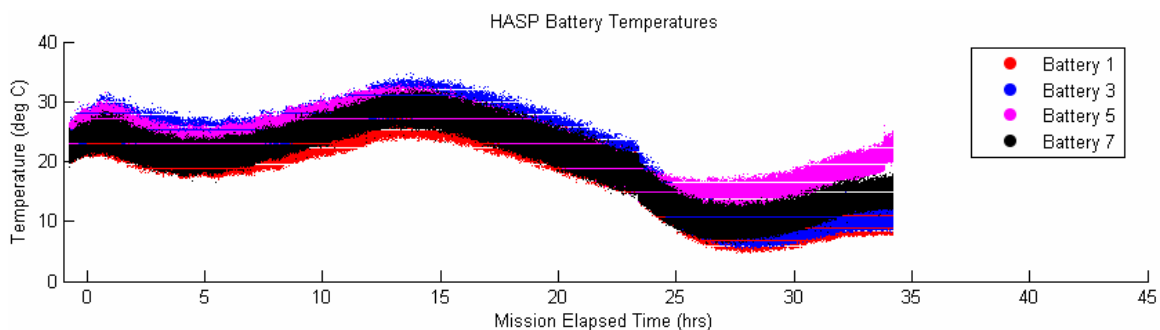
Figure 4.7: Battery Temperatures

Figure 4.8 shows the temperatures of the top of the payload plate for two student payloads. Student Payload 12, or SP12 is one of the large payloads—the Microwave Reception Experiment—which characterized the spectrum between 45-75 GHz.. Student Payload 8 was not flown, and the temperature is of the mounting plate mounted away from HASP on a boom similar to the HEMI pathfinder. Note that the position of the payloads can affect a 20–30 °C difference in ambient temperature. Recall that the HEMI instrument was a small payload on one of the outrigger booms.
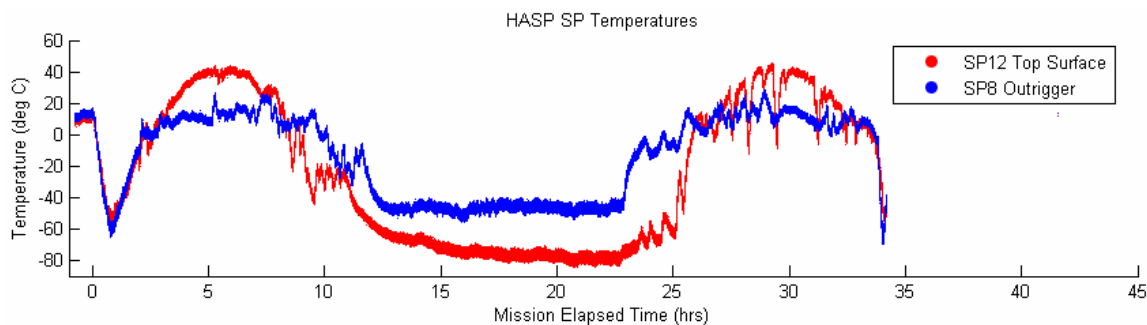
Figure 4.8: HASP Surface Temperatures

Figure 4.9 shows the data from the thermistor sensor placed on the PMT and monitored through the HASP analog channels. Comparing this to Figure 4.8 above shows that, despite previous (incorrect) calculations that the Earth's albedo and heat from

the electronics would sufficiently warm the instrument, the internal temperature of HEMI in fact closely tracked the ambient environment temperature. Recall that the local sunset and sunrise times were at 11.5 and 23.1 elapsed hours, respectively. As the instrument electronics produced a constant amount of power, the only thermal variations were due to diurnal environmental variations. The only beneficial deviation from the ambient temperatures was that the PMT temperature only dropped to -30 °C as the balloon passed through the tropopause at roughly one hour into the flight, compared to the -60 °C ambient temperature. Of course this is still well below the $+5$ °C minimum operating limit of the PMT.
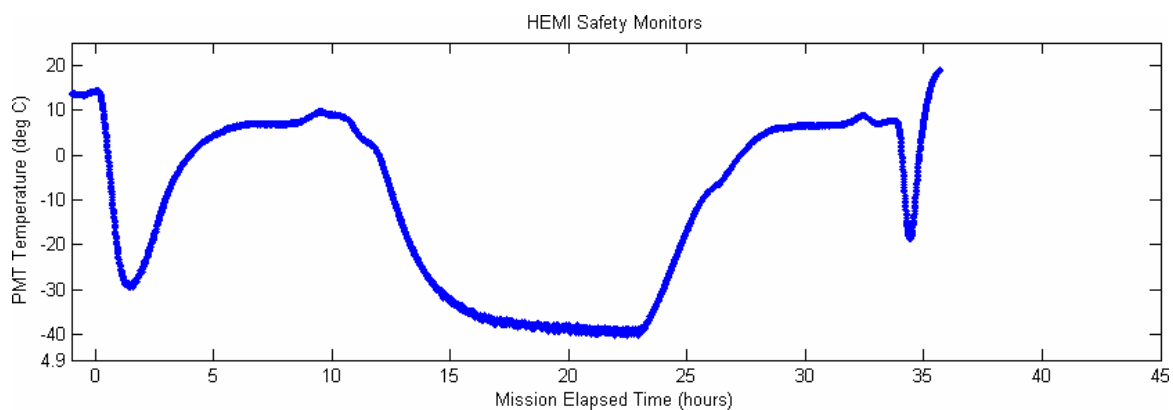
Figure 4.9: HEMI Safety Temperature Sensor

4.2 Science Results

The data product of the HEMI pathfinder was a recording of every peak voltage detected by the instrument throughout the mission. The data were stored on the ground in time-stamped data files, each containing 25,000 peak values. The majority of the peak

values were noise around the threshold value, so the effective rate is 25,000 peaks about every 20 minutes or one time-stamped file every 20 minutes.

As soon as a new data file was available, a MATLAB script parsed the binary file and generated an energy spectrum showing the total number of counts (i.e., number of times a peak voltage occurred) during that time period versus the range of peak voltages. Figure 4.10 shows three representative spectra taken during different times of the flight (indicated in the legends of each picture). The figures are marked with the local time (MST) as the local environment had an effect on the data, as will be described shortly. In Table 4.2, one will notice that the shapes of the curves are similar to the graphs presented earlier in the Instrument Testing and Calibration section. The tail end of the peak around 2 V is the noise present in the system. The C&DH peak detection algorithm included a software threshold to ignore peaks below 2 V. The large, distinct peak is due to muons. However, one will also notice that the bottom two pictures deviate from the earlier calibration results in that multiple peaks and more distributed peaks are now visible.
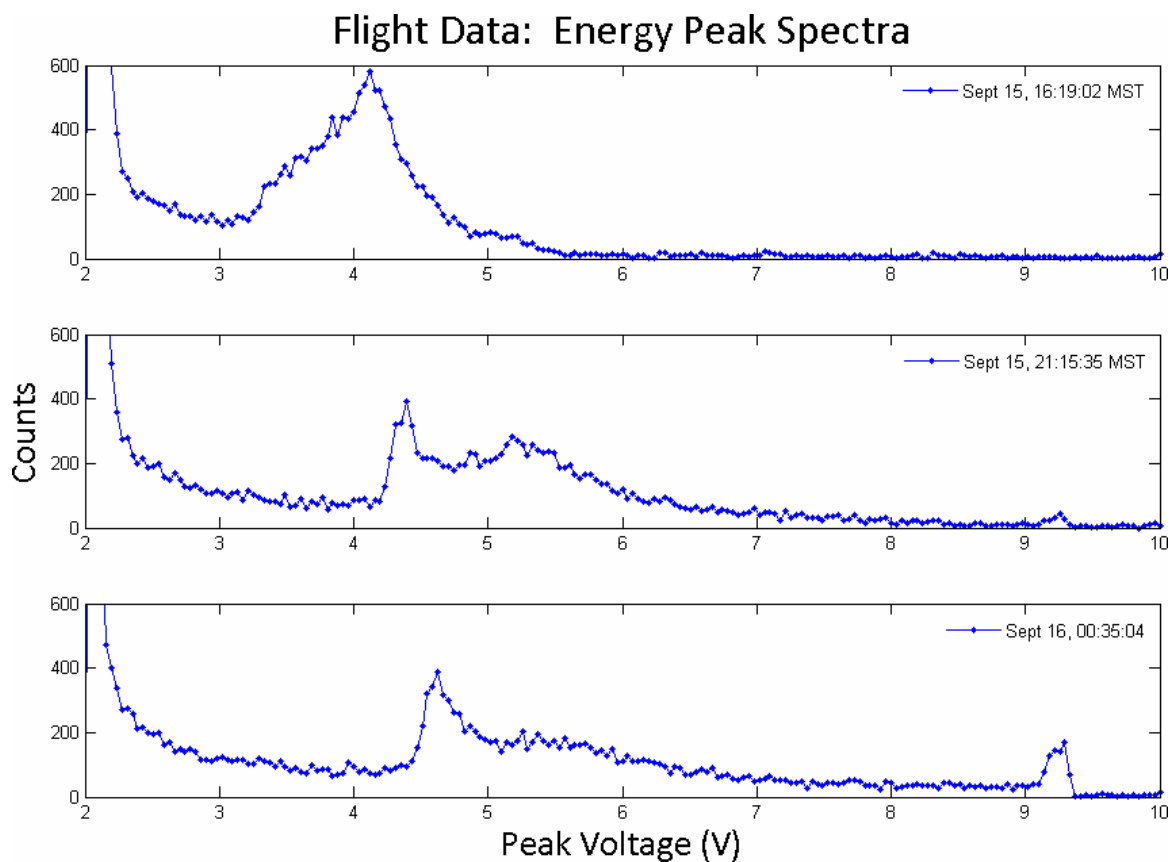
Figure 4.10: Select Energy Spectra Plots From Flight

Table 4.2: Spectra Time Stamps

Universal Coordinated Time (UTC)	Mission Elapsed Time (MET)	Local (MST)
Sept 15, 22:19:02	08:45:28	Sept 15, 16:19:02
Sept 16, 03:15:35	13:42:01	Sept 15, 21:15:35
Sept 16, 06:35:04	17:01:30	Sept 16, 00:35:04

Figure 4.11 shows how the energy spectra vary over the course of the flight. The *x*-axis is the mission elapsed time (MET) while the *y*-axis indicates the voltage of the peak(s) detected during each time interval. The color of the data point is indicative of

how many times (counts) the peak voltage occurred during that time interval to indicate
the relative size of each peak.
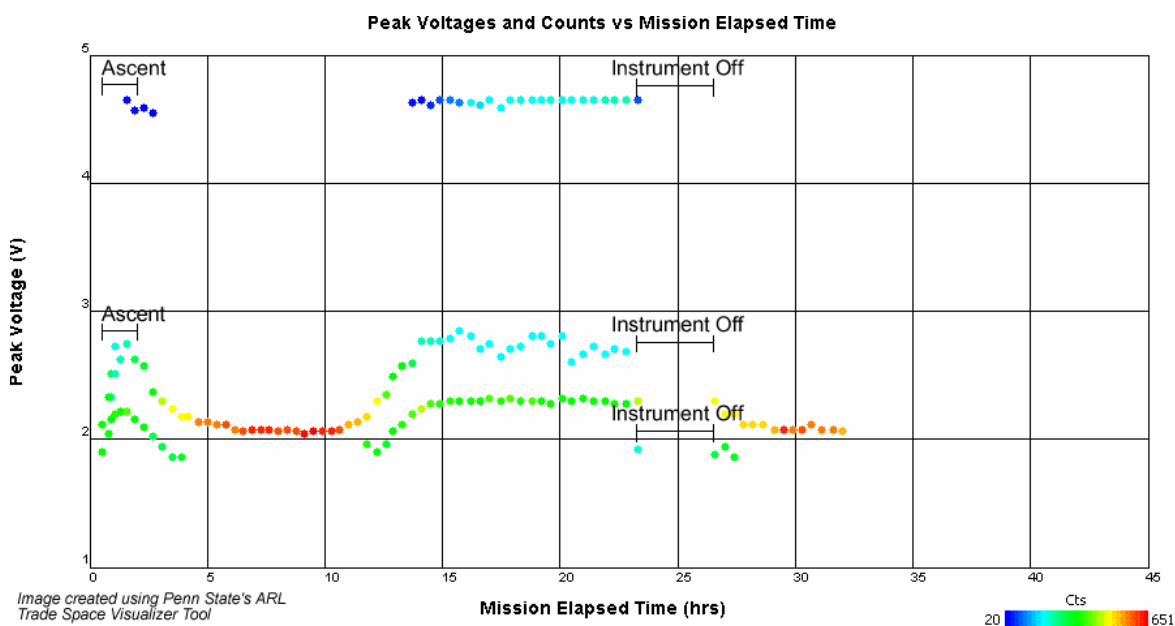
Figure 4.11: Peak Voltages and Counts vs. Mission Elapsed Time

By examining Figure 4.11, it is clear that there is a distinct diurnal variation in the
data and that the rate and energy of the particle flux may vary with the Earth's rotation.
However, the peaks did not agree with the expected z^2 energy relationship. Furthermore,
the fact that the minimum temperatures far exceeded the operating and storage
temperature of the PMT made the data suspect. Also, the NaI crystal is temperature
sensitive, which could easily affect the data.

A post-flight calibration was carried out to verify that the temperature hypothesis
was correct. The full instrument was assembled and placed in the SSPL thermal-cycling
chamber to simulate representative temperatures recorded during flight. Figure 4.12

shows the power consumption of the instrument and, most importantly, the temperature

as it was measured by a thermistor mounted to the PMT.
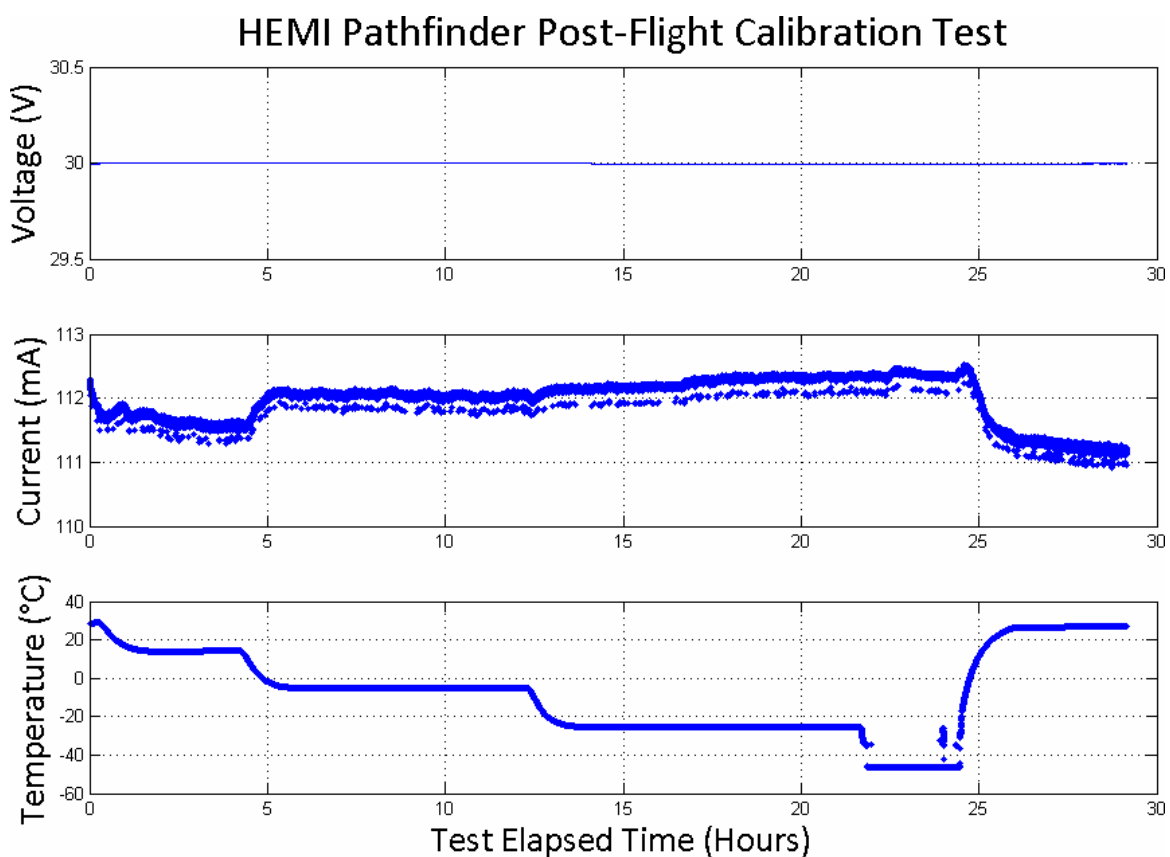
Figure 4.12: Post-Flight Calibration Environment

The instrument was left to operate at ambient room temperature for just under 12

hours. Afterwards the chamber was set to 14 °C, −5 °, and −30 °C as shown in Figure

4.12 above. The final drop between about 22 and 24 hours is explained by the AA

batteries internal to the vessel powering the thermistor sensor getting too cold. The

temperature chamber was maintained at −30 °C throughout this time. However, this was

not noticed during flight.

114

The detector peak voltages during each of these periods are shown in Figure 4.13. One will quickly notice a drastic variation of peak values with the change in temperate. Also the constant ambient temperature periods before and after the test agreed nicely. This shows that the detector and electronics are not permanently damaged by exceeding temperature extremes but certainly vary with temperature. During temperature transitions, the distribution of peak voltages is significantly spread out as the temperatures vary. The soak periods, where the temperature is held constant, shows more distinct peaks. Finally, looking at the −30 °C soak, one will recognize the typical primary peak at 2.25 V and a more subtle secondary peak at 2.75 V. This agrees nicely with the values experienced during flight. The magnitude (number of counts) of the peaks is related to the time of each test period, with longer periods having more total counts. Therefore, the graphs below illustrate the relative trends of the peak as temperature changes.
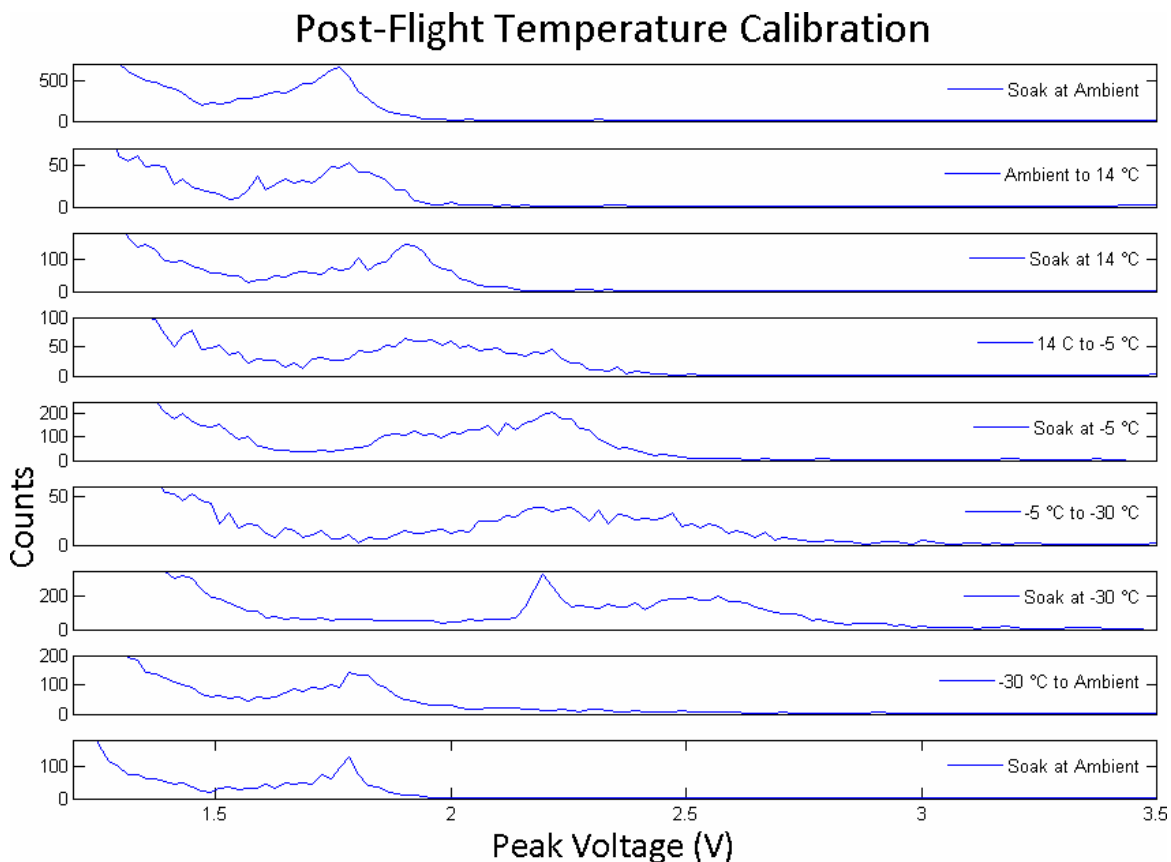
Figure 4.13: Varying Peak Voltages With Temperature

The only feature in the flight data that does not appear in the post-flight calibration data is the high energy peaks near the upper limit of the instrument output. If the muon peak voltage is centered at 2.25 V (at the extreme cold temperatures), then by the z^2 relationship, the expected peak for a $z = 2$ particle would be around 9 V. It is very likely that the upper peaks measured during flight were from particles from $z > 1$, but that the detector output just saturated. The more energetic particles do not penetrate to the ground altitudes.

It is clear now that the sensitivity of the detector and the selected gain provided so much amplification that only particles with $z = 1$ could be resolved. Any higher energy particles were collected in the single peak towards the end of the detector's range. Without access to energetic test sources with $z > 1$ for ground testing, it is impossible to verify this assumption. However, it is valid to conclude that in the flight configuration, only particles with $z = 1$ could be detected. Finally, if the originally planned uplink commands were implemented (as described in the C&DH implementation section), at least the detector gain could have been lowered in near real time during flight, which may have given the detector enough dynamic range to detect the higher energy particles.

Chapter 5

Project Summary

5.1 Conclusions

This effort was to educate and train a team of inexperienced students through the approximately 10-month development of a pathfinder energy detection instrument that would provide the foundation for the more complex and rigorous iterations to follow— eventually culminating as a flight instrument on the proposed JANUS mission.

The analysis of the flight data showed that thermal environment for high altitude balloons was not well understood for this mission and, as a result, the temperature of the electronics exceeded their operating ranges and the data during those extremes is unreliable. Furthermore, the inability to calibrate the detector with energetic sources expected during flight (~GeV) hindered the team's ability to understand the sensitivity and range of the detector output. As a result, only the lower-energy (low-z) muons were detected, as higher energy particles were outside the range of the detector in the flight configuration.

Despite these setbacks, the detector reliably detected muons during the nominal operating periods, which occurred during the local daytime when temperatures were within the operating range of the electronics. Furthermore, while not understood pre-flight, the anomalies experienced during flight were sufficiently understood and explained through extensive post-flight testing in thermal chambers. Also, future

iterations will be focused on lower energy gamma rays, for which the project has already acquired test radiation sources.

Therefore, from the science and engineering standpoint, the mission's minimum success criterion to detect and measure energetic particles during the flight was met. Comprehensive success would have been realized except for the schedule-driven de-scope actions that took place in the months prior to launch. These de-scopes allowed the minimum science objectives to be accomplished, but to do so, sacrificed the demonstration of up-link commands; remote operation and control of the instrument parameters (PMT gain, threshold level); and extensive system monitoring (although minimum monitoring was accomplished through the safety pressure and temperature sensors). It should be noted that the original designs allowed for such de-scopes in a methodical manner, in expectation that the short development schedule may require a limited focus.

On the programmatic side, it is the conclusion of the author that this project was an overwhelming success. It demonstrated an effective training and recruitment model that was able to train a young group of students in a matter of months and provide a strong personnel foundation for the next HEMI iteration on the long duration balloon. Despite being on a very constrictive schedule throughout most of the project, and especially towards the end, the project was able to generate comprehensive documentation on the prototypes, flight designs, testing, and integration—totaling 85 archived documents subject to unique document numbers and version control managed through SSPL's document library system. This total number does not include

documentation of the post-flight analysis tools and results, which will be forthcoming upon completion of this thesis.

Prior to flight, a wealth of science and engineering test data unprecedented for a Penn State student project were gathered through extensive thermal and vacuum testing of components. The early testing provided a thorough understanding of most of the payload systems; although it was unable to uncover the thermal environment issues or the excessive sensitivity of the PMT mentioned above. In hindsight, inclusion of detailed reviews with invited professors and industry representatives with expertise in the area would likely have helped correct some of the incorrect assumptions and understandings going into the flight. However, because of the wealth of pre-flight test data, the post-flight anomalies were able to be better understood by the team.

A wealth of knowledge and experience was generated during this project. The low student attrition rate in the near future will ensure that these lessons will not be forgotten, and this thesis will provide a foundation for the continuing HEMI efforts. The lessons learned and heritage developed during this brief effort already serve as the foundation for the continuing HEMI project—now totaling 28 students and continuing to grow.

5.2 Lessons Learned

The purpose of this project was to lay the foundation for the eventual student development and operation of the High Energy Monitoring Instrument on the JANUS spacecraft. As such, this section describes lessons learned that were contributed by the

students as a reference to future generations of students working on HEMI. While some of these may be common sense to experienced engineers, these lessons are often new to students and sometimes learned a high cost. Ideally, and in future projects, these lessons should be learned through reviews staffed by experience students, professors, and industry representatives. This could significantly benefit the students and the success of the project. This process was adopted for the follow-up long-duration balloon mission.

Thermal Control and Compensation — Temperatures can have drastic effects on electronics. A **validated** thermal model should be developed to ensure electronics stay within a tolerable range. If necessary, thermal control systems should be included. Even within acceptable operating conditions, thermal affects will change the performance of the electronics, so the design should include temperature-compensated circuitry, and an understanding of how the electronics perform across the full temperature range, including calibration curves.

Hardware selection — If possible, it is preferable to select hardware or instrumentation that has an established heritage for your application. Even if a tried and true part may not have all the best performance parameters compared to cutting edge parts, the reliability of older parts can be more critical to the mission.

Separate hardware and software responsibilities — Having separate hardware and software positions allows working in parallel. Also, having a specialist in hardware and a specialist in software is better than one person who is usually very good at one and has a passing knowledge of the other.

Check integrated circuit logic voltage interface levels — It is believed that the reason the FPGA continued to permanently malfunction and short circuit was that the

levels coming from the ADC where 5 V going into a 3.3-V FPGA without any 5-V-to-3.3-V interface translation. Technically, according to the respective data sheets, this interface was sufficient. After further investigation, the most likely reason is that leakage current from the 5-V MUX flowed into the 3.3-V FPGA—even though the MUX was input only—destroying the FPGA.

Save pin assignments to programmable logic parts — Save a copy of the pin outs so they can be used to debug potential shorts out of the FPGA. This can greatly simplify debugging problems that come up during programming.

Use hardware travelers — Have separate ESD boxes for each board and record everything done to that board (calibration, drops, cut traces, jumpers, etc.) on documents that are maintained with the board itself.

When problems occur, bring solutions to the table, not just the problem — When you find a problem—and you will find problems—think it through and be able to provide a list of options/solutions to your project manager or cognizant lead.

Verify that you and the supplier have a complete mutual understanding before purchase, preferably in writing — The cylindrical NaI crystal was thought to be bare but was in fact enclosed in aluminum on all sides except one of the faces. This completely excluded the original plan to operating two PMTs in coincidence. Cost and time pressures precluded ordering a new crystal. The possibility of overlapping two PMTs across the exposed crystal face was explored and even validated in testing. However, volume constraints in the added requirement for a pressure vessel eventually precluded two PMTs anyways.

Also, the PMTs where thought to be sufficiently potted for use in a rough vacuum in which HASP was to fly. This was confirmed over the phone with engineers from Hamamatsu before we purchased them. Once they arrived, our own vacuum testing proved that the PMTs suffered from internal arcing and could not operate in the rough (~1–10 torr) vacuum of the balloon environment. After several phone conversations and irrefutable evidence, Hamamatsu conceded that the "accessories" inside the potted assembly were not rated for this environment. "Accessories" included the high voltage DC/DC converter and the voltage dividers.

Later conversations with Hamamatsu and advice from PSU's physics department concluded that the only PMTs that would be certified for high altitude balloons "out of the box" would be very costly, and likely have to ordered in large quantities (~1000).

Instrumentation amplifiers have very narrow common mode voltages — The power system current sensors used instrumentation amplifiers to sense the small voltage drop across a precision current sense resistor. The specific instrumentation amp selected has a very small common-mode input range typically within $|V_{CM}| < 3.5$ V. This was not discovered until final system testing. In addition to the precious time lost debugging the circuits, the error also removed current-monitoring capabilities for the power system as there was not sufficient time or resources for a redesign.

Incrementally build and test during assembly — Debugging electrical errors, such as short circuits, is challenging when the entire circuit is populated. Populating a board in smaller groups makes for isolating errors easier. It also gives the design engineers an understanding of how the hardware really operates. Note that this may require software

modifications when debugging embedded systems (i.e., FPGAs, CPLDs, or microcontrollers).

Parts should be ordered by those who created the designs — Parts are best ordered by those who created the designs. This can prevent ordering the incorrect parts. Most common mistake is incorrect footprint, or the wrong part in a component family. In the event careful inventories are not maintained, this practice can also prevent over-ordering or under-ordering of components.

Test early, and test often — When something comes in, testing it early allows time for correcting unexpected problems. This was shown when the PMTs where tested at low pressure and did not work properly. Fortunately, the problem was found early; it would have been an issue if structures had not had an opportunity to redesign and build a sealed container to remedy the situation.

Document everything, especially automated/logged data — The beauty of automation is that it logs all the data automatically and easily. The downside is that weeks, or even days later, it is often hard to remember the exact conditions of each test. Incorporating a user prompt in the code to completely describe the test setup for each test will save significant backtracking and retracing later. The other option is meticulous hand-written documentation; however, having the comments follow the test data in the same file can help keep things organized.

5.3 Future Work

A complete understanding of the incorrect pre-flight assumptions has to be investigated and documented. This final analysis will provide insight into the errors to be avoided in future efforts, specifically the thermal environment. The technical implementation errors are better understood at this point. That is, that thermal design needs to be revisited and better command and control of the instrument should be enabled. In hindsight it is reassuring that the original designs planned for all of this and it is regrettable that the resources available to the project were not sufficient to realize the full design within the schedule of the project. Also, the HASP designs, environment, and flight data will serve as a realistic example to validate the thermal model currently in development for the planned long duration balloon.

The intricacies of science and detector operations still leave room for improvement. The ground-tested PMT coincidence implementations were not as effective as was originally hoped or expected. The post-flight analysis forced many of the original understandings of the detector to be revisited. Completely relating the flight data to the scientific processes the data observed still needs to be done.

Bibliography

Band *et al.*, "BATSE Observations of Gamma-Ray Burst Spectra. I. Spectral Diversity,"
The Astrophysical Journal, vol. 413, pp. 281–292, August 1993.

BATSE, (2005). The Burst And Transient Source Experiment. Web site:
http://heasarc.gsfc.nasa.gov/docs/cgro/batse/

Butler, N.R., *et al*. "A Complete Catalog of Swift Gamma-Ray Burst Spectra and
Durations: Demise of a Physical Origin for Pre-Swift High-Energy Correlations.,"
The Astrophysical Journal, vol. 671, pp. 656–677, December 2007.

CoBabe-Ammann, E., & Klumpar, D. (2008). *Final Report of the NASA Program
Definition Team for Student Collaborations*. NASA.

Cusumano, G. *et al*. "Swift Observations of GRB050904: the Most Distant Cosmic
Explosion Ever Observed," *Astronomy and Astrophysics*, vol. 462, pp. 73–80,
February 2007

Feroci, M., Frontera, F., *et al*. "In-Flight Performances of the BeppoSAX Gamma-Ray
Burst Monitor" *Proceedings of SPIE,* vol. 3114, pp. 186, August 1997.

Fox, D. B. *et al*. "The Afterglow of GRB 050709 and the Nature of the Short-Hard
Gamma Ray Bursts," *Nature*, vol. 437, pp. 845–850, 2005.

Frail, D. A. *et al*. "An Energetic Afterglow from a Distant Stellar Explosion," *The
Astrophysical Journal Letters*, vol. 646, pp. L99–L201, August 2006.

Gehrels, Neil (1998). Swift*: A Panchromatic Gamma Ray Burst MIDEX Mission*.
Greenbelt, MD: NASA GSFC.

Gou, L. J., Fox, D. B., and Mészáros, P. "Modeling GRB 050904: Autopsy of a Massive
Stellar Explosion at z = 6.29." *The Astrophysical Journal*, 668 (2007): pp. 1083.

HASP-CFP, (2008). *HASP Call for Proposals*. Baton Rouge, LA: Department of Physics
& Astronomy, Louisiana State University.

HASP-SPIM, (2008). *HASP Student Payload Interface Manual*. Baton Rouge, LA:
Department of Physics & Astronomy, Louisiana State University.

Knoll, Glenn F. *Radiation Detection and Measurement*. New York: John Wiley &
Sons, Inc., 2000.

Liang, E. & Zhang, B. "Calibration of gamma-ray burst luminosity indicators," *Monthly Notices of the Royal Astronomical Society: Letters*, vol. 369, pp. L37–L41 2006, MNRAS, 269, L37

Murata, (2008). WP06R Datasheet. Retrieved November 27, 2008, from Murata Power Solutions, Web site: http://www.murata-ps.com/data/power/ncl/tdc_wp06r.pdf

National Semiconductor, (1995). PC16550D Universal Asynchronous Receiver/Transmitter with FIFOs. Retrieved November 26, 2008, Web site: http://www.national.com/ds/PC/PC16550D.pdf

"Paschen Curve." Teledyne Reynolds, Inc. 8 Oct 2008 <http://www.teledynereynolds.com/product/2multipin/page17.asp>.

Roming, Peter, et al. *Joint Astrophysics Nascent Universe Satellite: Observing the Illumination of the Universe*. Proposal to NASA SMEX AO. 2008.

Saint Gobain, (2008). Efficiency Calculations for Selected Scintillators.

Schratz, B. (2006). *Design of a Sounding Rocket Plasma Frequency Probe*. University Park, PA: The Pennsylvania State University.

Schratz, B. (2007). *High Energy Monitoring Instrument (HEMI)*. Proposal to NASA High Altitude Student Platform, 2008 Flight Opportunity.

Appendix A

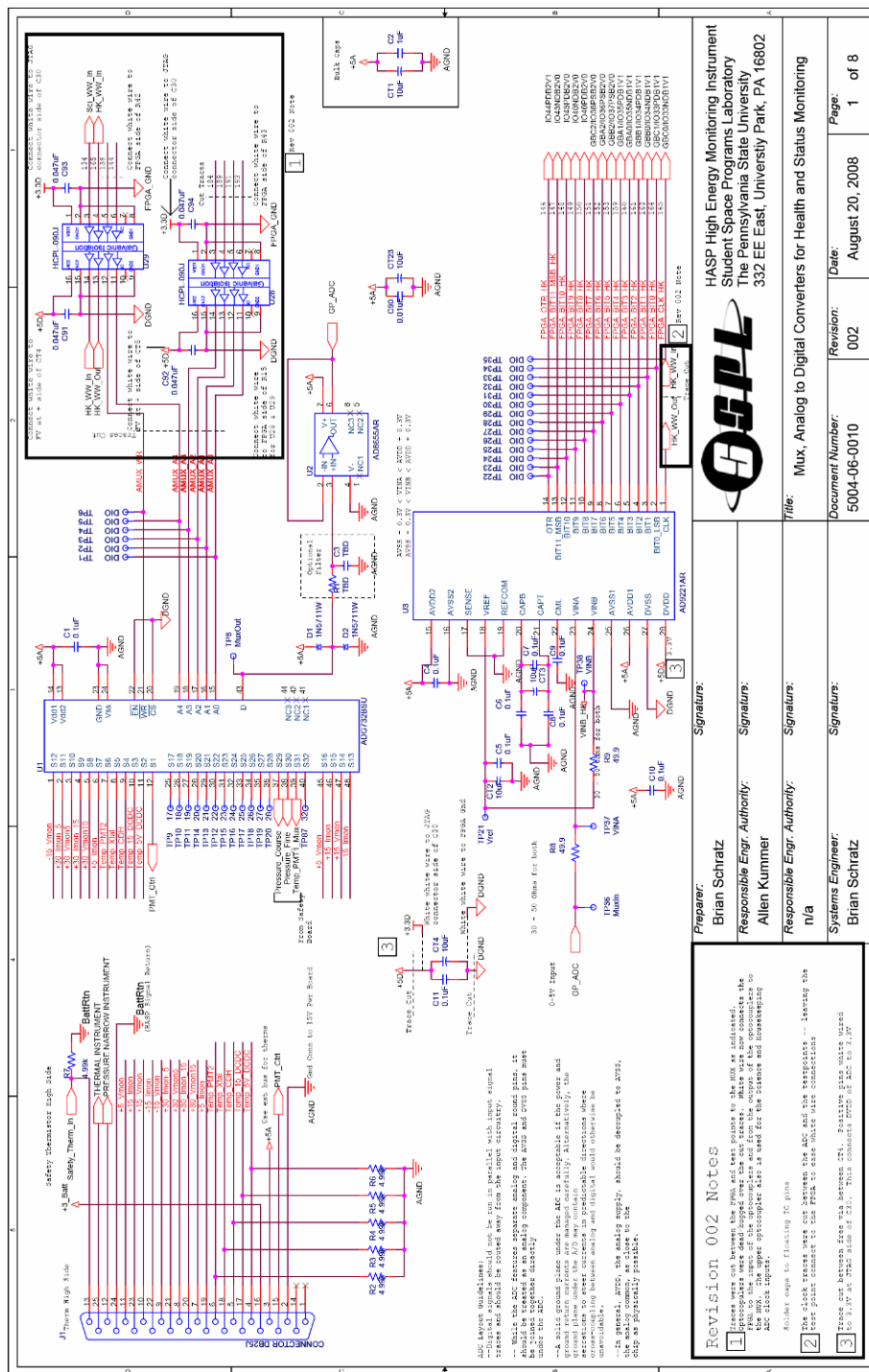**Command and Data Handling Schematics**

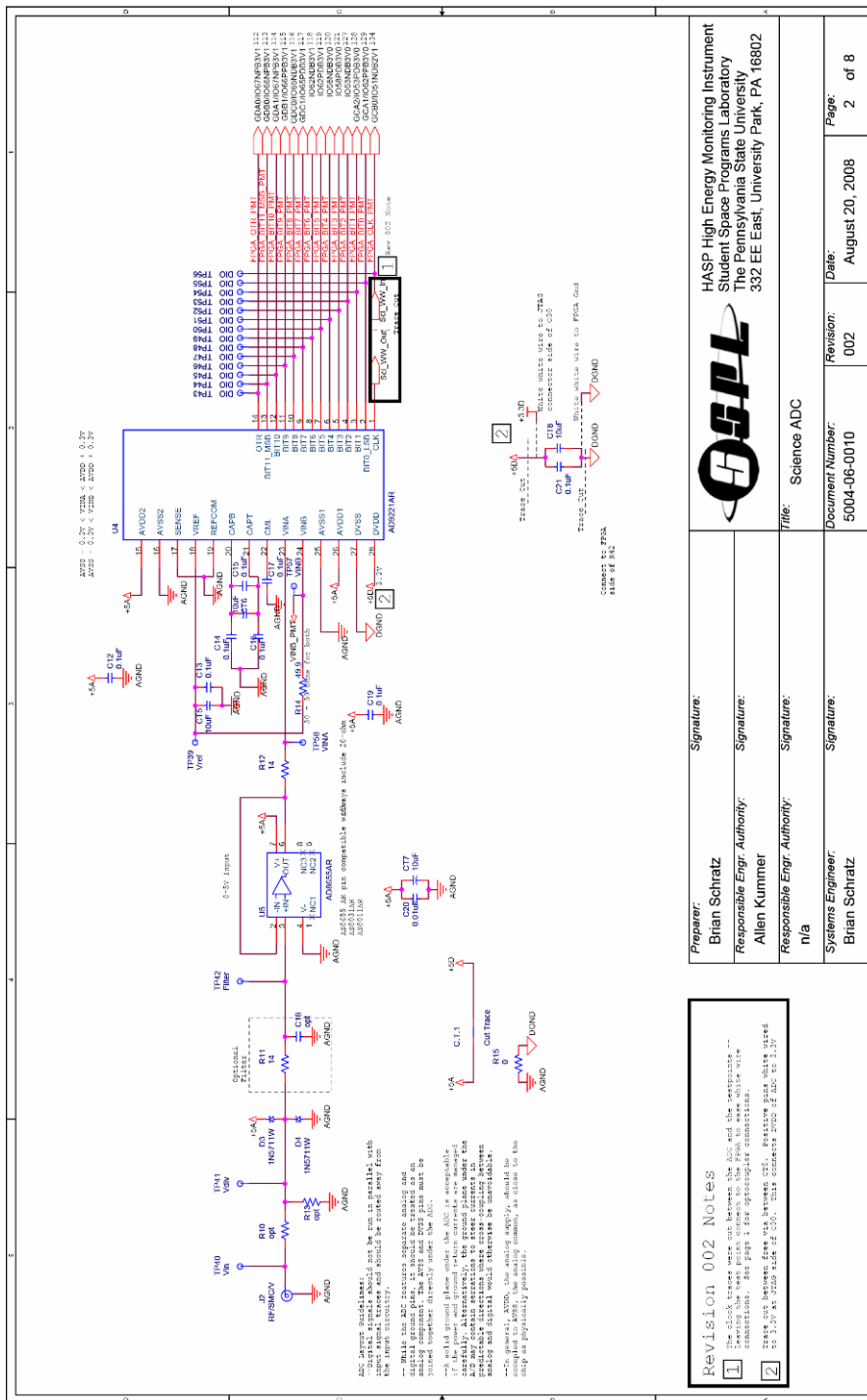Figure A.1: Schematic: MUX, ADC Converter for Health and Status Monitoring

129
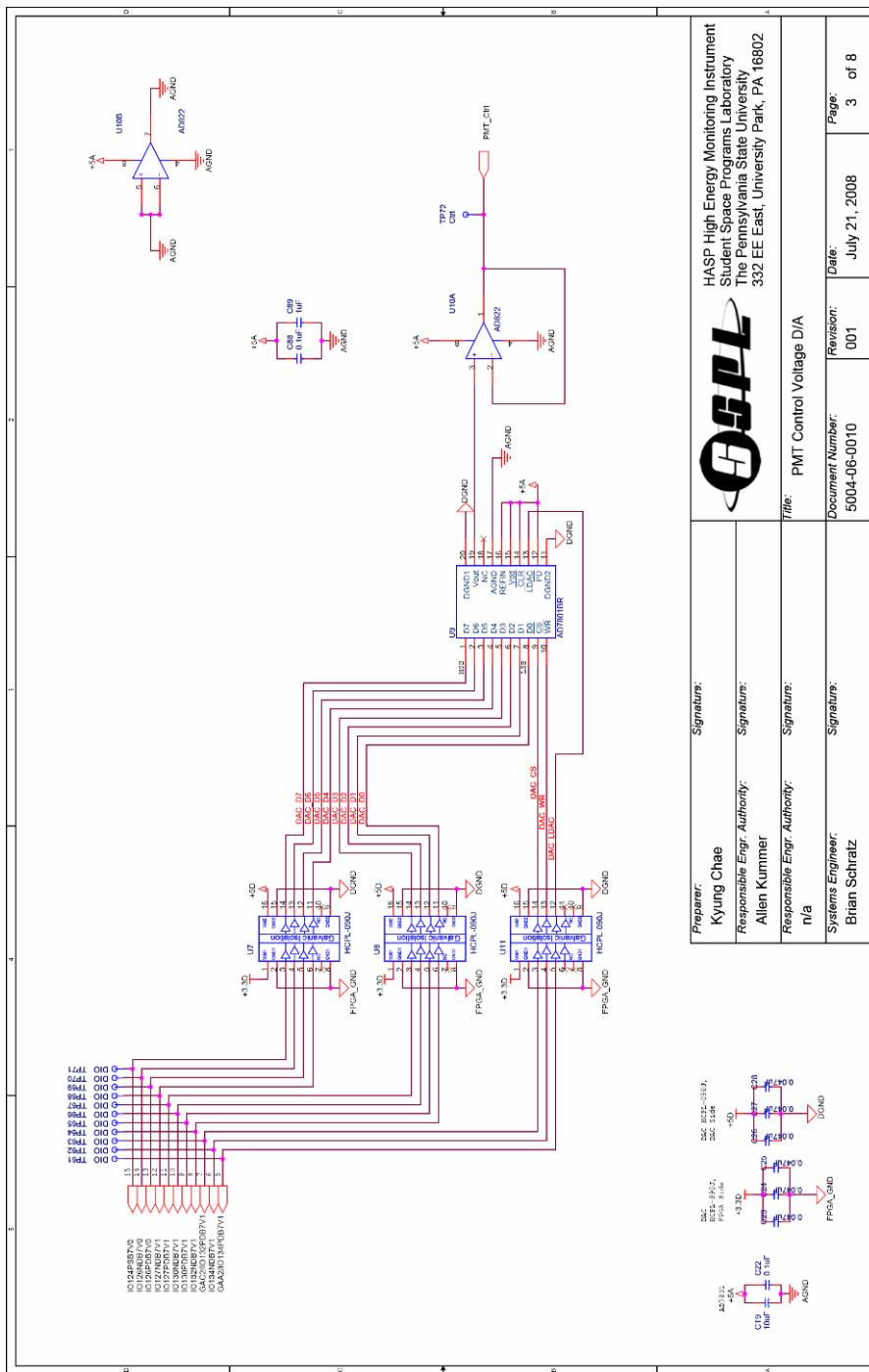

Figure A.2: Schematic: Science ADC

Figure A.3: Schematic: PMT Control Voltage Digital-to-Analog Converter

Figure A.4: Schematic: FPGA Capacitors

Figure A.5: Schematic: Power, Clock, RS232, JTAG
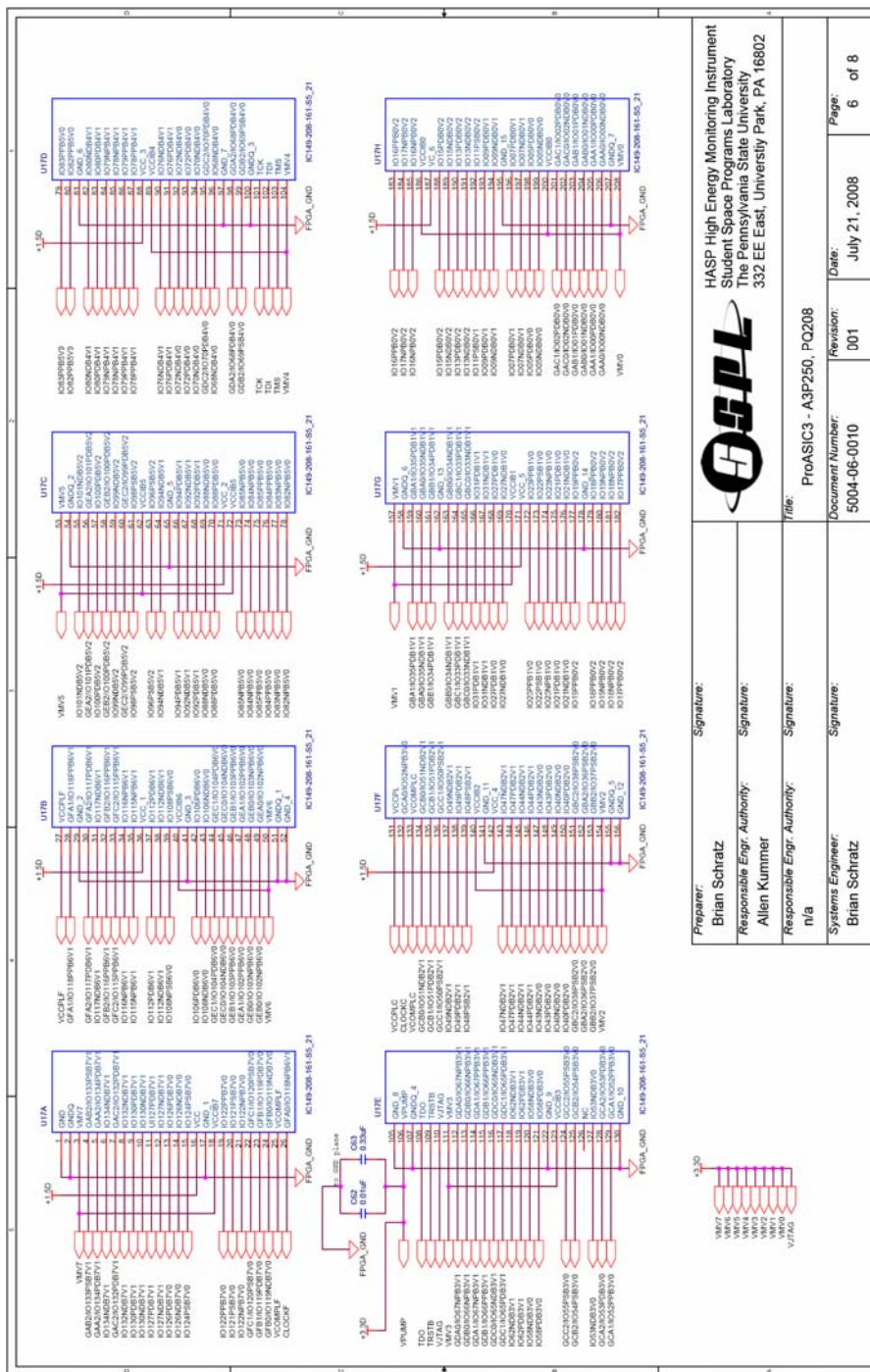
Figure A.6: Schematic: ProASIC3 – A3P250 PQ208

Figure A.7: Schematic: Safety Pressure/Temp Sensors Instrumentation Amps
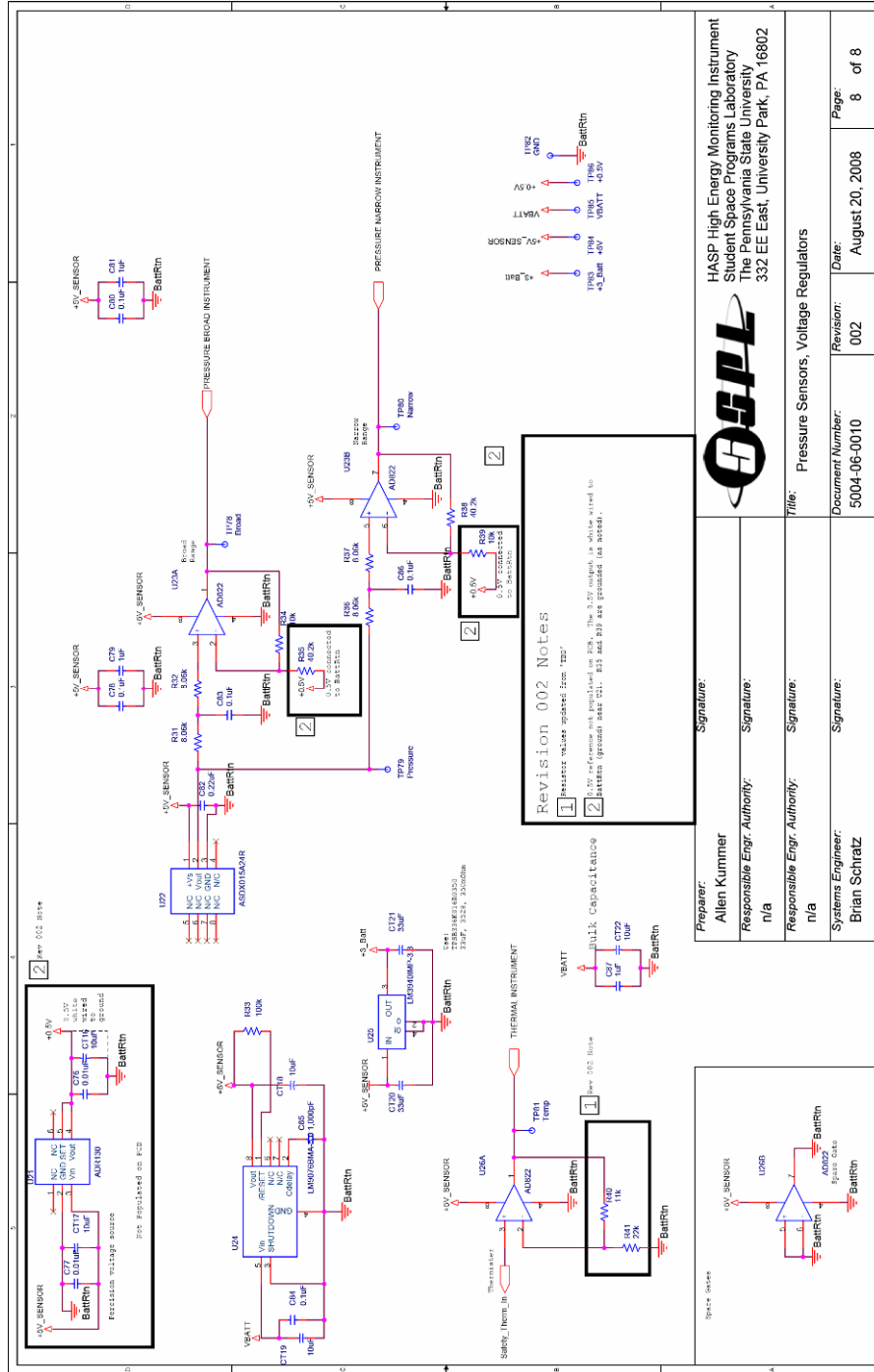
Figure A.8: Schematic: Pressure Sensor, Voltage Regulator

Appendix B

Flight Software and Configuration

This appendix contains the flight software used for this mission. The software was developed using the Libero® Integrated Development Environment v8.1 produced by the Actel Corporation who also manufactured the FPGAs used on HEMI. All flight software was written in Verilog. All references to specific hardware (i.e., FGPA, ADC, reset chip, clocks) refer to the hardware designs contained in Appendix A.

Several other earlier versions of the software exist that allowed for debugging various functions of the hardware. All of these preliminary programs are available through the SSPL document library.

B.1 Module "sci_test", Verilog file "top.v"

```verilog
// top.v
module sci_test(
    input clk_50,
    input reset,          // Active low reset

    input [7:0] adc_in,   // Data from the ADC
    output reg adc_clk,   // Clock for ADC

    output tx,            // Asyc TX output
    input  rx,            // Async RX input

    output above_threshold,  // debug signals
    output cur_val_higher,
    output peak_detected,
    output peaked,
    output deadband
    //output reg tx_busy
    );

// ***************************
```

```verilog
// Local wires/registers
// ****************************

   // Async Interface
   reg        wr;
   wire       baud_tx;
   wire       start_tx;
   wire        stop_tx;
   reg [7:0] data_tx;

   wire start_rx;
   wire valid_rx;
   wire stop_rx;
   wire baud_rx;
   wire [7:0] data_rx;


// ****************************
// Use active high reset in modules
// ****************************

wire rst;
assign rst = ~reset;


// ****************************
// Generate 5 MHz Clk for Async
// ****************************

reg clk_5;
reg [3:0] delay_5;

always @ (posedge clk_50)
  begin : CLOCKDIV

     delay_5 <= delay_5 + 1;

        if (delay_5 == 4'b0100) begin
           clk_5 <= ~clk_5;
           delay_5 <= 4'b0;
        end // IF

 end // CLOCKDIV


// ****************************
// Generate 2.5 MHz clk for ADC
// ****************************
 always @ (posedge clk_5) begin
   adc_clk <= ~adc_clk;
   end // ALWAYS

// ****************************
// Prevent Tx Overruns --> not necessary for science
// ****************************
```

```verilog
//
////// reg tx_busy;
//
//always @(posedge clk_5) begin
//
//   if( start_tx )
//       tx_busy <= 1'b1;
//   else if( stop_tx )
//       tx_busy <= 1'b0;
//
//end // ALWYAS
//

// *****************************
// Perform Peak Detection
// ****************************

//   1V = dec 51 = 8'b00110011
reg [7:0] threshold;
// assign threshold = 8'b00110011;

//wire peak_detected;
wire [7:0] max;

   peak_detect PEAK
     (
        .rst (rst),
        .adc_in (adc_in),
        .threshold (threshold),
        .adc_clk (adc_clk),
        .peak (peak_detected),
        .max (max),
        .above_threshold (above_threshold),
        .cur_val_higher (cur_val_higher),
        .peaked (peaked),
        .deadband (deadband)
     );

always @(posedge clk_5) begin   // was clk_50
   if( rst ) begin
      threshold <= 8'b00110011; // 1V
      wr <= 1'b0;
      //tx_busy <= 1'b0;

   end if( peak_detected || valid_rx ) begin
   // && ( !tx_busy)
      wr <= 1'b1;

      if(valid_rx) begin
         data_tx <= data_rx;
         threshold <= data_rx;

      end else begin
         data_tx <= max;
         threshold <= threshold;
```

```
        end // IF

    end else
        wr <= 1'b0;
end

// ****************************
// Instantiate Async Modules
// ****************************

    baud_clk BAUD_RX
      (
       .clk (clk_5),
       .rst (rst),
       .start(start_rx),
       .tx_mode(start_rx),
       .baud( baud_rx ),
       .stop( stop_rx )
       );

    uart_rx UART_RX
      (
       .clk (clk_5),
       .rst (rst),
       .baud(baud_rx & start_rx),
       .stop(stop_rx),
       .rx(rx),
       .data(data_rx),
       .valid(valid_rx),
       .start(start_rx)
       );


    baud_clk BAUD_TX
      (
       .clk (clk_5),
       .rst (rst),
       .start( start_tx),
       .tx_mode(start_tx),
       .baud( baud_tx ),
       .stop( stop_tx )
       );

    uart_tx UART_TX
      (
       .clk (clk_5),
       .rst (rst),
       .baud(baud_tx & start_tx),
       .stop(stop_tx),
       .tx(tx),
       .data(data_tx),
       .wr(wr),
       .start(start_tx)
       );
```

```
endmodule
```

B.2 Module "peak_detect", Verilog file "peak_detect.v"

```verilog
// peak_detect.v

module peak_detect(
    input rst,              // active high reset
    input [7:0] adc_in,     // data from the adc
    input [7:0] threshold,  // user threshold level
    input adc_clk,          // 2.5 MHz generated clock
    output reg peak,        // flag when 'max' is the peak
    output reg [7:0] max,   // stores current max value

    output reg above_threshold,  // debug signals
    output reg cur_val_higher,
    output reg peaked,
    output reg deadband
    );


// ****************************
// Clear ADC Pipeline on RST
// ****************************

reg [2:0] rst_cntr;
reg enabled;

always @(posedge adc_clk) begin
    if( rst) begin
        rst_cntr <= 3'b0;
        enabled <= 1'b0;

    end else if( rst_cntr < 3'b100 ) begin
        enabled <= 1'b0;
        rst_cntr <= rst_cntr +1;
    end else
        enabled <= 1'b1;

end // ALWAYS

// ****************************
// Sample ADC
// ****************************

reg [7:0] data;

// adc samples on rising edge
// data available at falling edge
always @(negedge adc_clk) begin
    if( enabled )
```

```verilog
      data <= adc_in;
   else
      data <= 8'b0;

end // ALWAYS

// ****************************
// Detect Peak
// ****************************

reg [5:0] dead_cntr;

// peak flag stays high for one adc_clk period

always @(posedge adc_clk) begin
   if( enabled ) begin
      if ( peak ) begin
         peak <= 1'b0;    // clear peak flag after detection
         max  <= 8'b0;    // reset stored max value

         // Deadband counter
         dead_cntr <= 6'h28; // 35 cycles = 14 usec

      end else if( dead_cntr > 0 ) begin
         dead_cntr <= dead_cntr - 1;  // still in the deadband period
         deadband <= 1'b1;            // used for debug

      end else if ( data > threshold ) begin

         deadband <= 1'b0;            // clear deadband if cntr = 0;
         above_threshold <= 1'b1;

         if(!peaked) begin

            if( data > max ) begin
               max <= data;  // keep waiting for the peak
               peak <= 1'b0;
               cur_val_higher <= 1'b1;

            end else begin
               max <= max;
               peak <= 1'b1; // the previous value was the peak
               peaked <= 1'b1;
               cur_val_higher <= 1'b0;

            end // IF data>max

         end // IF !peaked

      end else begin           // if data < threshold
         max  <= 8'b0;
         peak <= 1'b0;
         peaked <= 1'b0;
```

```
          cur_val_higher <= 1'b0;
          above_threshold <= 1'b0;
          deadband <= 1'b0;      // clear deadband if cntr = 0;

      end // IF data>threshold

   end else begin
      max <= 8'b0;
      peak <= 1'b0;
      deadband <= 1'b0;      // clear deadband if cntr = 0;
   end //IF


end // ALWAYS


endmodule
```

B.3 Module "uart_tx", Verilog file "uart_tx.v"

```
//---------------------------------------------------------------------
//  Student Space Programs Laboratory
//  The Pennsylvania State University
//  Copyright 2008
//
//---------------------------------------------------------------------
//   TITLE: Simple Async Transmitter
//
//   FILENAME: uart_tx.v
//   AUTHOR: Matthew Sunderland
//
//   DESCRIPTION:  This module implements a simple asynchronous
transmitter.
//   Compliant with RS-232/422/485 transmissions.  This module is
transmit
//   only, has no flow control, and no fifo.
//
//   Data format:  ST|b0|b1|b2|b3|b4|b5|b6|b7|SP
//   Data is LSB first, 8-bits, with no parity.
//
//   Clocking: The module muse be clocked at 4MHz and a baud rate clk.
The
//   baud rate must be a 50% duty cycle signal that is started ( first
neg
//   edge) when the start signal is sent. On each following pos edge, a
data
//   bit is written to the tx signal.
//
//   Transmitting: To transmit a data byte, two clock cycles are needed
to
//   set up the transmission. On the first cycle, data should be
written to
```

```verilog
//    the data signal. On the next clock cycle, (or anytime later as
long as
//    the data is still vailid) the wr signal is asserted for only one
clk
//    period.  This period between data and wr signal allows the uart to
//    calculate the parity bit.
//    The module will then complete the transmission on its own and
//    can be monitored by the reset of the start signal.
//
//    REVISION HISTORY:
//    2008-02-19: Initial Build
//    2008-08-01: Modified for HASP configuration (bcs)
//
//-----------------------------------------------------------------

module uart_tx
(
  //clks and reset
  input       clk,
  input       rst,
  input       baud,
  input       stop,
  // serial tx line
  output      tx,
  // data inputs
  input [7:0] data,
  input       wr,
  output      start
);

reg txing, tx_r;
reg [8:0] data_sr;

assign start = txing;
assign tx = tx_r;

always @( posedge clk )
begin
      if( rst | stop )
            txing = 1'b0;
      else if( wr )
            txing = 1'b1;
      else
            txing = txing;
end

always @( posedge baud or posedge wr)
begin
      if( wr ) begin
            tx_r <= 1'b1;
        data_sr <= {data,1'b0};
      end else begin
            tx_r <= data_sr[0];
            data_sr <= {1'b1,data_sr[8:1]};
      end
```

end

endmodule

B.4 Module "uart_rx", Verilog file "uart_rx.v"

```
//----------------------------------------------------------------------
//   Student Space Programs Laboratory
//   The Pennsylvania State University
//   Copyright 2008
//
//----------------------------------------------------------------------
//    TITLE: Simple Async Receiver
//
//    FILENAME: uart_rx.v
//    AUTHOR: Matthew Sunderland
//
//    DESCRIPTION:  This module implements a simple asynchronous
receiver.
//    Compliant with RS-232/422/485 transmissions.  This module is
receive
//    only, has no flow control, and no fifo.
//
//    Data format:  ST|b0|b1|b2|b3|b4|b5|b6|b7|pe|SP
//    Data is LSB first, 8-bits, and appended by one even parity bit.
//    Parity bit: pe = b0^b1^b2^b3^b4^b5^b6^b7
//
//    Clocking: The module muse be clocked at 4MHz and a baud rate clk.
The
//    baud rate must be a 50% duty cycle signal that is started (1st neg
//    edge) when the start signal is sent. On each following pos edge, a
//    data bit is read from the rx signal.
//
//
//
//    REVISION HISTORY:
//    2008-02-19: Initial Build
//    2008-08-01: Modified for HASP configuration (bcs)
//
//----------------------------------------------------------------------

module uart_rx
(
// Clocking and Reset
  input     clk,
  input     rst,
  input     baud,
  input     stop,
// Received signal
  input     rx,
```

```verilog
// Ouptut
  output [7:0] data,
  output valid,
  output start
);

reg started;
reg [8:0] data_r;

always @( posedge clk )
begin
      if( rst )
            started = 1'b0;
      else if( ~rx )
            started = 1'b1;
      else if( stop )
            started = 1'b0;
      else
            started = started;
end

always @( posedge baud )
begin
  data_r <= 10'd0;
  if( rst )
      data_r <= 10'd0;
  else
    //data_r <= {rx, data_r[9:1]};
      data_r <= {rx, data_r[8:1]};
end

assign valid = stop & rx;
assign start = started;
assign data = data_r[7:0];

endmodule
```

B.5 Module "baud_clk", Verilog file "baud_clk.v"

```verilog
//----------------------------------------------------------------------
//  Student Space Programs Laboratory
//  The Pennsylvania State University
//  Copyright 2008
//
//----------------------------------------------------------------------
//   TITLE: Simple Async Receiver
//
//   FILENAME: baud_clk.v
//   AUTHOR: Matthew Sunderland
//
```

```verilog
//   DESCRIPTION:  This module generates a baud rate clock for use with
the
//   simple uart_rx,tx modules. It starts when receiving the start
signals,
//   counts out 11 signals, and then sends the stop signal when
clocking the
//   eleventh bit (stop bit).
//
//   REVISION HISTORY:
//   2008-02-19: Initial Build
//   2008-02-27: changed to non-blocking assignments
//   2008-08-01: Modified for HASP configuration (bcs)
//
//------------------------------------------------------------------
//`define BAUD_COUNT 130 //Must be an even number
//`define TX_BITS 11
//`define RX_BITS 10


`define TX_BITS 10
`define RX_BITS 9

module baud_clk
(
      input clk,
        input rst,
      input start,
        input tx_mode,
      output baud,
      output stop
);

reg [10:0] baud_cntr;
reg [4:0] bit_cntr;
wire [3:0] bits;
reg stop_r;

assign baud = bit_cntr[0];
assign stop = stop_r;
assign bits = tx_mode ? `TX_BITS : `RX_BITS;

always @( posedge clk )
begin
  if ( rst ) begin
    baud_cntr <= 11'h209;  // was defined as BAUD_COUNT / 2
    bit_cntr  <= 0;
    stop_r    <= 0;
  end
  if( start ) begin
        bit_cntr <= bit_cntr;

      baud_cntr <= baud_cntr+1;
        stop_r <= 0;
      if( baud_cntr == 11'h412-1 ) begin  // was defined as BAUD_COUNT
              baud_cntr <= 11'd0;
```

```
            bit_cntr <= bit_cntr+1;
            if( bit_cntr[4:1] == bits ) begin
                    bit_cntr <= 0;
                stop_r <= 1;
            end
        end
    end
end

endmodule
```

B.6 FPGA Pin Connections

Table B.1 lists the port configurations for all of the FPGA I/O pins. In addition to the properties listed below, all ports have no pull-up resistors and are tri-state during programming. All output ports have an output drive of 12 mA, high slew, and an output load of 35 pF.

Table B.1: FPGA Port Configuration

Port Name	Macro Cell	Pin #	Bank Name	I/O Standard
peaked	ADLIB:OUTBUF	4	Bank3	LVTTL
above_threshold	ADLIB:OUTBUF	5	Bank3	LVTTL
cur_val_higher	ADLIB:OUTBUF	6	Bank3	LVTTL
peak_detected	ADLIB:OUTBUF	7	Bank3	LVTTL
deadband	ADLIB:OUTBUF	8	Bank3	LVTTL
tx	ADLIB:OUTBUF	19	Bank3	LVTTL
rx	ADLIB:INBUF	20	Bank3	LVTTL
clk_50	ADLIB:INBUF	26	Bank3	LVTTL
reset	ADLIB:INBUF	90	Bank2	LVTTL
adc_in[7]	ADLIB:INBUF	113	Bank1	LVCMOS33
adc_in[6]	ADLIB:INBUF	114	Bank1	LVCMOS33
adc_in[5]	ADLIB:INBUF	115	Bank1	LVCMOS33
adc_in[4]	ADLIB:INBUF	116	Bank1	LVCMOS33
adc_in[3]	ADLIB:INBUF	117	Bank1	LVCMOS33
adc_in[2]	ADLIB:INBUF	118	Bank1	LVCMOS33
adc_in[1]	ADLIB:INBUF	119	Bank1	LVCMOS33
adc_in[0]	ADLIB:INBUF	120	Bank1	LVCMOS33
adc_clk	ADLIB:OUTBUF	134	Bank1	LVCMOS33

B.7 FPGA Design Margins

The current design using the hardware and software described in this document

uses a total of 433 of 6144 (7%) Core Cells and 18 I/O Cells, and 0 of 8 Block Rams.

B.8 Module "AD7801.v" (not flown)

```
// Student Space Programs Laboratory
```

```verilog
// The Pennsylvania State University
// Copyright 2008
//
//-------------------------------------------------------------------
//    TITLE: Simple AD7801
//
//    FILENAME: AD7801.v
//    AUTHOR: Kyung Chae
//
//    DESCRIPTION: This Module runs signals to D/A convertor chip,
//      converting 8 bits data an anolog signal to control PMT control
//      voltage. Change has to be at high input in order to run any
//      signals and enable controls flags when to start updating the
//      outp_D7_D0 to control the PMT_ctrl voltage.  Both change and
//      enable has to be at high for Data to load to DAC7801.
//
//    Clocking: This module must have internal clk less than 50MHz since
//      LDAC setup time equals 20ns.
//
//
//
//
//
//    REVISION HISTORY:
//    2008-07-21: Modified for
//    2008-05-30: Initial build
//
//-------------------------------------------------------------------

`timescale 1ns / 10ps

module AD7801(
input clock,
input reset,
input change,
input enable,
// output clk

input [7:0] outp_D7_D0,
output reg [7:0] PMT_Ctrl,
output reg [2:0] conditions
);

//registers
reg outp_CS;
reg outp_WR;
reg outp_LDAC;
reg [19:0] delay ;
reg clk ;
reg [2:0] state;
parameter CS = 3'b000;
parameter CS_OFF = 3'b110;
parameter WR_OFF = 3'b100;
parameter WR = 3'b001;
parameter D7_D0 = 3'b010;
```

```verilog
parameter LDAC_ON = 3'b011;
parameter LDAC_OFF = 3'b101;


always @ (posedge clk)
conditions = {outp_LDAC, outp_WR, outp_CS};


// divids clock with 50MHz frequency with 10MHz, gets new clk with
delay of 10MHz
always @ (posedge clock)
    begin: Clock_Div

        if (delay == 20'hf4240) begin
            clk <= ~clk;
            delay <= 0;
        end

    delay <= delay +1;

    end

// wr, cs, ldac is switched one by one so it has enough delay for next
signal to
// register to the dac chip.  Data is also timed so that it is loaded
when ldac
// is activated.  Also, state cs and wr waits for the

always @ (posedge clk)
    begin : OUTPUTS

    if (reset == 1'b0)
        begin
            state <= CS;
            outp_CS <= 1'b1;
            outp_WR <= 1'b1;
            PMT_Ctrl <= 8'b00000000;
            outp_LDAC <= 1'b1;
        end

     else if (change == 1'b1)
        begin
        case(state)
            CS: begin
                state <= WR;
                outp_CS <= 1'b0;
                outp_LDAC <= 1'b1;
                outp_WR <= 1'b1;
                end
            WR: begin
                if (enable == 1'b1)
                    begin
                state <= D7_D0;
                    end
                if (enable == 1'b0)
```

```verilog
                  begin
               state <= WR;
                   end
           outp_WR <= 1'b0;
           end
       D7_D0: begin
           state <= WR_OFF;
           PMT_Ctrl <= outp_D7_D0;
           end
       WR_OFF: begin
           state <= CS_OFF;
           outp_WR <= 1'b1;
           end
       CS_OFF: begin
           state <= LDAC_ON;
           outp_CS <= 1'b1;
           end
       LDAC_ON: begin
           state <= LDAC_OFF;
           outp_LDAC <= 1'b0;
           end
       LDAC_OFF: begin
           state <= CS;
           outp_LDAC <= 1'b1;
           end
   endcase
   end // else

   end // OUTPUTS

endmodule
```

Appendix C

Automated Peak Detection and Data Acquisition Software

      The MATLAB software package was used extensively throughout this project for the testing and calibration of the system of photomultiplier tube, crystal scintillator, and custom instrument electronics in various configurations. The goal was first to characterize accurately the PMT and crystal using an oscilloscope, and then to compare those results to the instrument hardware.

      In all tests, either the oscilloscope, instrument electronics, or both, performed the peak detection. During the oscilloscope tests, the scope was controlled autonomously through MATLAB and the GPIB connection. The instrument electronics interfaced through an asynchronous RS-232 communication interface. This section contains the source code for each of these programs.

C.1 PMT Only with Oscilloscope

```
function PMT_Trigger()

%open oscilloscope
scope = gpib('NI', 1, 7);
fopen(scope);

%open power supply
supply = gpib('NI', 1, 5);
fopen(supply);

%create text file
textfile=fopen('test.txt','at');

triggered = 0;
fprintf(scope,'*CLS');
```

```
% Format Text File Header
fprintf(textfile,'\n*************************************\n');
fprintf(textfile,'*   HEMI                            *\n');
fprintf(textfile,'*   Vacuum Chamber Test             *\n');
fprintf(textfile,'*                                   *');
fprintf(textfile,'\n*************************************');
fprintf(textfile,'\nTime\t\t\tWidth\t\tMaximum\t\tMinimum\t\tBase\n');

clc

while(1)

    % wait for a trigger
    while(not(triggered))
        fprintf(scope,'*STB?');
        idn=fscanf(scope);
        idn = str2num(idn);
        triggered = bitand(idn,1)
    end

    % measure data on curve and PMTs
    fprintf(scope,'MEAS:PWID?');
    idn = fscanf(scope);
    width = str2num(idn);
    fprintf(scope,'MEAS:VMAX?');
    idn = fscanf(scope);
    maximum = str2num(idn);
    fprintf(scope,'MEAS:VMIN?');
    idn = fscanf(scope);
    minimum = str2num(idn);
    fprintf(scope,'MEAS:VBAS?');
    idn = fscanf(scope);
    base = str2num(idn);

    % write data to text file
    timestamp = datestr(now,'HH:MM:SS.FFF AM');

fprintf(textfile,sprintf('%s\t\t%3.3E\t%3.3E\t%3.3E\t%3.3E\n',timestamp
,width,maximum,minimum,base));
    disp(sprintf('Max = %6.4f',maximum));

    % Clear the flag
    fprintf(scope,'*CLS')
    triggered = 0;

    % Set back to single trigger
    fprintf(scope,'SING');

end

% close everything and place everything below in command window after
you
% are done running the program
fclose(textfile)
```

```
fclose(scope)
delete(scope)
fclose('all');

newobjs = instrfind
fclose(newobjs)
```

C.2 PMT with Instrument Electronics and Oscilloscope Comparison

```
function PMT_Trigger_CDH()

%open oscilloscope
scope = gpib('NI', 0, 7);
fopen(scope);

%create text file
textfile=fopen('CDH_test3.txt','at');

%open RS232 port
rs232 =
serial('COM1','BaudRate',2400,'Parity','none','StopBits',1,'FlowControl
','none');
fopen(rs232);

triggered = 0;
fprintf(scope,'*CLS');

% Format Text File Header
fprintf(textfile,'\n*************************************\n');
fprintf(textfile,'  HEMI                                \n');
fprintf(textfile,'  CDH vs Scope Test              \n');
fprintf(textfile,'                                      ');
fprintf(textfile,'\n*************************************');

%% Get User Input for Test Conditions
reply = input(sprintf('Describe test conditions\n(timestamp
automatically included)'),'s');
fprintf(textfile,sprintf('** Test started: %s\n',datestr(now)));
fprintf(textfile,sprintf('** Test conditions: %s\n',reply));

fprintf(textfile,'\nTime\t\t\tMaxPMT\tMaxADC\tAsync\tV calculated from
Async\n');

clc

%% flush Async input buffer
bytes = rs232.BytesAvailable
if(bytes>0)
    async = fread(rs232,bytes,'uint8');
    disp('Flushing Buffer');
    disp(async);
```

```
    disp('-----')
end

while(1)

    % wait for a trigger
    while(not(triggered))
        fprintf(scope,'*STB?');
        idn=fscanf(scope);
        idn = str2num(idn);
        triggered = bitand(idn,1);
    end

    %% Record CDH measurement
    async = fread(rs232,1,'uint8');

    %% Measure PMT signal directly (Channel 1)
    fprintf(scope,'MEAS:SOUR CHAN1');

    fprintf(scope,'MEAS:VMAX?');
    idn = fscanf(scope);
    maxPMT = str2num(idn);

    %% Measure input to ADC (Channel 2)
    fprintf(scope,'MEAS:SOUR CHAN2');

    fprintf(scope,'MEAS:VMAX?');
    idn = fscanf(scope);
    maxADC = str2num(idn);
    maxADC_V = async.*(2.5/255);


    % write data to text file
    timestamp = datestr(now,'HH:MM:SS.FFF AM');

fprintf(textfile,sprintf('%s\t\t%6.4f\t%6.4f\t%i\t%6.4f\n',timestamp,ma
xPMT,maxADC,async,maxADC_V));

disp(sprintf('%s\t\t%6.4f\t%6.4f\t%i\t%6.4f',timestamp,maxPMT,maxADC,as
ync,maxADC_V));

    % Clear the flag
    fprintf(scope,'*CLS')
    triggered = 0;

    % Set back to single trigger
    fprintf(scope,'SING');

end

% close everything and place everything below in command window after
you
% are done running the program
fclose(textfile)
fclose(scope)
```

```
delete(scope)

% Close RS232
fclose(rs232);
delete(rs232);
clear rs232;

fclose('all');

newobjs = instrfind
fclose(newobjs)
```

C.3 PMT with Instrument Electronics Only, Configured for Flight

[Only Data Logging]

```
function PMT_CDH_Async_Only()

%open oscilloscope
% scope = gpib('NI', 0, 7);
% fopen(scope);

%create text file
textfile=fopen('FlightTest.txt','at');

%open RS232 port
rs232 =
serial('COM7','BaudRate',2400,'Parity','none','StopBits',1,'FlowControl
','none');
fopen(rs232);

% triggered = 0;
% fprintf(scope,'*CLS');

% Format Text File Header
fprintf(textfile,'\n*************************************\n');
fprintf(textfile,'   HEMI                              \n');
fprintf(textfile,'   Instrument Flight Test            \n');
fprintf(textfile,'                                     ');
fprintf(textfile,'\n*************************************');

%% Get User Input for Test Conditions
reply = input(sprintf('Describe test conditions\n(timestamp
automatically included)'),'s');
fprintf(textfile,sprintf('** Test started: %s\n',datestr(now)));
fprintf(textfile,sprintf('** Test conditions: %s\n',reply));

fprintf(textfile,'\nTime\t\t\tAsync\tConverted Volts\n');

clc
```

```matlab
%% flush Async input buffer
bytes = rs232.BytesAvailable
if(bytes>0)
    async = fread(rs232,bytes,'uint8');
    disp('Flushing Buffer');
    disp(async);
    disp('-----')
end

while(1)

    %% Record CDH measurement
    async = fread(rs232,1,'uint8');
    volts = async.*(5/255);

    % write data to text file
    timestamp = datestr(now,'HH:MM:SS.FFF AM');

fprintf(textfile,sprintf('%s\t\t%i\t%6.4f\n',timestamp,async,volts));
    disp(sprintf('%s\t\t%i\t%6.4f',timestamp,async,volts));

end

% close everything and place everything below in command window after
you
% are done running the program
fclose(textfile)

% Close RS232
fclose(rs232);
delete(rs232);
clear rs232;

fclose('all');

newobjs = instrfind
fclose(newobjs)
```

Appendix D

MATLAB Data Analysis Software - Parsing

During flight, the HASP system collected the science data from HEMI into raw data files and made the files available over a near real-time web interface when the file size reached a nominal 25 kB. Since each data point recorded by HEMI is 1 byte in length, each data set contains 25,000 data points. The data are stored in the order each point was received, rather than as a binned energy spectrum.

During flight, it was important to be able to view a quick look of the data as it was received to verify the operation of the instrument and to make decisions about leaving the instrument on or off. Therefore, a MATLAB script was developed to automatically parse an individual raw data file and produce several data products useful for real-time analysis and eventual post-flight analysis:

- Parse the received binary file and create an ASCII text file representing all of the peaks detected by HEMI;

- Form an energy spectra of the data, listing how many times each discrete peak value was recorded;

- Graph the data showing the number of each peak voltage (proportional to energy) for easy interpretation; and

- Save the processed text and graphical data with the name of the raw data file for easy referencing later—the graph is saved as both an editable MATLAB figure (.m), and as a lossless Tagged Image File Format (*.tiff) image.

In addition to science data, temperature, voltage, and current values were recorded by HASP and saved to similar files. Separate MATLAB parsing programs were created to combine all of these files into single text files that can be imported into MATLAB or Excel for future analysis.

D.1 HEMI/HASP Flight Data Processing File "hasp_parse"

```
function [total, bytes_received] = hasp_parse(filename)

% HEMI/HASP Flight Data Processing File
%
% Document #: 5004-09-0003

% Written by Brian Schratz, 12 September 2008
%
% Description:
% This program receives the filename of the raw data file in binary
format
% to process.  The data file must be in the same folder as this
program.
%
% The program returns a Nx2 array where N is the number of unique peak
% values detected.  The array will be sorted by increasing peak value
in
% row 1.  Row two is the number of times that value occurred.
%
% The returned value 'bytes_received' represents how many total values
were
% contained by the original binary file.
%
% In addition to returned data, the program will graph the data showing
the
% number of unique values as a function of unique value.  This plot
will be
% saved as a .tif file and an editable .m file with filenames matching
the
% original input filename.  These plots will be stored in the same
% directory as the current MATLAB working directory.
%
% Revision History:
% 001  First Public Release,  Brian Schratz
%
%------------------------------------------------------------------------
----

%% Open data files for reading/writing, set initial conditions
```

```matlab
fin = fopen(filename,'r');

[filename,r]=strtok(filename,'.');
fout = fopen(sprintf('%s.txt',filename),'at');

bytes_received = 0;
data_i = 1;

%% Parse the binary file
while ~isempty(data_i)
    data_i = fread(fin,1,'uint8');
    data_f = data_i .* (5/255);

    if ~isempty(data_i)
        fprintf(fout,sprintf('%i %6.4f\n',data_i,data_f));
        bytes_received = bytes_received + 1;
    end

end

%% Close data files
fclose(fout);
fclose(fin);

%% Load processed data for analysis
data = load(sprintf('%s.txt',filename));
unique = [];

%% Create vector of unique values
for i=1:length(data)
    x = find(unique == data(i,2));

%   if the value doesn't already exist
%   store the value in the copy array
    if isempty(x)
        unique(length(unique)+1)=data(i,2);
    end
end

%% Count how many of each value exists
for i=1:length(unique)
    x=find(data(:,2) == unique(i));
    counts(i)=length(x);
end

%% Sort values and plot the results
total=[unique;counts]';
total=sortrows(total,1);
h=plot(total(:,1),total(:,2),'.');
title(sprintf('%s',filename))
xlabel('voltage')
ylabel('counts')

%% Save the plot
saveas(gcf,sprintf('%s',filename),'tif')
```

```
saveas(gcf,sprintf('%s',filename),'fig')
```

D.2 HASP ADC Flight Data Processing File "hasp_parse_ADC"

```
function hasp_parse_adc(input_files)

% HASP ADC Flight Data Processing File
%
% Document #: 5004-09-0004

% Written by Brian Schratz, 29 September 2008
%
% Description:
% This program receives the a cell array of all the *.adc data files.
% Each cell must contain the complete filename with extension enclosed
% in single quotes.  For example:
%                                '1a02-259-04-33-21.adc'
%
% The data file must be in the same folder as this program and the
working
% directory for MATLAB.
%
% The program returns a single text file with the data for the entire
% flight
%
% Revision History:
% 001  First Public Release,  Brian Schratz
%
%----------------------------------------------------------------------
-

%% Open master data file for writing, set initial conditions
fout = fopen('adc_all.txt','at');

files_completed = 0;

%% Open data file for reading
for i=1:length(input_files)

    filename = char(input_files(i));
    fin = fopen(filename,'r');

    %% Parse the binary file
    data = textscan(fin,'%s %f %f %f %f %f %f %f %f %f %f %f %f %f
%f %f %f %f %f %f %f %f %f %f %f %f %f %f %f %f %f %u %u %u %u %u %u
%u %u %u %u %u %u %u %u %u %u %u %u %u %u %u %u %u %u %u %u %u %u %u %u
%u %u','headerLines',1,'delimiter',';');

    for m=1:length(data{1,1}) % row
        fprintf(fout,sprintf('\n%s',data{1,1}{m,1}));
```

```
        for n=2:33 %column
            fprintf(fout,sprintf(';%f',data{1,n}(m)));
        end
    end
    clear('data');
    fclose(fin);

    files_completed = files_completed + 1;
    disp(sprintf('File "%s" complete (%i/%i) . .
.',filename,files_completed,length(input_files)));
end

disp('Done')
%% Close data files
fclose(fout);
```

Appendix E

Mechanical Drawings
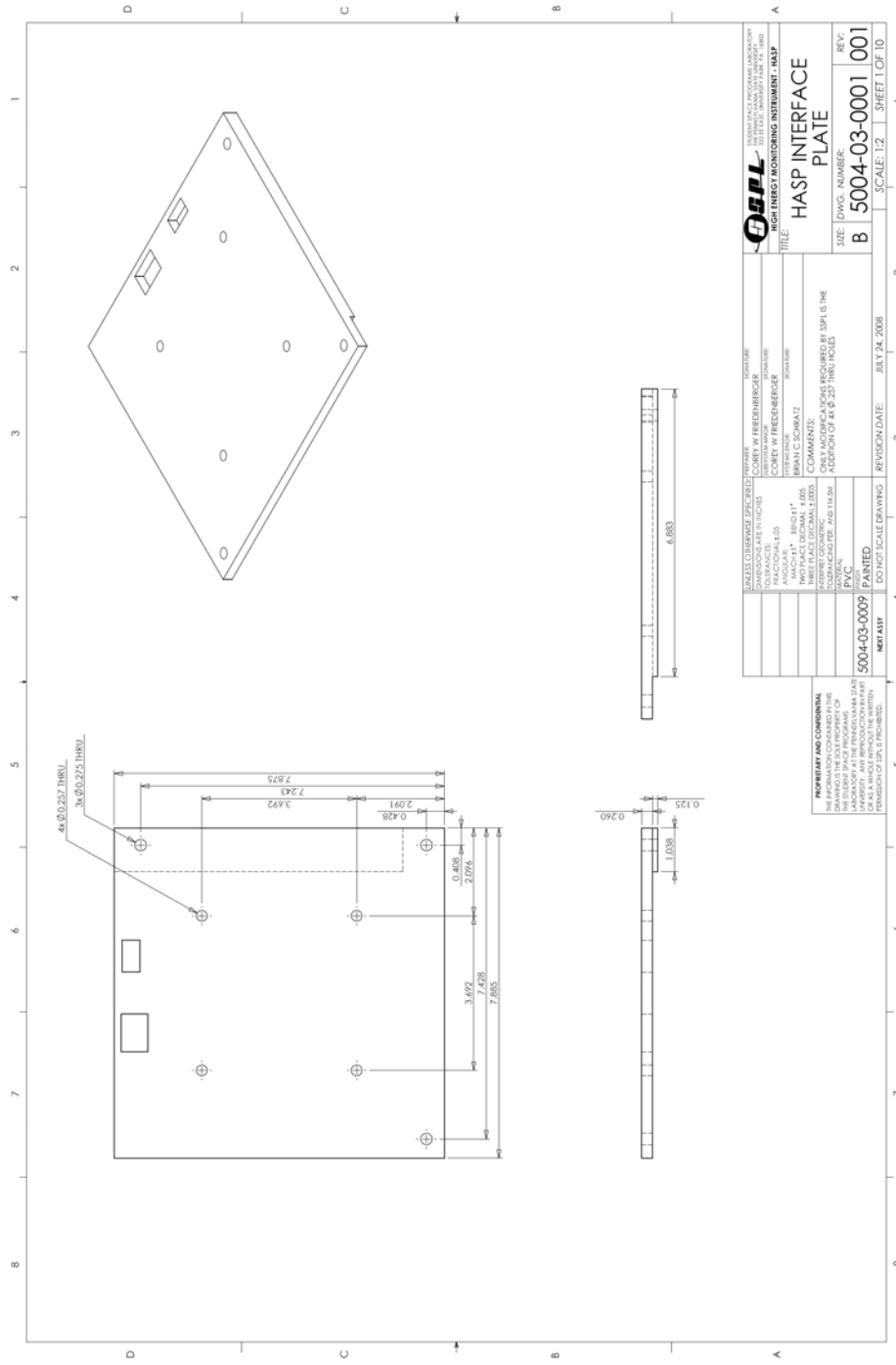
Figure E.1: Mechanical Drawing: HASP Interface Plate
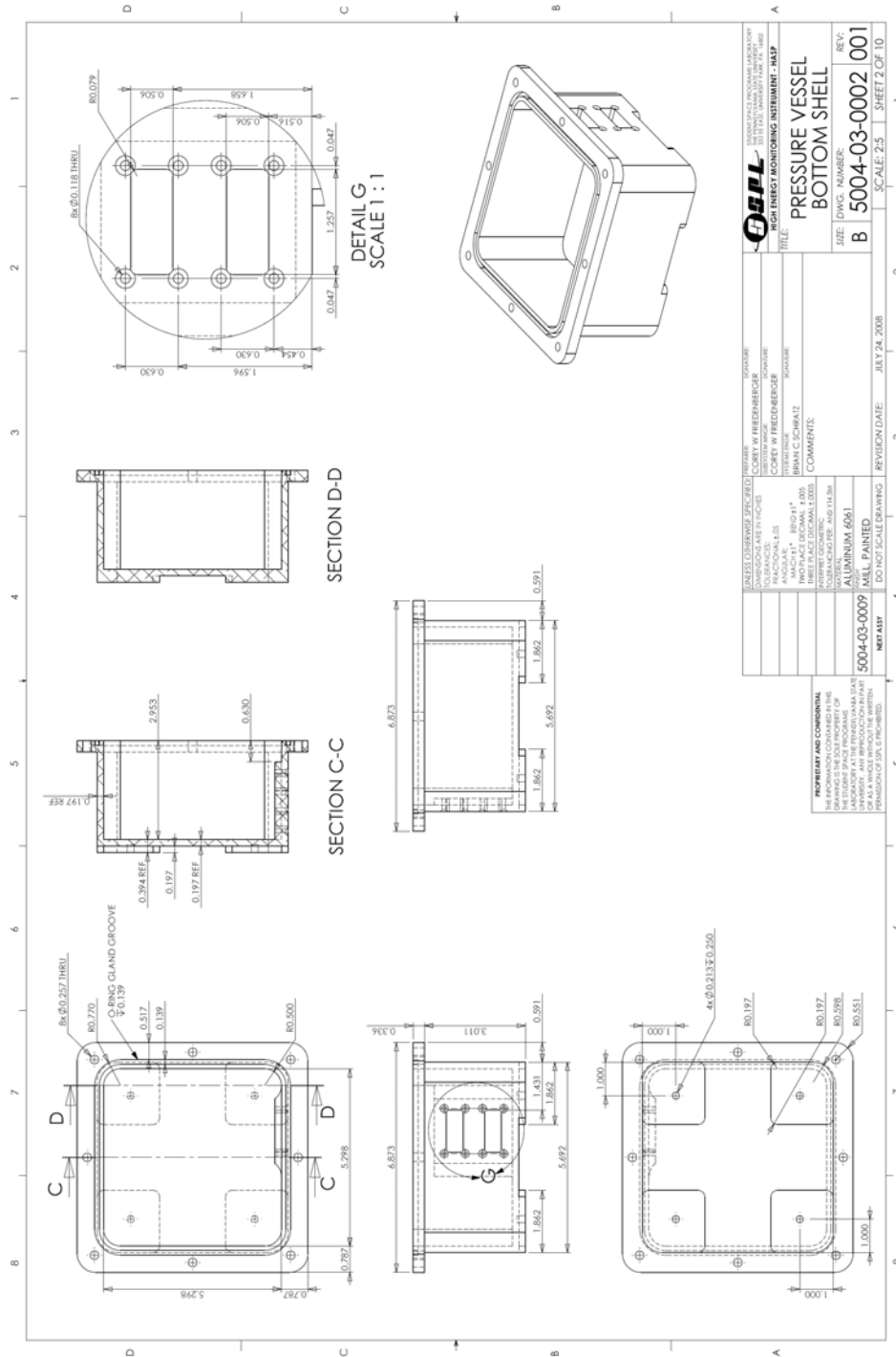
Figure E.2: Mechanical Drawing: Pressure Vessel Bottom Shell
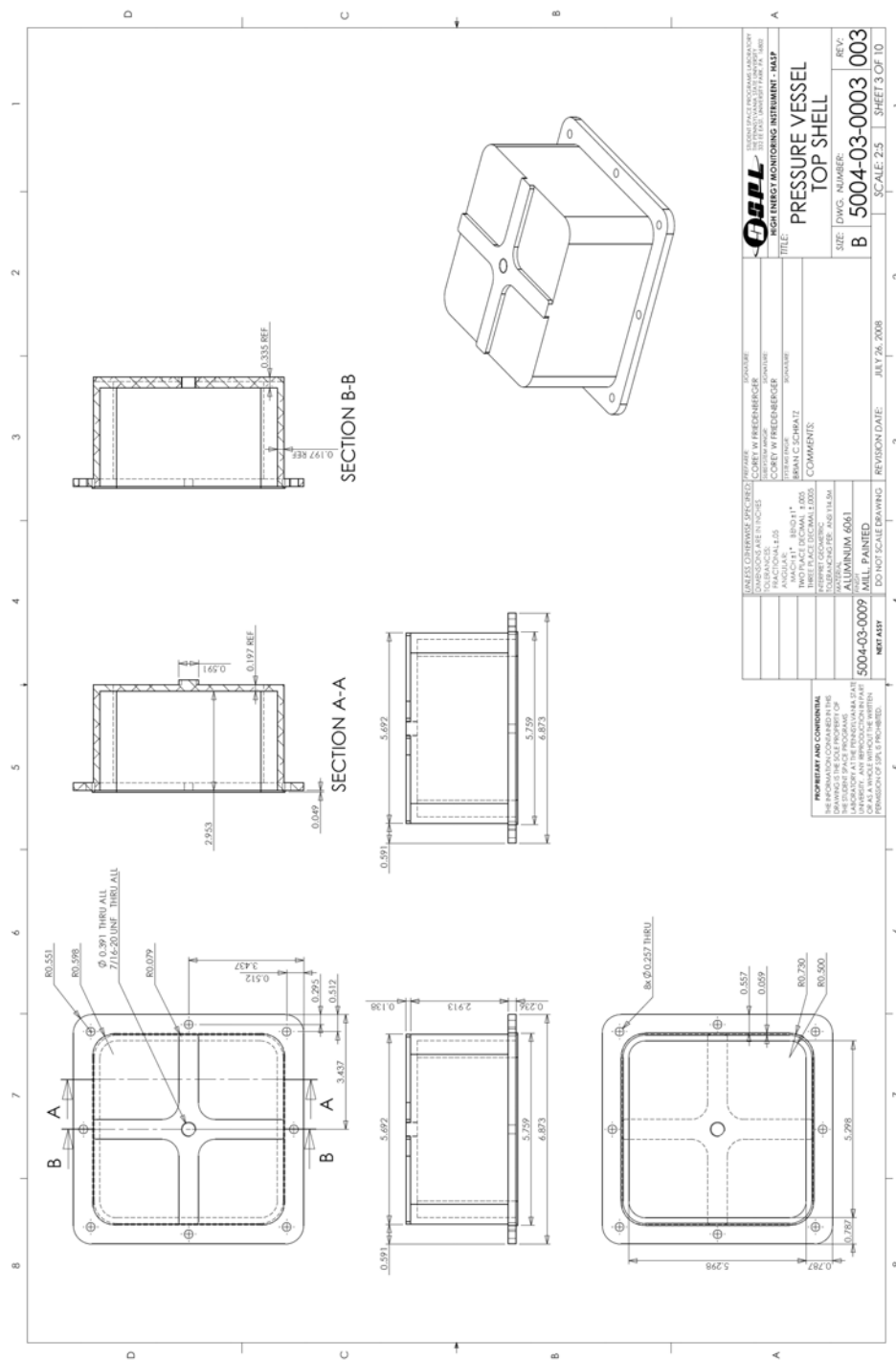
Figure E.3: Mechanical Drawing: Pressure Vessel Top Shell
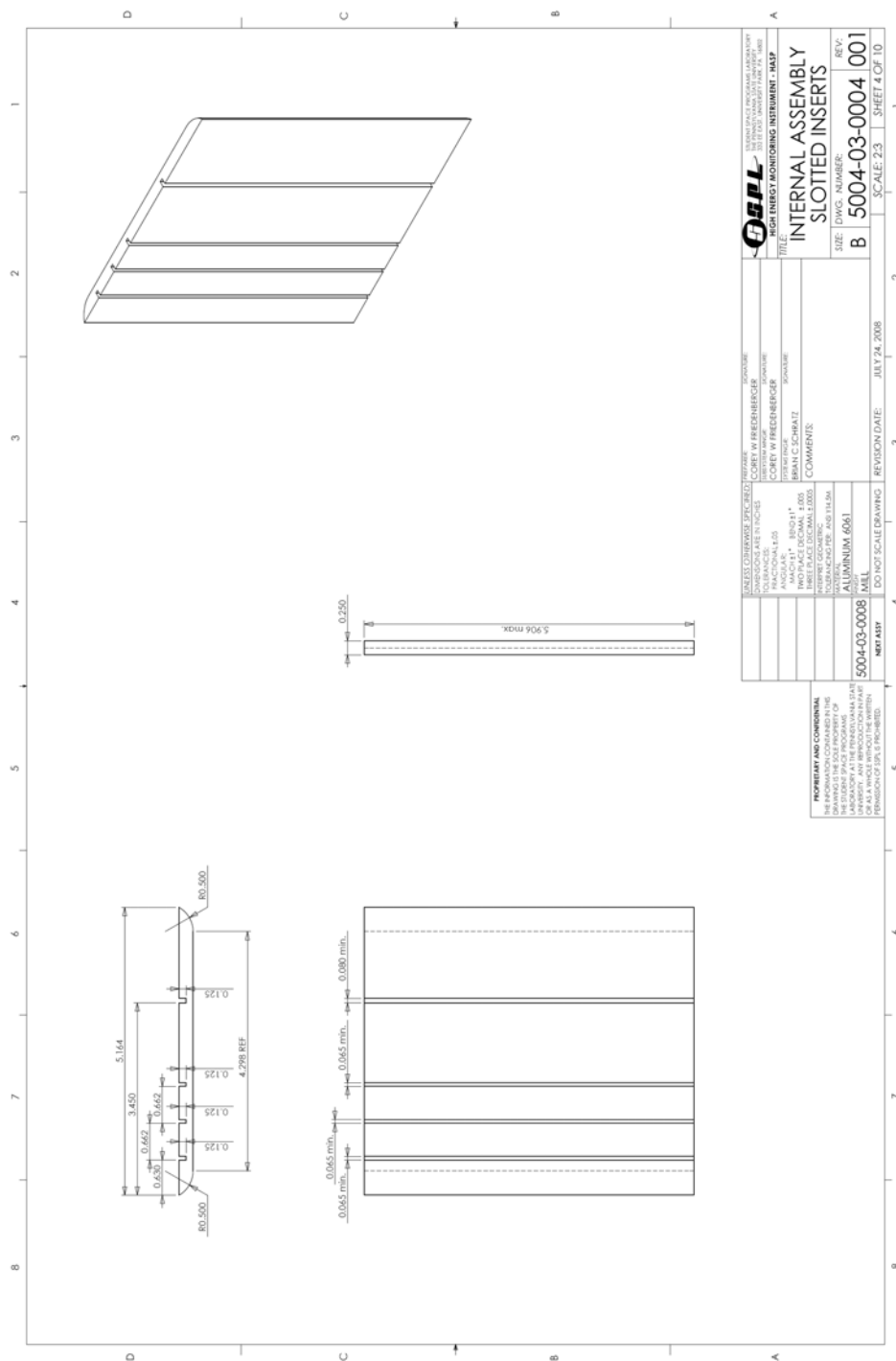
Figure E.4: Mechanical Drawing: Internal Assembly Slotted Inserts
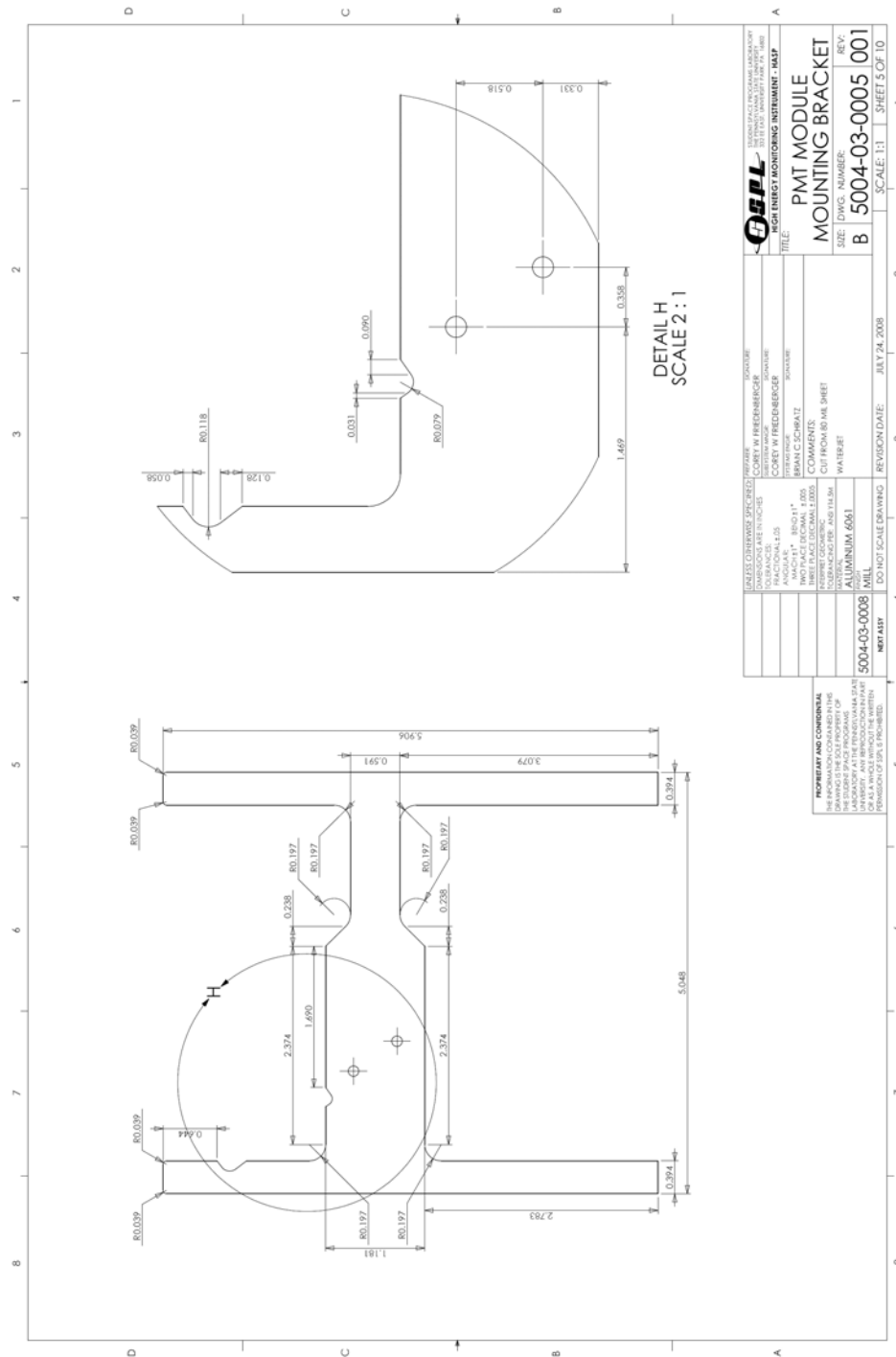
Figure E.5: Mechanical Drawing: PMT Module Mounting Bracket

Figure E.6: Mechanical Drawing: 5-V Board EMI Shield
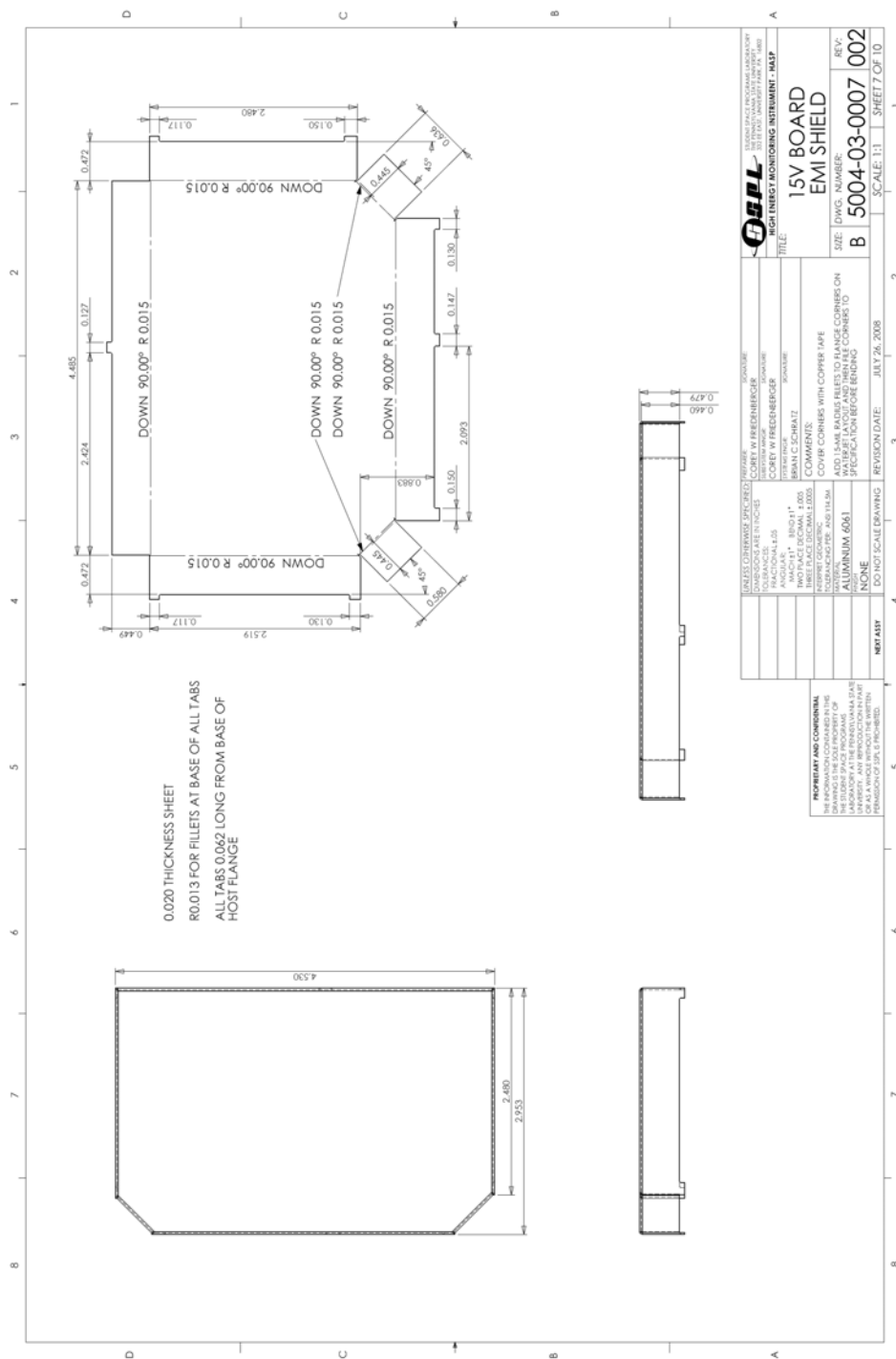
Figure E.7: Mechanical Drawing: 15-V Board EMI Shield
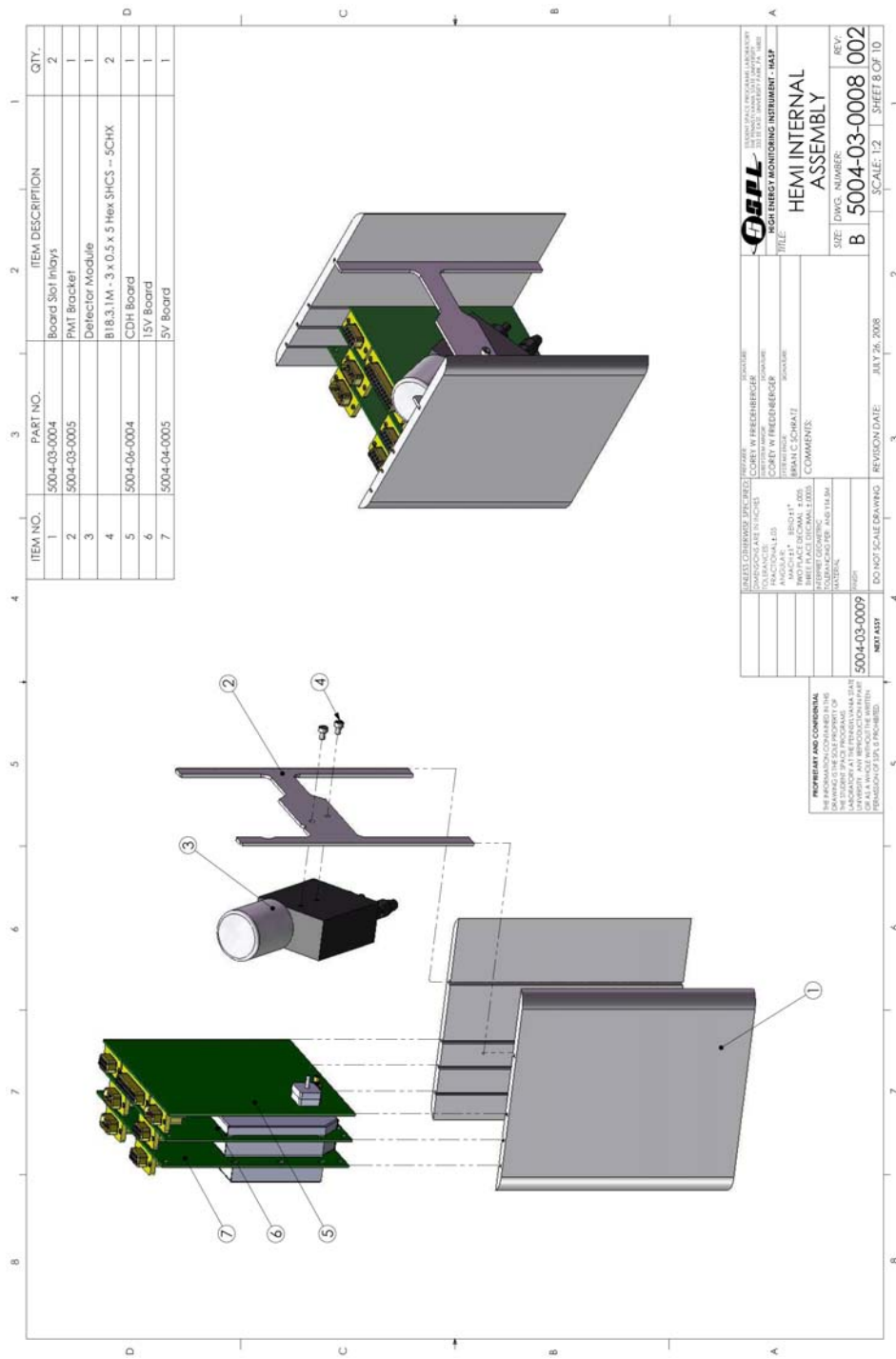
Figure E.8: Mechanical Drawing: HEMI Internal Assembly
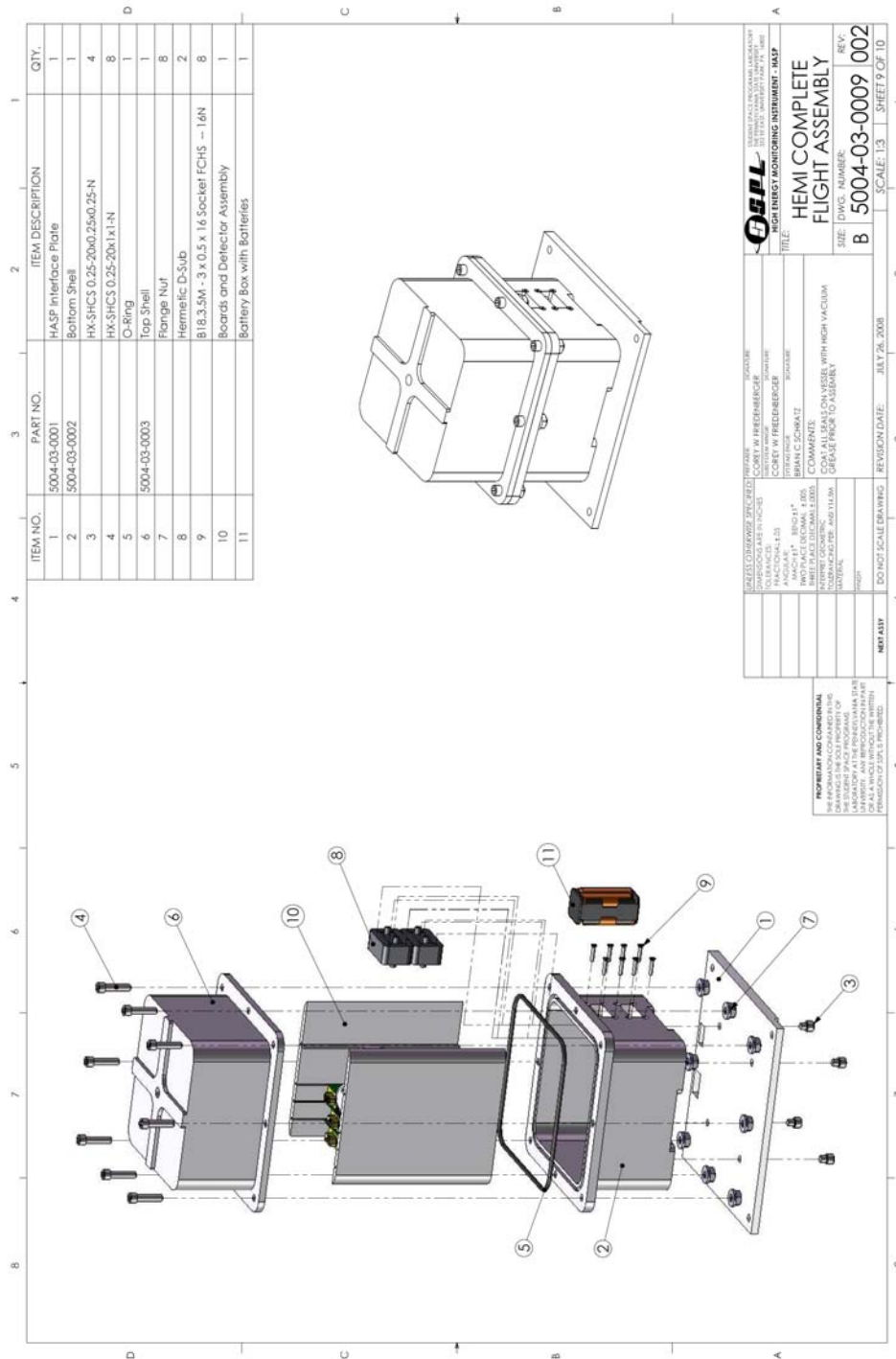
Figure E.9: Mechanical Drawing: HEMI Complete Flight Assembly
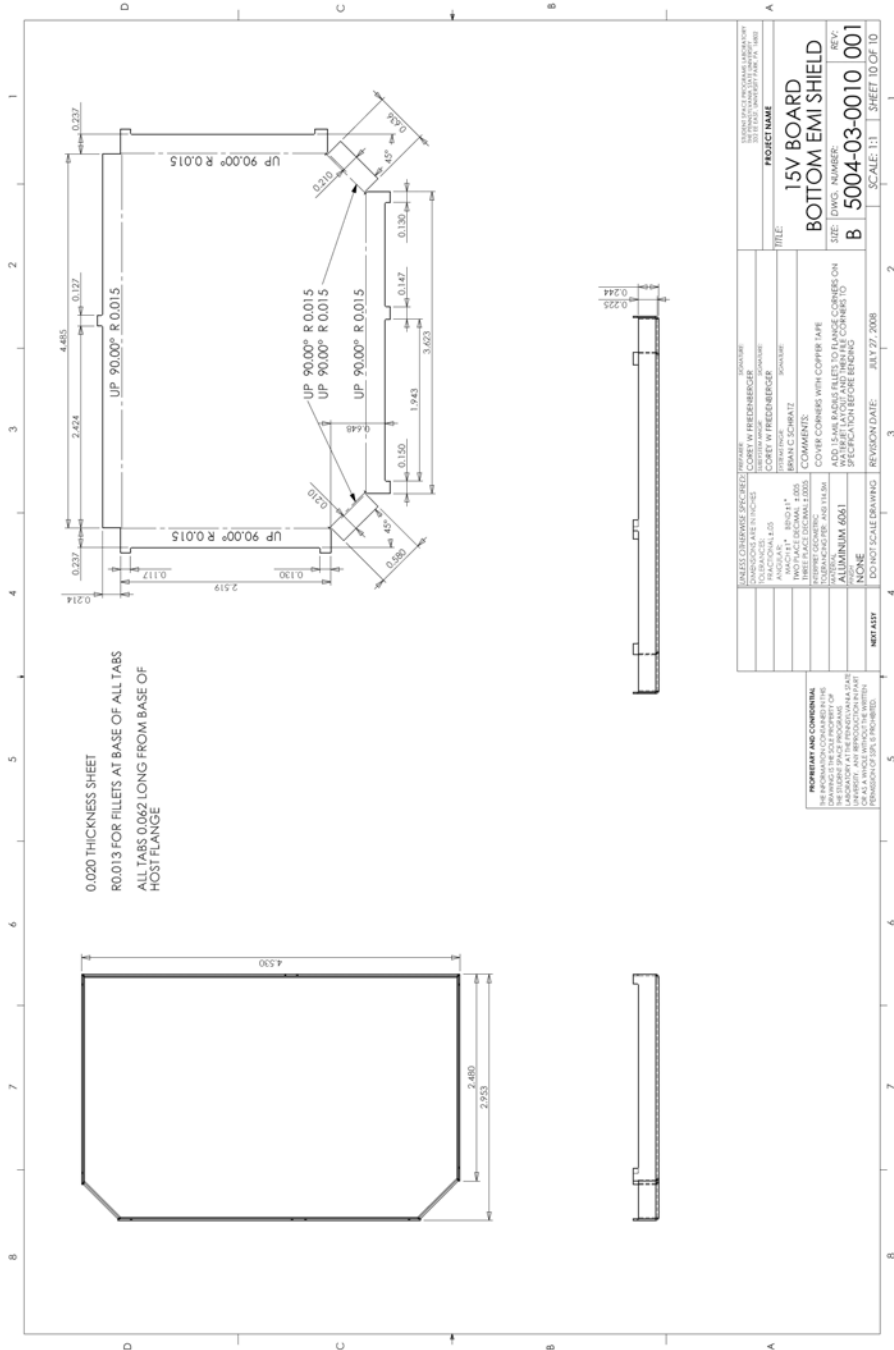
Figure E.10: Mechanical Drawing: 15-V Board Bottom EMI Shield

Appendix F

Power System DC/DC Converter MATLAB Model

```matlab
function y = dcdcfilter(x)

% Sample uses (2.088u,200m,34u,200m,10n,10m,10k)

% Enter the parameters in a 7 column 1 row bracket
% From left to right the parameters are L, Rl, C, Rc, Cd, Rcd, R

% Used for final boards (clear to use function)
x = [2.088e-6, 200e-3, 15e-6, 200e-3, 100e-9, 10e-3, 182e3];

L = x(1,1);    % 2.4 uH
Rl = x(1,2);   % 200 mOhm ESR
%C = x(1,3);   % 30 uF (for final design: pre-fab)
C = 15e-6;     % 30 uF (for flight: post-fab change)
Rc = x(1,4);   % 200 mOhm ESR
Cd = x(1,5);   % 100 nF
Rcd = x(1,6);  % 10 mOhm ESR
R = x(1,7);    % 182 kOhm

% Below are the equivalent impedances

Z1 = (Rl + tf([L,0],[1]));
Z2 = (Rc + tf([1],[C,0]));
Z3 = (R + Rcd + tf([1],[Cd,0]));
Zeq = (Z2*Z3)/(Z2+Z3);

y = (Zeq/(Zeq+Z1))^3;

% specify the frequency values to use
w = logspace(0,8,10000);

% Create the bode plot (in Hertz)
figure(2)
bode(y,w)
h = gcr;
h.AxesGrid.XUnits = 'Hz';
h.AxesGrid.Grid = 'on'
```

Appendix G

HEMI-HASP Document Library

All formal project documentation was stored and managed through SSPL's web-based Microsoft SharePoint site. All project documents follow the SSPL document numbering standard defined by SSPL# 0000-00-0001, which describes the following format for document numbers:

PPPP	-SS-	CCCC.	RRR
Project Number	**S**ubsystem	**C**omponent	**R**evision

The HEMI pathfinder on HASP was project number 5004 (the 4th where 5000 denotes a balloon project). The subsystems numbers are:

00 – Project Management
03 – Mechanical
04 – Power
06 – Command and Data Handling
09 – Payload/Science
10 – Integration and Test

The component number is assigned chronologically for this project although other SSPL projects may adopt a different standard. Below is the list of official documents for this project, all of which can be found on SSPL's internal SharePoint website linked from http://sspl.psu.edu.

5004 – HASP 2008 (HEMI Pathfinder)

Subsystem : 00 - Project Management
   0001 High Energy Monitoring Instrument (HEMI) Proposal

0002 HEMI-HASP Document Template
0003 Payload Integration Plan

Subsystem : 03 - Mechanical
  0001 HASP Interface Plate
  0002 Pressure Vessel Bottom Shell
  0003 Pressure Vessel Top Shell
  0004 Internal Assembly Slotted Inserts
  0005 PMT Module Mounting Bracket
  0006 5V Board EMI Shield
  0007 15V Board EMI Shield
  0008 HEMI Internal Assembly
  0009 HEMI Complete Flight Assembly
  0010 15V Board Bottom EMI Shield
  0100 Vacuum Chamber Pressure Test Procedure for the Pressure Vessel with
        Thermal Cycling
  0101 Sealing Procedure for the HEMI-HASP Pressure Vessel
  0102 Vacuum Chamber Pressure Test Results (text)
  0102 Vacuum Chamber Pressure Test Data Plots
  0103 Finite Element Analysis Plots
  0200 SolidWorks Design Files

Subsystem : 04 - Power
  0004 5V DC/DC Schematic
  0004 5V DC/DC Schematic
  0005 5V DC/DC Layout
  0005 5V DC/DC Layout
  0006 15V DC/DC Schematic
  0006 15V DC/DC Schematic
  0007 15V DC/DC Layout
  0007 15V DC/DC Layout
  0008 5V Power Board Post-Fab Corrections
  0009 15V Power Board Post-Fab Corrections
  0010 5V DC/DC Board Assembly and Test Procedure

Subsystem : 06 - Command and Data Handling
  0001 AD7801 DAC, THS1030 ADC, AD8611 Comparator Prototype
  0001 AD7801 DAC, THS1030 ADC, AD8611 Comparator Prototype
  0002 FPGA Schematics
  0002 FPGA Schematics
  0003 FPGA Development Board Schematics
  0003 FPGA Development Board Schematics (zip)
  0004 FPGA Layout

0004 FPGA Layout
0005 FPGA Development Board Layout
0005 FPGA Development Board Layout
0006 AD9221,AD9223,AD9220 Analog to Digital Converter Prototype
0006 AD9221,AD9223,AD9220 Analog to Digital Converter Prototype
0007 AD7801 Prototype Schematics
0007 AD7801 Prototype Schematics
0008 AD7801 Layout
0008 AD7801 Layout
0010 Instrument Board Schematics
0010 Instrument Board Schematics
0011 Instrument Board Layout
0011 Instrument Board layout
0012 Instrument Board Assembly and Test Procedure
0013 RS232 Loopback Test Project Files
0014 adc to tx
0015 DAC_MODULE
0016 Tested counting DAC code
0017 Byte Shift to Async TX FPGA Project
0018 RS232 Loopback, no parity
0019 HASP Selective Downlink on Uplink Command
0020 HASP Downlink Prototype - 1Hz dataframe containing 00 thru FF (19.2
        E)
0021 HASP_Downlink 244 bytes, 2hz repeat, 2400 no parity
0022 HASP Downlink Integration Test, 2400, no parity, start-stop control
0023 Peak Detection Test 25 Aug 08
0025 Peak Detection 29Aug08 - upload threshold, downlink as received, works
        with LabVIEW interface
 0026 peak_deadband-last modified 3Sept08

 Subsystem : 09 - Payload/Science
  0001 Payload Tests
  0002 Science Investigation & Testing Setup
  0003 HEMI/HASP Flight Data Processing File (.m)
  0004 PMT Graphs
  0005 MATLAB Programs
  0006 Test Files

 Subsystem : 10 - Integration and Test
  0001 Thermistor Calibration in Cryo Oven
  0002 2Pressure 2Temperature Test(user prompt)
  0004 Thermistor Calibration Data
  0005 Thermistor Calibration Data Points
  0006 Thermistor Calibration Stats and Data
  0007 2Pressure 2Temperature Data Set Sc

0008 Voltage&Current Test(user prompt)
0009 2Voltage Test(user prompt)
0010 Data Simulation for HEMI-HASP
0011 MUX Working Test Code
0012 HASP VIs to Read Downlink
0013 Wiring Harness
0014 Safety Thermal Calibration
0015 HEMI Post Flight Calibration Files

Appendix H

C&DH FPGA and Development Board Schematics

Figure H.1: FPGA Development Board, Capacitors

Figure H.2: FPGA Development Board, FPGA Headers--Sockets
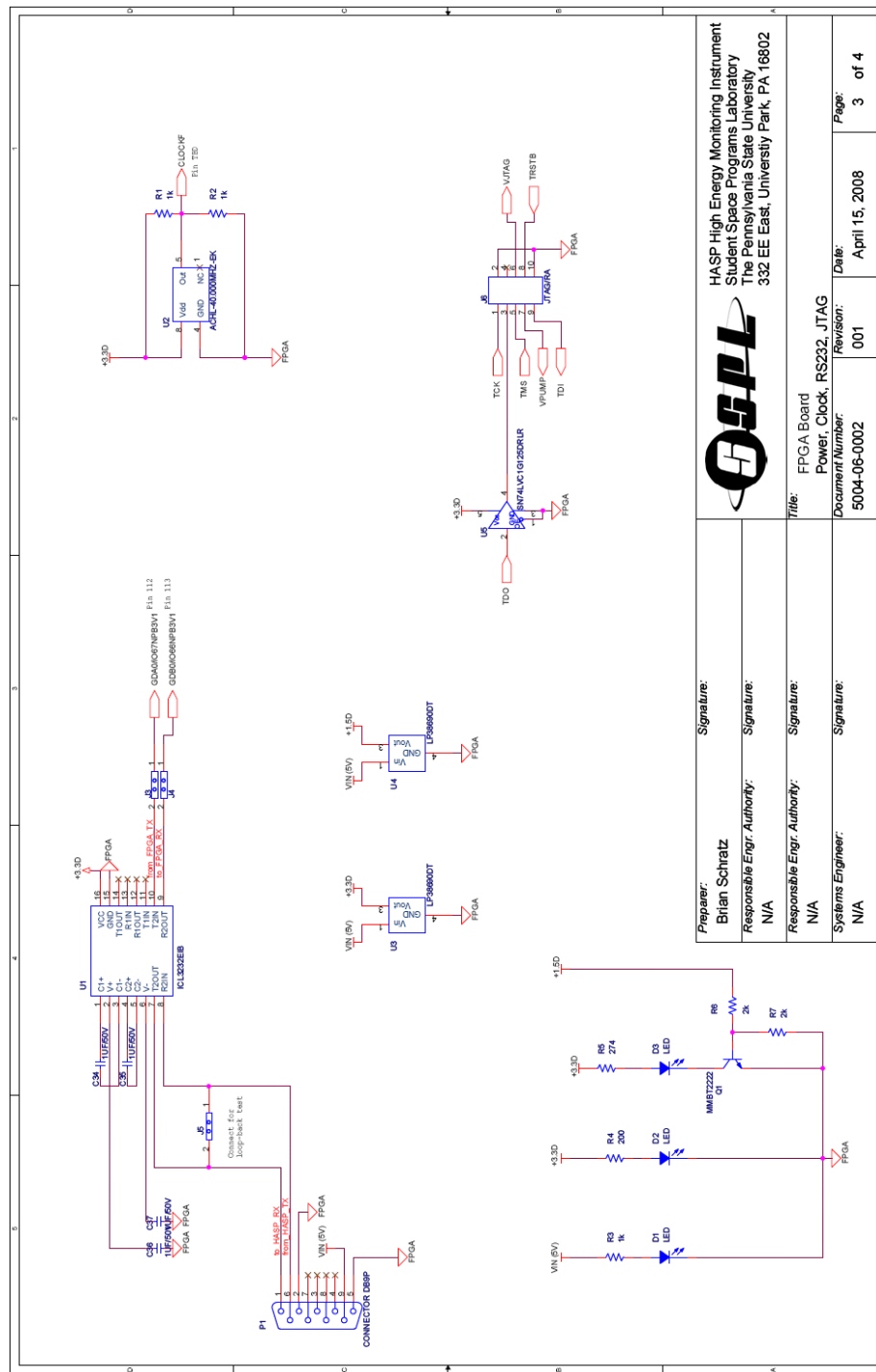
Figure H.3: FPGA Development Board, Power, Clock, RS232, JTAG
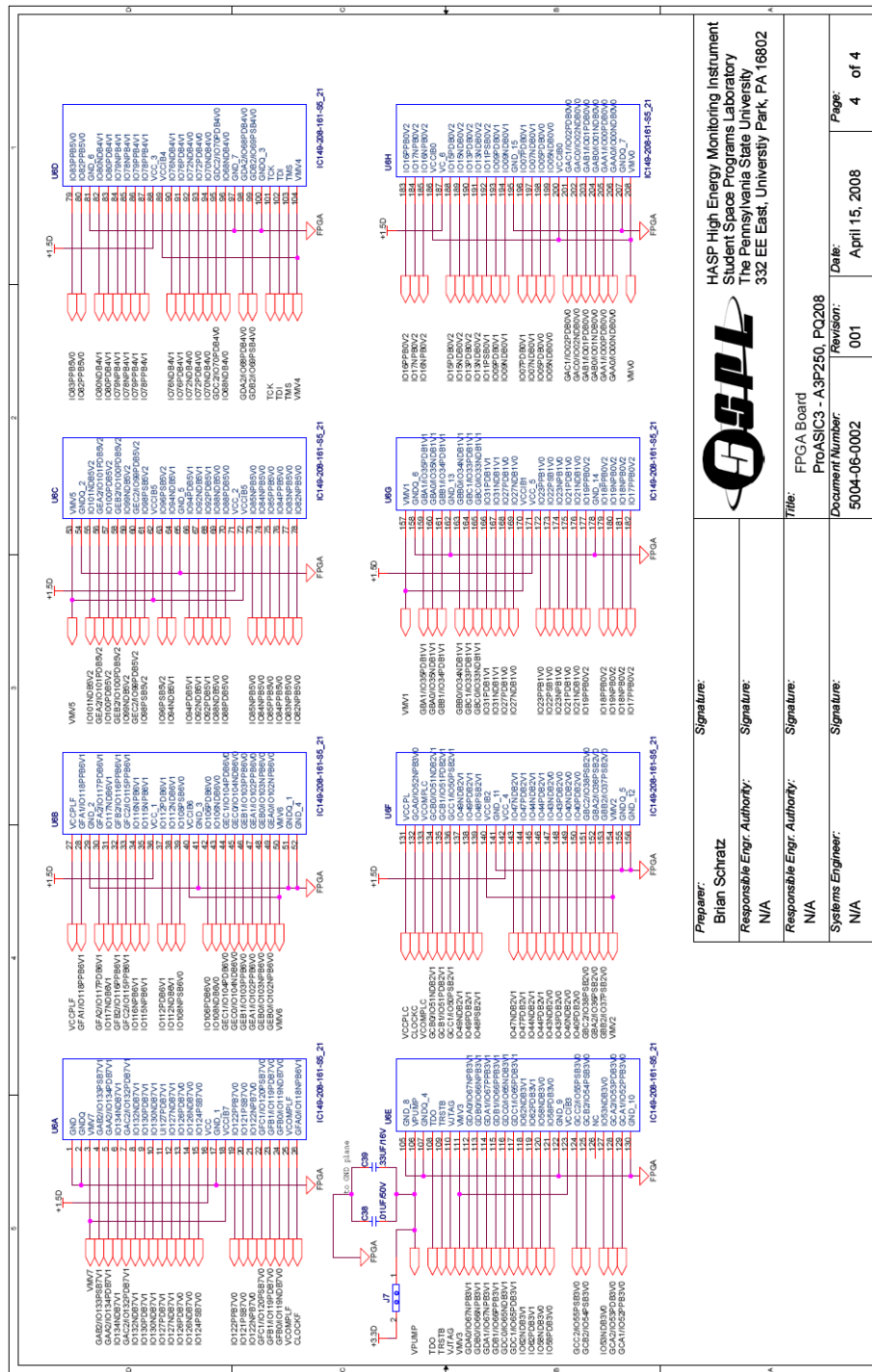
Figure H.4: FPGA Development Board, ProASIC3 - A3P250, PQ208

185
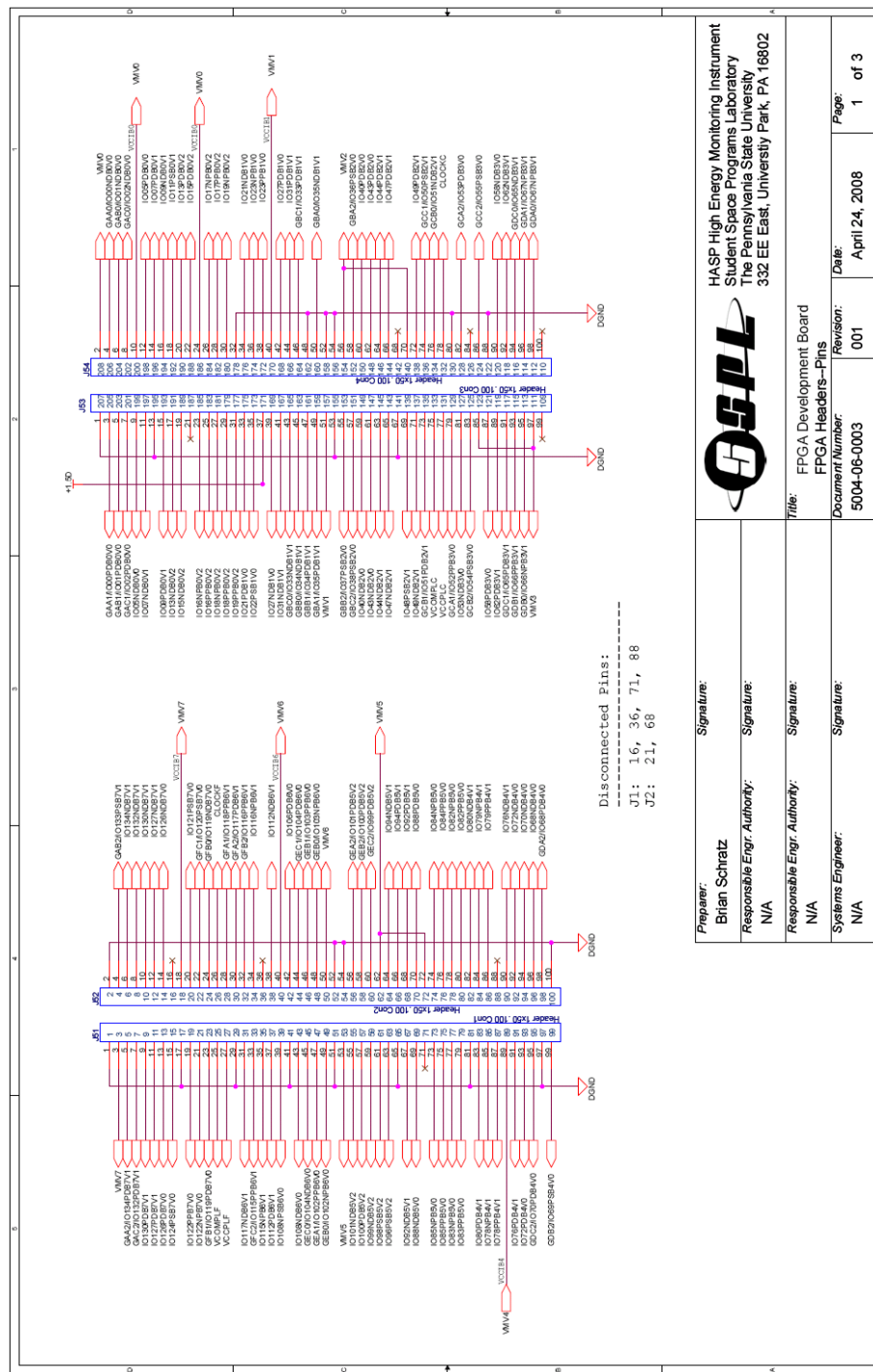
Figure H.5: FPGA Breakout Board, FPGA Headers--Pins
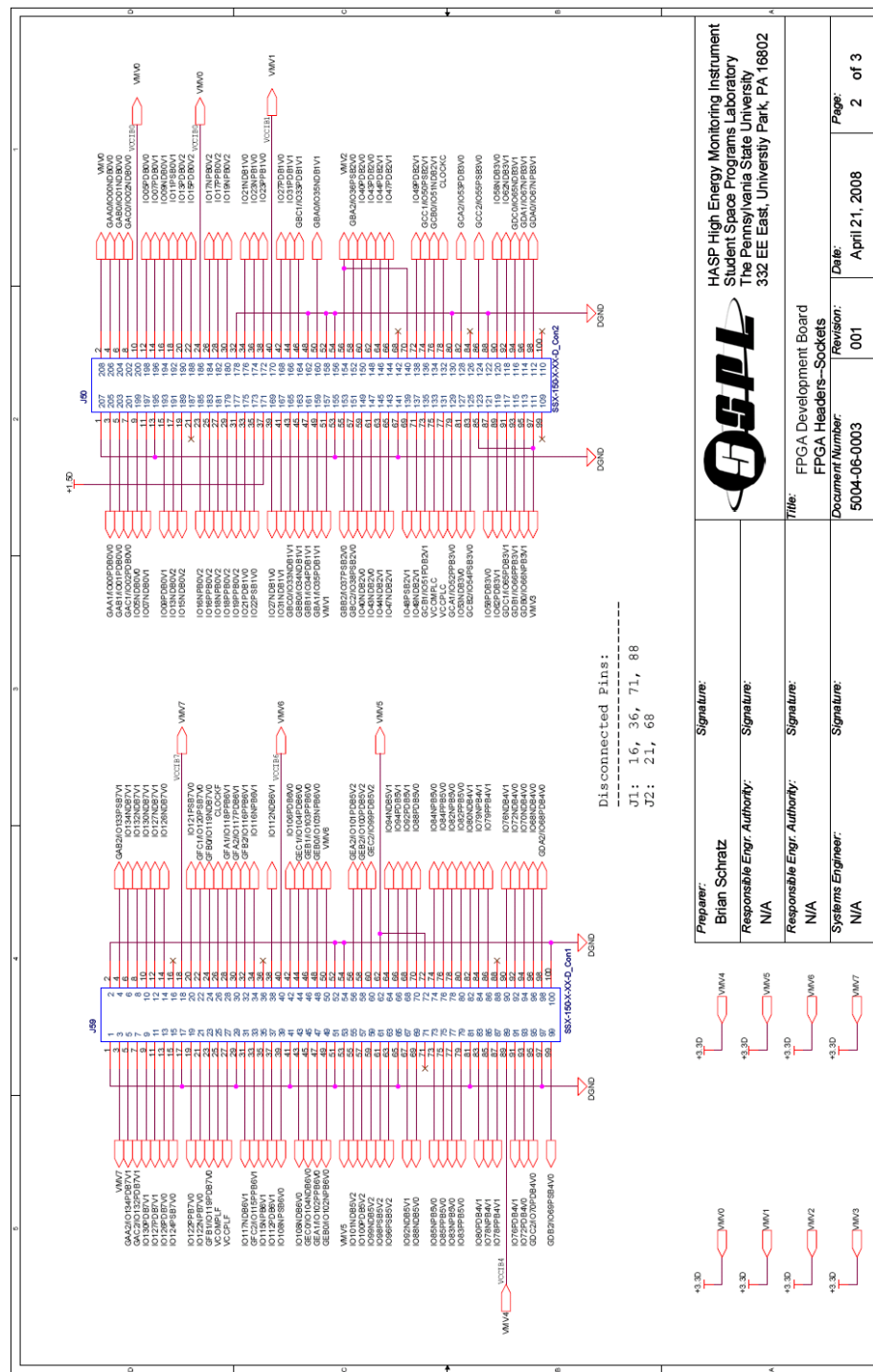
Figure H.6: FPGA Breakout Board, FPGA Headers--Sockets

Figure H.7: FPGA Breakout Board, User I/O

Appendix I

Structure Preliminary Design

The baseline structure at CDR consisted of two parts: the electronics housing and the detector bracket. The electronics housing provided a platform and heat sink for the electrical circuit boards. The detector bracket provided a rigid mounting platform for the compact PMT modules and their respective patch heaters.

The baseline design of the electronics housing was a simple box formed of 0.08-inch thick aluminum panels. The box measured 150 mm × 150 mm in footprint and was just tall enough to provide room for the circuit trays and mounting hardware. To provide a cost-effective method of securing the six panels to each other, corner brackets were formed by drilling and tapping cubes cut from an aluminum square bar.
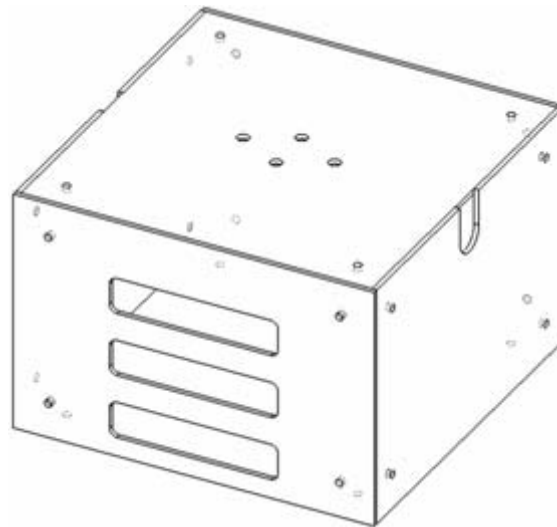

Figure I.1: Initial Electronics Housing Design.

The detector bracket (see Figure I.2), which screwed to the four central holes on the top panel seen in Figure I.1, consisted of two side plates with spacers, and a mounting block. Each PMT module was fitted with mounting holes on one side only; therefore, each U-shaped plate was drilled only at one end for PMT attachment, and the other end served as a guard for the patch heaters to be installed on each PMT. The necessary space between the plate and PMT module was provided by the spacers.
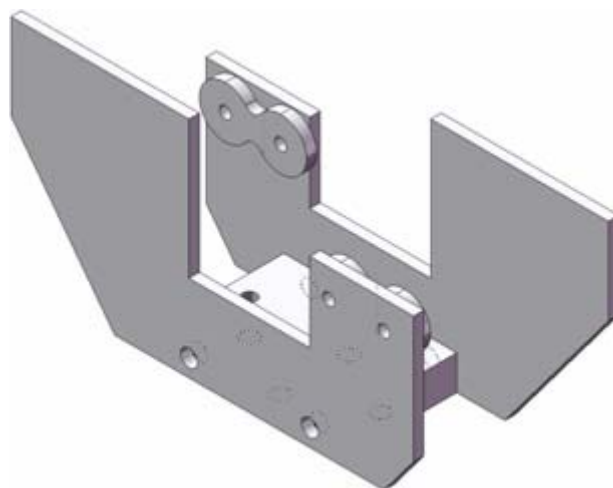

Figure I.2: PMT Module Mounting Bracket.

The mounting block that connects the plates and secures them to the electronics housing was a 50 mm × 32 mm × 10 mm block with drilled and tapped holes for connecting screws. The bracket was not load bearing, but it needed to be rigid enough in order to ensure the PMT modules and crystal would maintain proper alignment for the flight duration.

To support the power, FPGA, and payload circuit boards, four trays were installed inside the electronics housing. The basic design for each tray, shown in Figure I.3, entailed two rails (milled with custom standoff heights for each board) connected by a

base plate, which could be cut with openings for board-to-board connectors. Note that

the front panel would be ported to allow external connector access and the base plate

would be ported for board-to-board connectors. At each end, a plate was screwed to the

rails, with the front plate having ports cut into it for access to the connectors. These

connectors were exposed by ports also cut into the front housing plate (see Figure I.1),

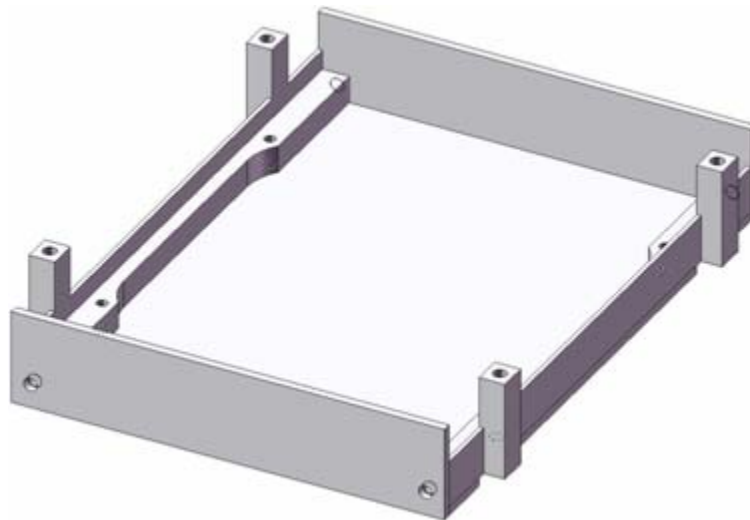and external cables were used to wire the trays together.

Figure I.3: Basic Circuit Board Tray Design.

Because the electrical design called for board-to-board connectors, the vertical

spacing was important. The standoffs machined into the rails were machined to the

necessary height to maintain the required distance between boards. The bottom plate

thickness had no bearing on the standoff height as the plate was notched to allow the rails

to rest directly on top of one another.

A primary concern with the circuit boards was that they may overheat as the

structure will be in near vacuum and the tray ledges do not provide substantial thermal

contact. In order to facilitate thermal flow between the circuit boards and aluminum

trays, the boards were to be encapsulated with a potting compound, using the tray itself as

a mold. Loctite 3860 is the ideal compound for this encapsulation, as the epoxy provides

a high coefficient of thermal conductivity of 1.25 W/(m•K) while also increasing between

components the dielectric breakdown strength from that of vacuum.

The baseline design at CDR is shown in Figure I.4, which shows the assembled

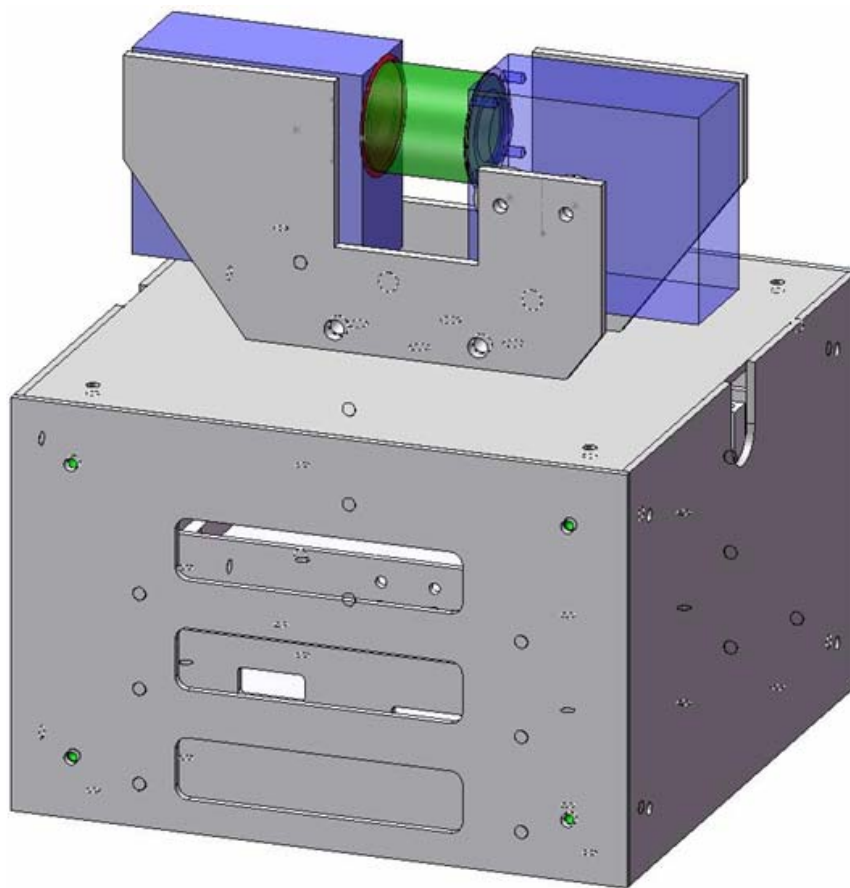HEMI structure with PMT modules (blue) and crystal (green).

Figure I.4: CDR Baseline Mechanical Design

In order to meet flight requirements set by HASP, HEMI had a total mass

requirement of equal to or less than the 3-kg limit. Knowing that the aluminum 6061

alloy being used for all machined parts had a density of 2710 kg/m^3, the Solidworks CAD software was able to compute the mass of all parts during the development of the design.

As this design was never fully fabricated, all mass estimates were modeled and not actual; however, a small contingency of 10% on the mass estimates were kept as they were based on volumetric data from the working design model.

I.1 Mechanical Baseline Trades: PMT Module Mounting Bracket

The originally proposed concept design entailed placing a PMT tube inside of the main structure, with the scintillating crystal protruding from an opening at the top. This, design however, was abandoned due to a change in PMT choice to a PMT module that included the high voltage power supply and voltage divider.

The CDR baseline detector design consisted of two rectangular, compact PMT modules with a crystal suspended between the lenses (see Figure I.4 above). The modules could be rotated in any configuration about the crystal, so long as the crystal's line-of-sight was not obstructed from above.

One design consideration for CDR baseline was to mount the PMTs flat against the inside of the upper electronics housing panel with the crystal at the center of the panel, and to have the upper panel and upper-halves of the side panels notched to expose the crystal. For the science aspect of the detector, this design was feasible, but for fabrication of the structure, it has a higher level of risk. There is no direct connection between the two PMT modules, so the machining tolerances between parts would compound to a significant degree between the two modules; this creates a problem when

one considers that the crystal is being glued to the PMT module lenses, and large errors in PMT separation distance could either dislodge or damage the crystal.

The CDR baseline design for the PMT mounting is shown in Figure I.2. This design, consisting of two identical mounting plates and spacers separated by a mounting block, provided a rigid mount where the PMT modules were separated by a single unit, independent of the rest of the structure. This design also allowed the crystal to have maximum exposure to its surroundings with minimal secondary particles caused by surrounding structural material.

I.2 Mechanical Baseline Trades: Electronics Housing and PCB Trays

The baseline design of the electronics housing remained relatively constant, only changing in dimensions to accommodate the electronics and remain within originally specified design constraints.

To assemble the structure, the design uses cubic corner brackets. Another design that was considered was brackets that were similar to cubes, but with the inside corner notched out for mass; however, this involves additional machining that may prove difficult, and the mass saved by doing so would have been minimal. Additionally, solid cubes provided extra heat sinking and perhaps better heat flow between panels.

The originally proposed design also included L-shaped brackets mid-way between the top and bottom, holding the side panels together to prevent warping with thermal contraction, which was important with the original detector design. However, this

became unnecessary once the electronics housing became more compact and the PMT modules were mounted independent of the electronics housing.

PCB trays for previous projects have been milled mainly from solid aluminum blocks, creating a single piece. This design, however, has proven problematic when milling thin-walled trays, which would have been necessary for this project to minimize mass. As observed with past ESPRIT sounding rocket circuit trays, the tray walls tended to buckle and warp when being machined. Because this instrument needed low-mass trays that could be easily and quickly fabricated, and because high-precision was not necessary for this specific flight, this previous tray design is was not used.

The CDR baseline design for the PCB tray design (refer back to Figure I.3) allowed for a low mass structure while also minimizing manual milling. The front, rear, and bottom panels were all cut from aluminum sheets on a water jet, which also enabled the team to easily create ports for all external and board-to-board connections without extra milling.